Departamento de Química Física
y Termodinámica Aplicada
Universidad de Córdoba

PELÍCULAS ORGÁNICAS ORGANIZADAS EN SISTEMAS NANOESTRUCTURADOS

ORGANIC FILMS ORGANIZED IN NANOSTRUCTURED SYSTEMS

Tesis Doctoral

Antonio Miguel González Delgado

Córdoba, Julio 2012

TÍTULO: Películas orgánicas organizadas en sistemas nanoestructurados.

AUTOR: Antonio Miguel González Delgado

Campus de Rabanales Ctra. Nacional IV, Km. 396 A
14071 Córdoba

www.uco.es/publicaciones
publicaciones@uco.es

PELÍCULAS ORGÁNICAS ORGANIZADAS EN SISTEMAS NANOESTRUCTURADOS.

LOS DIRECTORES

Fdo.: Luis Camacho Delgado
Catedrático del Departamento de Química Física y Termodinámica Aplicada. Universidad de Córdoba.

Fdo.: Marta Pérez Morales
Profesora Ayudante Doctora del Departamento de Química Física y Termodinámica Aplicada. Universidad de Córdoba.

Trabajo presentado para optar al grado de Doctor en Ciencias Químicas

Fdo.: Antonio Miguel González Delgado
Licenciado en Ciencias Químicas

DEPARTAMENTO DE QUÍMICA FÍSICA
Y TERMODINÁMICA APLICADA
UNIVERSIDAD DE CÓRDOBA

D. Luis Camacho Delgado, Catedrático y Director del Departamento de Química Física y Termodinámica Aplicada de la Universidad de Córdoba,

INFORMA:

Que el trabajo presentado como Tesis Doctoral por D. Antonio Miguel González Delgado, titulado "*Películas Orgánicas Organizadas en Sistemas Nanoestructurados*" ha sido realizado en los laboratorios de este Departamento, así como en las instalaciones del Groupe d'Etude des Vecteurs Supramoléculaires de la Université Henri Poincaré Nancy I (Francia) y en el Department Chemie und Pharmazie de la Friedrich-Alexander Universitat Erlangen-Nurnberg (Alemania), y reúne las condiciones exigidas según legislación vigente.

Y para que conste, firmo el presente en Córdoba a Veintiséis de Junio de dos mil doce.

Fdo.: Luis Camacho Delgado

Mediante la defensa de esta memoria se pretende optar a la obtención de la **Mención Internacional**, habida cuenta que el doctorando reúne los requisitos exigidos para tal mención:

1. Se cuenta con los informes favorables de dos doctores pertenecientes a instituciones de Enseñanza Superior, o instituto de investigación, de países europeos distintos al nuestro.
2. En el Tribunal, que ha de evaluar la Tesis, existe un miembro de un centro de Enseñanza Superior de un país europeo distinto al nuestro.
3. Parte de la redacción y defensa de la Memoria se realizará en la lengua oficial de un país europeo distinto al nuestro.
4. El doctorando ha realizado una parte del trabajo experimental en las instalaciones del Groupe d'Etude des Vecteurs Supramoléculaires de la Université Henri Poincaré Nancy I (Francia). Esta estancia, de un trimestre de duración, se ha realizado gracias a la concesión de ayuda para estancias breves en el extranjero asociada a la beca de Formación de Personal Investigador del Ministerio de Ciencia e Innovación.

El trabajo que engloba la presente Memoria se ha realizado durante el periodo de disfrute de una Beca de Formación de Personal Investigador del Ministerio de Ciencia e Innovación, asociada al proyecto financiado por la D. G. I. C. Y T. "*Influencia de la organización molecular en fenómenos de transferencia eléctrica y de transferencia de energía. Aplicaciones al diseño de dispositivos nanoestructurados*" (CTQ2007/64474)

LUIS CAMACHO DELGADO, Catedrático del Departamento de Química Física y Termodinámica Aplicada de la Universidad de Córdoba.

INFORMA:

Que el trabajo presentado como Tesis Doctoral por D. Antonio Miguel González Delgado titulado *"Películas orgánicas organizadas en sistemas nanoestructurados"*, ha sido realizado bajo su dirección en los laboratorios de este Departamento y reúne las condiciones exigidas según la legislación vigente.

Y para que conste, firmo el presente en Córdoba a 26 de Junio de 2012.

Fdo.: Luis Camacho Delgado

MARTA PÉREZ MORALES, Profesora Ayudante Doctor del Departamento de Química Física y Termodinámica Aplicada de la Universidad de Córdoba.

INFORMA:

Que el trabajo presentado como Tesis Doctoral por D. Antonio Miguel González Delgado titulado *"Películas orgánicas organizadas en sistemas nanoestructurados"*, ha sido realizado bajo su dirección en los laboratorios de este Departamento y reúne las condiciones exigidas según la legislación vigente.

Y para que conste, firmo el presente en Córdoba a 26 de Junio de 2012.

Fdo.: Marta Pérez Morales

TÍTULO DE LA TESIS: PELÍCULAS ORGÁNICAS ORGANIZADAS EN SISTEMAS NANOESTRUCTURADOS

DOCTORANDO/A: ANTONIO MIGUEL GONZÁLEZ DELGADO

INFORME RAZONADO DEL/DE LOS DIRECTOR/ES DE LA TESIS

(se hará mención a la evolución y desarrollo de la tesis, así como a trabajos y publicaciones derivados de la misma).

La presente Tesis Doctoral se ha desarrollado en los laboratorios del Departamento de Química Física y Termodinámica Aplicada de la Universidad de Córdoba bajo nuestra dirección. Esta Tesis Doctoral reúne todas las condiciones exigidas según la legislación vigente. Su evolución y desarrollo ha seguido el plan de trabajo inicialmente previsto, alcanzándose los objetivos previamente marcados. Durante la elaboración de la Tesis, el doctorando ha realizado dos estancias breves de investigación en centros internacionales. Ha dado lugar a cinco publicaciones, tres de ellas ya publicadas en revistas internacionales de reconocido prestigio, una pendiente de acpetación y otra en preparación, así como a diversas comunicaciones en congresos nacionales e internacionales.

Por todo ello, se autoriza la presentación de la tesis doctoral.

Córdoba, 26 de __Junio_____ de __2012_____

Firma del/de los director/es

Fdo.: Luis Camacho Delgado____ Fdo.: Marta Pérez Morales___

Índice General

OBJETIVOS

La presente Memoria presentada como Tesis Doctoral se encuadra en la línea de investigación *"Películas Superficiales y Organización Molecular"* del grupo FQM-204 de la Junta de Andalucía. Los objetivos globales que se han marcado son:

1. Preparar y caracterizar películas superficiales homogéneas y estables de colorantes orgánicos, puros y/o mezclados con matrices lipídicas, que sean susceptibles de ser transferidas a soportes sólidos mediantes las técnicas LB y LS.
2. Estudiar y controlar la agregación de colorantes orgánicos en la interfase aire-agua, así como la distancia promedio entre moléculas.
3. Estudiar las propiedades fotofísicas de colorantes orgánicos ensamblados en películas delgadas, así como la influencia ejercida por la estructura molecular alcanzada en la película sobre sus propiedades fotofísicas y ópticas.
4. Sintetizar un calix[6]areno anfifílico, así como un complejo de inclusión calixareno-C_{60}, capaces de formar películas superficiales estables en la interfase aire-agua.
5. Estudiar la influencia de la conformación y orientación del calixareno anfifílico en la estabilidad y propiedades de las películas formadas.

The work described in this Report belongs to the research line *"Thin Films and Molecular Organization"* within the group FQM-204 (Junta de Andalucía classification). The main goals of this research were as follows:

1. To prepare and to characterize homogeneous and stable thin films with organic dyes, pure and/or mixed with lipidic matrixes. These thin films should be able to be transferred to solid supports by means of the LB and LS techniques.
2. To study and to control the aggregation of organic dyes at the air-water interface, as well as the average distance between molecules.
3. To study the photophysical properties of thin-film assembled organic dyes, as well as the influence of the molecular structure of the film over its photophysical and optical properties.
4. To synthesize an amphiphilic calix[6]arene, and an inclusion complex calixareno-C_{60}, which are able to form stable thin films at the air-water interface.
5. To study the influence of the conformation and orientation of the amphiphilic calixareno in the stability and properties of the formed films.

CAPÍTULO 1

INTRODUCCIÓN

1.1. MÉTODOS DE PREPARACIÓN DE PELÍCULAS DELGADAS

1.1.1 Películas de Langmuir y Langmuir-Blodgett (LB)

Las primeras experiencias relacionadas con la formación de monocapas en la interfase aire-agua siguiendo un método científico se remontan a los estudios llevados a cabo por Benjamin Franklin (1706-1790), los cuales estimularon a posteriores científicos a investigar de manera más profunda en este nuevo campo.

Sin duda, la aportación más importante la realizó Irving Langmuir (1881-1957), que destacó por su trabajo en Química de Superficies, el cual le llevó a conseguir el Premio Nobel de Química en 1932. Su trabajo, junto con el de Lord Rayleigh (1842-1919), llega a confirmar que las capas de moléculas anfifílicas esparcidas sobre superficies acuosas (*películas de Langmuir*) tienen el espesor de una capa molecular simple y concluyó que las moléculas estaban orientadas en la superficie acuosa, con un grupo funcional polar inmerso en el agua y una cadena alifática situada casi verticalmente respecto a la superficie. Sus experimentos apoyaron la hipótesis de la existencia de interacciones de corto alcance, y dieron la base sobre los tipos de moléculas que podían formar este tipo de películas.

Katherine Blodgett (1898-1979), bajo la dirección de Irving Langmuir, fue la primera persona capaz de transferir monocapas de ácidos grasos desde la superficie acuosa a soportes sólidos tales como vidrio hidrofílico, formándose así las denominadas *películas de Langmuir–Blodgett* (LB).

Desde entonces hasta nuestros días, el abanico de posibilidades que ofrece esta técnica ha aumentado considerablemente. Actualmente, la técnica LB constituye una herramienta muy útil para la construcción de dispositivos supramoleculares con aplicaciones en diferentes áreas como óptica no lineal, sensores, electrónica molecular y fotocromismo.[1-6]

1.1.1.1 Formación de Monocapas en la Interfase Aire-Agua

La formación de monocapas en la interfase aire-agua se basa en la insolubilidad

de las moléculas que las forman y, sobre todo, en la estructura anfifílica de las mismas, es decir, poseen una parte apolar hidrofóbica (una o varias cadenas alifáticas), y otra polar hidrofílica (grupos funcionales tipo ácido, alcohol o amina).[7-8] Mediante la técnica de Langmuir, la preparación de las monocapas se efectúa añadiendo una cantidad determinada de moléculas anfifílicas sobre la superficie acuosa, disueltas en un disolvente volátil e inmiscible en agua, las cuáles ocupan toda la superficie disponible (Figura 1.1). En este proceso, la elección del disolvente o mezcla de disolventes es importante, ya que debe favorecer la máxima dispersión de las moléculas sobre el agua.[9] Una vez se evapora el disolvente, cabe esperar que la disposición de las moléculas en la monocapa sea aquella en la que su situación energética resulte más favorable, esto es, con los grupos polares inmersos en la subfase acuosa y las colas hidrófobas fuera de la misma.[7]

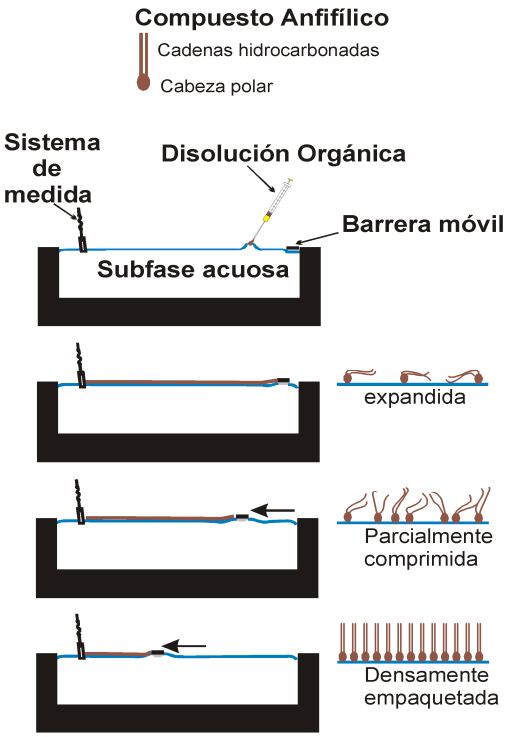

Figura 1.1

En este momento, la tensión superficial (γ) de la zona cubierta por la monocapa disminuye respecto a la tensión superficial de la superficie del agua limpia (γ_0) y como consecuencia, se mide la presión superficial (π) definida por

$$\pi = \gamma_0 - \gamma \qquad (1.1)$$

En principio, cualquier método para determinar la tensión superficial puede ser usado para medir la presión superficial. En la práctica se utilizan dos tipos de sistemas, el tipo Wilhelmy y el tipo Langmuir.[10]

Tras la evaporización del disolvente, la monocapa se comprime reduciéndose el área superficial disponible, la densidad superficial de las moléculas incrementa, disminuye γ y aumenta π. De esta manera, la representación de π frente al área por molécula (A) aumenta cuando el área disminuye (ver Figura 1.2), siendo la analogía bidimensional de una isoterma presión-volumen. Las isotermas π-A dan información acerca de la estabilidad de la monocapa en la interfase aire-agua, de la organización de las moléculas en la monocapa y de las interacciones entre ellas.

A partir de las isotermas π-A se obtienen dos parámetros muy importantes. Por una parte, el valor del área límite, obtenido por extrapolación del tramo de mayor pendiente de la isoterma a presión superficial cero, que corresponde al área ocupada por una molécula en una situación de máximo empaquetamiento (líneas de puntos en la Figura 1.2). Por otra, el valor máximo de presión superficial al cual la monocapa pierde su estabilidad, conocido con el nombre de *presión de colapso* (π_C en la Figura 1.2).

Las isotermas presión superficial-área muestran distintas regiones que corresponden a los diferentes estados de organización o fases en los que se encuentra la monocapa, así como regiones en las que coexisten dos fases.[7]

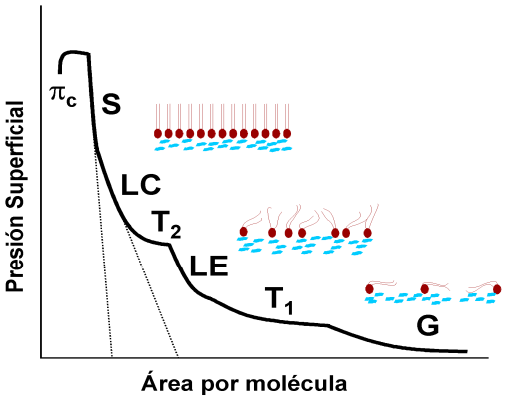

Figura 1.2

En la isoterma π-A mostrada en la Figura 1.2 se indican de forma idealizada las distintas fases para una sustancia anfifílica simple, descritas brevemente a continuación:

- Gaseosa (G): A muy bajas presiones superficiales, las moléculas se encuentran bastante diluidas en el seno de la monocapa y las interacciones entre ellas son débiles, constituyendo una fase denominada gas bidimensional.
- Líquido: Cuando la presión superficial aumenta se llega a una fase fluida muy compresible, en la que las moléculas experimentan unas fuerzas atractivas lo suficientemente intensas como para que empiecen a adoptar una estructura compacta, formándose lo que se llama líquido expandido (LE). Entre estas dos fases descritas ocurre un proceso parecido a la condensación de un gas, es decir, una zona de coexistencia de ambos estados, G + LE (T_1). Aumentos posteriores de presión dan lugar a un estado menos compresible y más ordenado, conocido como líquido condensado (LC). La organización de la monocapa es compacta y la parte hidrófoba de las moléculas se orienta perpendicularmente a la interfase. De nuevo, puede observarse una segunda transición de fase entre la situación de líquido expandido y la de líquido condensado, LE + LC (T_2).
- Sólido (S): Al continuar comprimiendo la monocapa, y antes de que ésta llegue al colapso, se alcanza un estado sólido (S) donde la película es muy rígida y las cadenas hidrófobas forman un apilamiento compacto.

No obstante, hay que indicar que el número y la complejidad de las fases observadas en una isoterma varían en función del sistema estudiado y de las condiciones experimentales bajo las cuales se realizan las isotermas.

La morfología originada por la coexistencia de estados en una monocapa puede visualizarse usando microscopía de fluorescencia,[11] o mediante microscopía de ángulo Brewster (BAM),[12] técnica de gran versatilidad desarrollada en época reciente.

Monocapas mixtas de lípido y colorantes

El método tradicional para la formación de películas de Langmuir requiere el empleo de moléculas anfifílicas. De esta forma, la gama de moléculas que podían formar monocapas estables era limitada. En las últimas décadas, se han desarrollado métodos que permiten utilizar una gran variedad de moléculas para la formación de este tipo de películas, incluso moléculas solubles en agua. Estos métodos están basados en la construcción de monocapas complejas, donde los componentes de la monocapa se organizan bajo control externo y atendiendo a las interacciones intermoleculares específicas de cada sistema. Uno de los métodos propuestos consiste en añadir

componentes solubles en la subfase acuosa de forma que dicho componente pueda adsorberse sobre una matriz lipídica seleccionada, y así ser retenido en la interfase. Más efectivo, sin embargo, se ha mostrado el método denominado de coesparcimiento, en el cual el adsorbato no se añade a la subfase acuosa, sino que se coesparce mezclado con el lípido sobre la superficie acuosa,[13-16] de tal forma que el colorante queda retenido en la interfase mediante interacciones, principalmente, electrostáticas. Con estos métodos, se amplía el rango de moléculas que pueden ser estudiadas mediante la técnica de Langmuir. Existe, sin embargo, una limitación al uso de monocapas mixtas basada en la heterogeneidad del sistema.

1.1.1.2 Técnicas de caracterización de monocapas sobre la interfase aire-agua

Además de las medidas de presión superficial en la balanza de Langmuir, existe una gran variedad de técnicas, en continua evolución, muy útiles en la caracterización de películas superficiales en la interfase aire-agua. A continuación se describen con más detalle aquellas técnicas que han sido utilizadas a lo largo de esta Memoria.

- ***Espectroscopía de Reflexión****:* Esta técnica se basa en la diferencia de reflectividad de una superficie acuosa cubierta con una monocapa y una superficie acuosa desnuda. El método aplicado, representado en la Figura 1.3, utiliza luz no polarizada, la cual se hace incidir de forma normal sobre la superficie del agua.

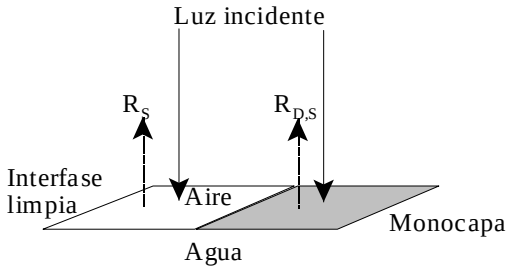

Figura 1.3

Denominaremos R_S y $R_{D,S}$ a las cantidades de radiación reflejadas en ausencia y en presencia de monocapa, respectivamente. Cuando la reflexión y la absorción son pequeñas, aproximadamente se cumple que[17]

$$R_{D,S} = R_S + R_D + A\sqrt{R_S} \qquad (1.2)$$

donde R_D y A son la reflexión y la absorción propias de la monocapa, respectivamente. El término $A\sqrt{R_S}$ representa la amplificación de la luz reflejada a consecuencia de la absorción. Asimismo, $R_D \approx A \times A_M / 4$, donde A_M es la absorción máxima.

$R_{D,S}$ y R_S se determinan simultáneamente en una misma experiencia, por lo que la medida experimental es directamente la diferencia entre ambas

$$\Delta R = R_{D,S} - R_S = A\left(\sqrt{R_S} + \frac{A_M}{4}\right) \approx A\sqrt{R_S} \qquad (1.3)$$

En general, la absorción de la monocapa es lo suficientemente pequeña como para despreciar el término $A_M/4$. Asimismo, en este caso, absorción y absorbancia están relacionadas mediante el factor numérico 2.303, por lo que

$$\Delta R = 2.303 \times 10^3 f_o \varepsilon \sqrt{R_S} \Gamma \qquad (1.4)$$

donde ε representa la absortividad molar en sus unidades habituales ($mol \cdot L^{-1} \cdot cm$), Γ es la concentración superficial en $mol \cdot cm^{-2}$, el factor 10^3 da cuenta del cambio de unidades necesario para que ΔR sea adimensional y, por último, f_o es el factor de orientación. Este factor compara las orientaciones promedio del dipolo de transición en disolución y en la interfase aire-agua y, su introducción es necesaria ya que, la absortividad molar se define como la que posee el cromóforo en disolución.

La ecuación (1.4) nos propone un método para detectar la presencia de cromóforos en la interfase aire-agua a partir de medidas del incremento de la reflexión de la monocapa con respecto a la interfase limpia, permitiendo cuantificar el material existente en dicha interfase y obtener, como se describirá más adelante, información sobre la orientación del cromóforo.

- ***Microscopía de ángulo Brewster (BAM):*** La microscopía de ángulo Brewster es una herramienta excelente para el estudio de monocapas, ya que sólo registra la reflectividad debida a las moléculas situadas en la interfase aire-agua.[18]

La reflectividad en la interfase de dos medios se define como la relación entre la

fracción de intensidad reflejada e intensidad incidente.[19] Esta relación depende de la polarización de la radiación y del ángulo de incidencia. El fenómeno de polarización por reflexión se produce cuando un haz de luz no polarizada incide desde un medio con índice de refracción n_1 en un medio de mayor índice de refracción n_2, con un ángulo *i* tal que el rayo refractado forma un ángulo recto con el reflejado. Además, la polarización producida por este fenómeno es siempre perpendicular al plano de incidencia (polarización s). Aplicando la condición anterior a la ley de Snell (n_1 sen*i*= n_2 sen*r*), se obtiene la ley de Brewster (tg*i* = n_2 / n_1, $n_2 > n_1$), esquematizada en la Figura 1.4.

La microscopía de ángulo Brewster se basa en este principio. Cuando se hace incidir un haz de luz en la interfase aire-agua con polarización paralela al plano de incidencia (polarización p) y con el ángulo Brewster de esta interfase (*i* = 53.1º), toda la radiación es transmitida, no produciéndose reflexión alguna. Si ahora se esparce una monocapa de moléculas sobre la subfase acuosa se forma una nueva interfase, donde los índices de refracción son n_{aire} y $n_{monocapa}$, y en la que el ángulo Brewster disminuye ligeramente. En estas condiciones, y si mantenemos el ángulo de incidencia original, parte de la luz se refleja, debido únicamente a la presencia de la monocapa. Si, a continuación, esta radiación es recogida por una cámara, podemos observar directamente la morfología de la película durante su proceso de formación. Además, su posterior análisis puede aportar valiosa información acerca de la organización molecular dentro de la película. Así, por ejemplo, teniendo en cuenta que la polarizabilidad de una cadena hidrocarbonada extendida es mayor a lo largo del eje que perpendicular al mismo, la anisotropía óptica de los dominios puede ser observada mediante BAM.

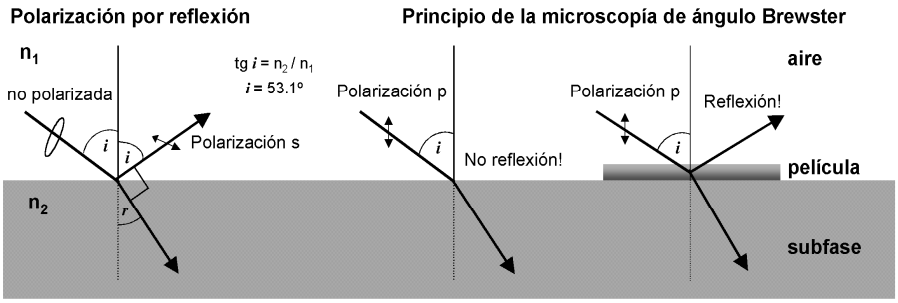

Figura 1.4

Esta técnica, frente a otras como la microscopía de fluorescencia, ofrece mayor contraste en aquellos dominios con diferente orientación azimutal,[12] además de no

necesitar una sonda fluorescente que añadir a la película.

- ***Difracción de rayos X de incidencia rasante (GIXD):*** La difracción de rayos X de incidencia rasante es una técnica de caracterización microestructural de películas en la interfase aire-agua que usa una fuente de rayos X de alta intensidad, que inciden en la película de forma casi paralela a dicha interfase. Esta técnica fue introducida por Kjaer y Dutta et al.[20-22] y se ha establecido como una poderosa herramienta para estudiar el empaquetamiento de moléculas anfifílicas en la interfase aire-agua.

Los rayos X de alta intensidad se generan por la colisión de positrones en un acelerador de partículas tipo sincrotrón (línea BW1, HASYLAB, DESY, Hamburgo), y son convertidos en un rayo monocromático (λ=1.3038Å) gracias a un cristal monocromador de Be. Este rayo se hace incidir sobre la monocapa a un ángulo de incidencia de $\alpha_i=0.85\alpha_c$, siendo $\alpha_c\approx0.13^o$ el ángulo crítico para la reflexión total. Sólo los primeros 80 Å por debajo de la superficie del agua son iluminados, para mejorar la sensibilidad de las monocapas y eliminar ruido de fondo. Con un detector sensible a la posición lineal se recoge la luz difractada en función del ángulo de dispersión vertical α_f. El ángulo de dispersión en el plano (horizontal) 2Θ se varía rotando todo el dispositivo detector.

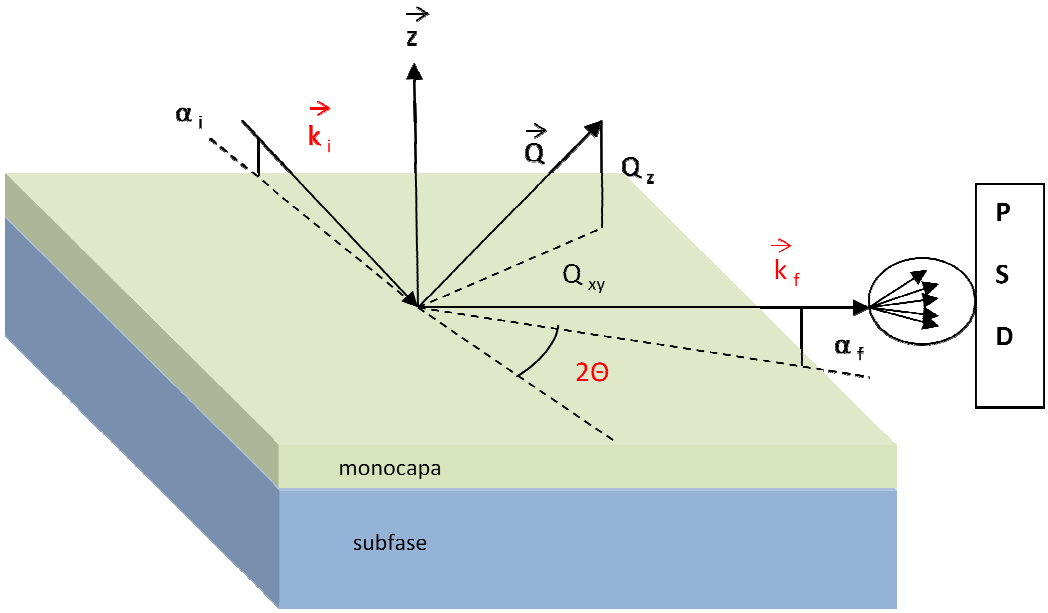

Figura 1.5

Las componentes horizontal (Q_{xy}) y vertical (Q_z) del vector de dispersión se pueden expresar en la forma:

$$Q_{xy} \approx \frac{4\pi}{\lambda} \sin\frac{2\Theta}{2} \qquad (1.5) \qquad\qquad Q_z \approx \frac{2\pi}{\lambda} \sin\alpha_f \qquad (1.6)$$

donde λ es la longitud de onda de los rayos X. La intensidad de la radiación detectada se corrige en función de la polarización, el área efectiva y el factor de Lorentz. Los picos obtenidos en la dirección del plano se ajustan por mínimos cuadrados a una curva Lorentziana y los fuera del plano a una Gaussiana. La semianchura (anchura a mitad del máximo, AMM) de los picos obtenidos en la dirección del plano está relacionada con la longitud de correlación *l*, es decir, la extensión de la red cristalina, en la forma[23]: *l=2/AMM*. Los picos obtenidos en la dirección fuera del plano son llamados "barras de Bragg", y su anchura es inversamente proporcional a la longitud de la molécula. Por la posición de los picos en la dirección en el plano (horizontal), se puede determinar el espaciamiento de red:

$$d(hk) = \frac{2\pi}{Q_{xy}^{hk}} \qquad (1.7)$$

donde (h, k) indica el orden de reflexión. Los parámetros de red *a*, *b* y el ángulo γ se pueden estimar desde el espaciamiento de red *d(hk)*, pudiendo calcular el área por celda unidad A_{xy}:

$$A_{xy} = a \cdot b \cdot \sin\gamma \qquad (1.8)$$

Las moléculas anfifílicas sólo se pueden empaquetar en un número limitado de redes cristalinas: hexagonal, ortorrómbica y oblicua. En una red hexagonal, las cadenas están normalmente perpendiculares a la interfase, con unos parámetros de red a=b y γ=120º. Cuando las cadenas están inclinadas totalmente de forma simétrica es una fase ortorrómbica, y sólo dos picos de Bragg son detectados. Cuando la inclinación es intermedia tenemos una fase oblicua, y se pueden ver tres picos de difracción.

- ***Reflectividad especular de rayos X (XRR)*:** Las medidas de reflectividad especular de rayos X se realizan en el mismo instrumento que las de difracción GIXD. Para las medidas de reflectividad, los ángulos del rayo incidente α_i y reflejado α_f son

iguales, y se varían en el rango $0.5\ \alpha_c < \alpha_i\ (\alpha_f) < 30\ \alpha_c$, donde $\alpha_c = 0.13^o$. La luz reflectada es medida con un detector de centelleo de NaI en el plano del rayo incidente, en función del vector de dispersión fuera del plano Q_z.

En el caso de una interfase ideal y bien definida entre gas y líquido, la reflectividad ($R_f(Q)$) es simplemente una reflectividad tipo Fresnel. Una monocapa de grosor d modula la reflectividad en vectores de onda del orden de π/d y superiores. La reflectividad medida (R), dividida por la reflectividad de Fresnel viene dada por la fórmula[24]:

$$\frac{R}{R_f} = \frac{1}{\rho_w^2}\left|\rho'(z) \cdot e^{iQ_z z} dz\right|^2 \qquad (1.9)$$

donde ρ_w es la densidad electrónica del agua, ρ' el gradiente de densidad electrónica a lo largo del vector normal Q_z. En realidad la interfase entre dos fases no está matemáticamente bien definida. La rugosidad molecular, σ, es del orden de los 3 Å y está causada principalmente por excitaciones térmicas en la superficie del agua. Es por ello que hay que introducir el factor Debye-Waller ($e^{-Q_z^2\sigma^2}$) en la fórmula.

No se puede aplicar directamente una transformada de Fourier a la reflectividad para obtener la distribución de densidad electrónica, porque se mide el cuadrado absoluto de un número complejo y no la fase. Por este motivo la reflectividad medida tiene que ser ajustada a un perfil de densidad con un número de parámetros ajustable: el modelo de cajas.

En una versión simplificada del modelo de cajas, la monocapa de Langmuir es considerada como dos cajas que representan la región de las cadenas alifáticas y el grupo polar, con densidades electrónicas constantes. Este modelo tiene 4 parámetros ajustables: altura (densidad) y anchura (longitud de los segmentos) de las dos cajas, y un parámetro general que representa la rugosidad. Este modelo es capaz de describir satisfactoriamente la región de las colas alifáticas, aunque no es tan bueno para la determinación de la orientación y la hidratación del grupo polar.

1.2 MÉTODOS ESPECTROSCÓPICOS

1.2.1 Fuerza y Polarización de Bandas de Absorción

La intensidad de una banda de absorción electrónica suele representarse en términos de la denominada *fuerza del oscilador, f.*[25] Esta puede calcularse a partir de la integración de la banda

$$f = \frac{4\varepsilon_0 \, 2.303 m_e c_0}{N_A e^2} \int_{banda} \varepsilon d\upsilon = 1.44 \times 10^{-19} \int_{banda} \varepsilon d\upsilon \qquad (2.1)$$

donde ε es la absortividad molar, ε_0 la permitividad en el vacío, m_e y e la masa y carga del electrón, c_0 la velocidad de la luz en el vacío, y N_A el número de Avogadro. En la ecuación anterior, el factor numérico $1.44 \cdot 10^{-19}$ tiene unidades de $mol \cdot L^{-1} \cdot cm \cdot s$. La fuerza del oscilador, *f*, es una magnitud adimensional que relaciona la absorción total de una transición espectroscópica (integral de la banda) con la absorción del oscilador clásico equivalente.

Transiciones permitidas por las reglas de selección espectroscópicas dan lugar a valores de *f* del orden de la unidad. Se obtienen valores de $f << 1$ cuando la transición considerada incumple alguna de las reglas de selección.

A partir de la ecuación de Schrödinger dependiente del tiempo, es posible obtener una relación teórica para la fuerza del oscilador

$$f = \frac{8 \cdot \pi^2 m_e n g}{3 h^2 e^2 \hat{n}} M^2 \Delta E = 2.128 \times 10^{-75} \frac{n g M^2 \Delta E}{\hat{n}} \qquad (2.2)$$

donde *h* es la constante de Planck, $\hat{n}$, el índice de refracción, *g* la degeneración del estado excitado, *n* el número de electrones en el estado ocupado (HOMO), *E* la energía de la transición espectroscópica, y *M* es el módulo del vector momento dipolar de transición. En esta ecuación, el factor numérico $2.128 \cdot 10^{-75}$ tiene unidades de $C^{-2}\ m^{-2}\ J^{-1}$. La deducción de la ecuación (2.2) implica suponer que el vector momento dipolar de transición se encuentra en la dirección del campo eléctrico de la luz incidente.

El vector dipolo de transición se define como

$$\vec{M} = e\int \psi_i \vec{r}\, \psi_j d\tau = M_x \vec{i} + M_y \vec{j} + M_z \vec{k} \qquad (2.3)$$

donde Ψ_i y Ψ_j son las funciones de onda de los estados inicial y final de la transición.

La absorción de radiación depende de la orientación relativa entre la radiación incidente y el dipolo de transición. Únicamente la componente de $\vec{M}$ que oscila en la misma dirección que el campo eléctrico de la radiación, da lugar a absorción molecular. Matemáticamente esto puede expresarse mediante la relación

$$\left|\vec{\varepsilon}\cdot\vec{M}\right|^2 = \left(M_x^2 + M_y^2 + M_z^2\right)\left|\vec{\varepsilon}\cdot\vec{n}\right|^2 = M^2\left|\vec{\varepsilon}\cdot\vec{n}\right|^2 \qquad (2.4)$$

donde $\vec{\varepsilon}$ y $\vec{n}$ son los vectores característicos de la radiación incidente y de la dirección del dipolo, respectivamente. En la ecuación (2.2) se ha supuesto que el producto $\left|\vec{\varepsilon}\cdot\vec{n}\right|^2 = 1$, por lo que, en un caso general, la ecuación (2.2) debe ser modificada para tener en cuenta este efecto, multiplicándola por el factor $\left|\vec{\varepsilon}\cdot\vec{n}\right|^2$. La absorción de radiación tiene lugar cuando el producto escalar $\left|\vec{\varepsilon}\cdot\vec{n}\right|^2 \neq 0$, es decir, si dichos vectores son perpendiculares no se produce absorción. A consecuencia de este fenómeno, los sistemas moleculares organizados, tales como cristales moleculares y películas superficiales, son ópticamente activos y pueden polarizar la luz incidente. Este fenómeno puede utilizarse para determinar la orientación molecular en sistemas organizados.

1.2.2 Factor de Orientación en la Interfase Aire-Agua

Supongamos una molécula lineal, con una sola componente diferente de cero en su dipolo de transición (por ejemplo, una hemicianina). En disolución, donde la orientación es al azar, la absorción debe ser proporcional a un factor 2/3. En efecto, podemos imaginar que 1/3 de las moléculas se encuentran alineadas hacia cada uno de los ejes de coordenadas, por lo que, si la radiación incidente lo hace a lo largo de un eje determinado, solo dos de las orientaciones anteriores darán lugar a absorción de radiación. Sin embargo, si las moléculas se encuentran en la interfase aire-agua con su dipolo de transición orientado paralelo a la interfase, la absorción debe de ser proporcional a un factor 1, ya que en esta situación la molécula siempre es capaz de

absorber radiación (ver Figura 2.1). El factor de orientación se define como el cociente entre estas dos cantidades, 1/(2/3) = 3/2, lo que nos indica que, a igualdad de densidad molecular, la absorción en la interfase es 1.5 veces superior a la absorción en disolución.

Para moléculas con dos componentes de su dipolo de transición diferentes de cero (por ejemplo, porfirinas), debe aplicarse un tratamiento a las dos componentes del dipolo. Una definición general del factor de orientación debe realizarse en base a la ecuación (2.4). Supondremos el plano de la molécula orientado un ángulo θ con respecto al eje z, tal como se muestra en la Figura 2.1. Se define el vector $\vec{p}$, como el vector dirección perpendicular al plano de la molécula, siendo ϕ el ángulo entre el eje z y este vector, por lo que $\theta + \phi = \pi/2$.

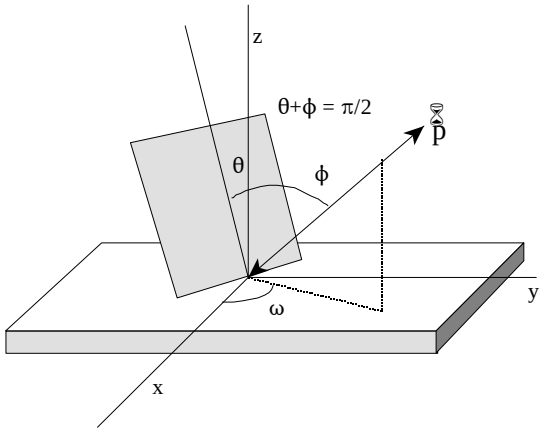

Figura 2.1

Para cada eje, la suma de las componentes al cuadrado de los dipolos, debe ser igual a uno menos la componente del vector p al cuadrado, por lo que, en este caso

$$M^2 \left| \vec{\varepsilon} \cdot \vec{n} \right|^2 = M^2 \left(\left| \vec{\varepsilon} \cdot \vec{u} \right|^2 - \left| \vec{\varepsilon} \cdot \vec{p} \right|^2 \right) \qquad (2.5)$$

siendo

$$\vec{\varepsilon} = \begin{pmatrix} 1 \\ 1 \\ 0 \end{pmatrix} \qquad \vec{u} = \begin{pmatrix} 1 \\ 1 \\ 1 \end{pmatrix} \qquad \vec{p} = \begin{pmatrix} sen(\phi)\cos(\omega) \\ sen(\phi)sen(\omega) \\ \cos(\phi) \end{pmatrix} \qquad (2.6)$$

Si el medio es isotrópico en el plano x-y (plano de la interfase), no existirá

dirección preferente de orientación con respecto al ángulo ω (ver Figura 2.1), por lo que puede escribirse que

$$\left\langle sen(\phi)^2 \cos(\omega)^2 \right\rangle + \left\langle sen(\phi)^2 sen(\omega)^2 \right\rangle = \frac{\left\langle sen(\phi)^2 \right\rangle}{2} + \frac{\left\langle sen(\phi)^2 \right\rangle}{2} = \left\langle sen(\phi)^2 \right\rangle \qquad (2.7)$$

El valor medio de sen(ϕ)^2, viene definido por

$$\left\langle sen(\phi)^2 \right\rangle = \frac{\int_0^{\pi} sen(\phi)^2 P(\phi) sen(\phi) d\phi}{\int_0^{\pi} P(\phi) sen(\phi) d\phi} \qquad (2.8)$$

donde $P(\phi)$ representa la función de distribución de los dipolos con respecto al ángulo ϕ (ver Figura 2.1). En disolución, debe existir también isotropía con respecto al eje z, por lo que $P(\phi)$ es constante y puede escribirse

$$\left\langle sen(\phi)^2 \right\rangle_{\text{disolución}} = \frac{P(\phi)\int_0^{\pi} sen(\phi)^2 sen(\phi) d\phi}{P(\phi)\int_0^{\pi} sen(\phi) d\phi} \qquad (2.9)$$

De esta forma, el factor de orientación viene dado por

$$f_0 = \frac{\left|\vec{\varepsilon}\cdot\vec{n}\right|^2_{\text{aire-agua}}}{\left|\vec{\varepsilon}\cdot\vec{n}\right|^2_{\text{disolucion}}} = \frac{2-\left\langle sen(\phi)^2 \right\rangle_{\text{aire-agua}}}{2-\left\langle sen(\phi)^2 \right\rangle_{\text{disolucion}}} = \\ = \frac{3}{4}\left(1+\left\langle \cos(\phi)^2 \right\rangle_{\text{aire-agua}}\right) = \frac{3}{4}\left(1+\left\langle sen(\theta)^2 \right\rangle\right) \qquad (2.10)$$

Si la orientación es homogénea, es decir, si todos los dipolos tienen el mismo ángulo θ de inclinación, $P(\phi)$ será una función discontinua, tal que sólo es diferente de cero para dicho ángulo, en este caso $\left\langle sen(\theta)^2 \right\rangle = sen(\theta)^2$, cumpliéndose:

$$f_0 = \frac{3}{4}\left(1 + sen(\theta)^2\right) \qquad (2.11)$$

En caso contrario, es decir, cuando la distribución de los dipolos no es homogénea, esta sustitución no puede ser realizada. En la interfase aire-agua, las películas superficiales homogéneas de cromóforos muestran, en general, una orientación preferente. Dicha orientación, además, puede ser alterada modificando la presión superficial. En estos casos, la determinación del factor de orientación permite obtener información cuantitativa del grado de inclinación de los dipolos.

1.2.2.1 Fuerza del Oscilador Aparente en la Interfase Aire-Agua

Con frecuencia la reflexión suele expresarse de una forma normalizada. Si se tiene en cuenta que

$$\Gamma = \frac{10^{14}}{N_A S} \qquad (2.12)$$

donde *S* corresponde al área ocupada por molécula en la interfase, expresada en nm^2, es posible escribir la expresión (1.4), dada en la Sección 1 de esta Introducción, como

$$\Delta R = 2.303\times10^3\, f_0 \varepsilon \sqrt{R_S}\,\Gamma = \frac{2.303\times10^{17}\, f_0 \varepsilon}{N_A S}\sqrt{R_S} \qquad (2.13)$$

lo que nos permite definir la reflexión normalizada como

$$\Delta R_{norm} = S \times \Delta R = \frac{2.303\times10^{17}\, f_0 \varepsilon}{N_A}\sqrt{R_S} = 5.545\times10^{-8}\, f_0 \varepsilon \qquad (2.14)$$

donde se ha utilizado $\sqrt{R_S} = 0.145$, y ΔR_{norm} posee unidades de nm^2/molécula.

La combinación de las ecuaciones (2.1) y (2.14) nos propone un procedimiento para el cálculo de la fuerza del oscilador a través de la integración de la banda de reflexión normalizada

$$f = \frac{1.44\times10^{-19}}{5.545\times10^{-8}\, f_o} \int_{banda} \Delta R_{\text{norm}} d\upsilon = \frac{2.6\times10^{-12}}{f_0} \int_{banda} \Delta R_{\text{norm}} d\upsilon \qquad (2.15)$$

Sin embargo, el factor de orientación es una magnitud desconocida a priori, por lo que conviene definir una fuerza del oscilador aparente mediante la relación:

$$f_{\text{ap}} = f \times f_0 = 2.6\times10^{-12} \int_{banda} \Delta R_{\text{norm}} d\upsilon \qquad (2.16)$$

donde el factor $2.6\cdot10^{-12}$ tiene unidades de nm^{-2} s. Hay que indicar que, en la anterior definición *f* es la fuerza del oscilador en disolución (condiciones isotrópicas).

Las disminuciones de ΔR_{norm} o f_{ap} con el aumento de la presión superficial en la interfase aire-agua pueden ser relacionadas con dos fenómenos: bien con una pérdida de cromóforo hacia la subfase acuosa, o bien con una reorientación del dipolo de transición. Por lo tanto, cuando la pérdida de cromóforo puede ser descartada, las variaciones de ΔR_{norm} o f_{ap} con el área superficial permiten determinar la orientación del dipolo de transición.

1.2.3 Absorción de Radiación y Agregación Molecular: Modelo de los Dipolos Extendidos

La mayor parte de las propiedades espectroscópicas de los agregados moleculares son consecuencia de las propiedades individuales de las moléculas. Sin embargo, a pesar de que en estos sistemas la energía de interacción es débil, es posible observar grandes diferencias entre los espectros de absorción de la molécula aislada y del agregado molecular. Estas diferencias se deben al acoplamiento entre los momentos dipolares de transición de cada molécula. Así, cuando una molécula es excitada electrónicamente en el seno de un agregado molecular, dicho estado puede ser transportado a moléculas vecinas de forma que es compartido colectivamente, en mayor o menor medida, por el agregado. El hecho de que el estado excitado tenga cierta movilidad permite introducir, como concepto teórico, la existencia de una *cuasi-partícula* asociada a dicho movimiento. A dicha *cuasi-partícula* se le denomina *excitón*.

Los complejos de transferencia de carga, excímeros, polarones, bipolarones, y los denominados agregados H y J son, entre otros, ejemplos de *excitones*.[26]

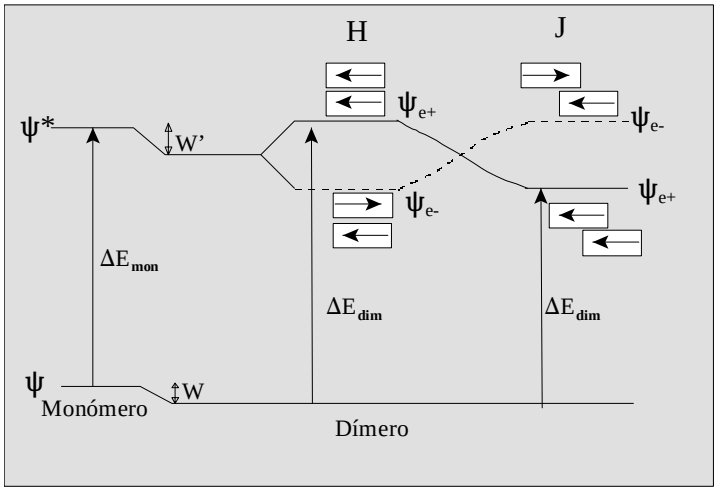

Figura 2.2

Supongamos una molécula aislada, siendo ψ y ψ^* las funciones de onda de su estado fundamental y de su primer estado excitado, respectivamente, y ΔE_{mon} la energía correspondiente a la transición espectroscópica entre ambos (parte izquierda de la Figura 2.2).

En el caso más simple, nuestro agregado estará formado solo por dos moléculas idénticas (dímero físico o de van der Waals). Si ψ_1 y ψ_2 son las funciones de onda fundamentales de estas moléculas, el producto $\psi_1\psi_2$ representará, de forma aproximada, la función de onda fundamental del agregado. Supongamos ahora que una de las dos moléculas es excitada electrónicamente, y que $\psi_1^*\psi_2$ y $\psi_1\psi_2^*$ representan estas dos opciones. En principio ambas moléculas tienen la misma probabilidad de ser excitadas y, de hecho, el estado excitado es compartido entre ambas. La función de onda de este estado excitado compartido (excitón), puede ser representada mediante una combinación lineal de las dos opciones anteriores. El método variacional de la Mecánica Cuántica nos enseña que, en estos casos, son posibles dos combinaciones lineales diferentes y, por lo tanto, dos estados excitados diferentes representados por las funciones:

$$\psi_{e\pm} = \frac{1}{\sqrt{2}}\left(\psi_1\psi_2^* \pm \psi_2\psi_1^*\right) \qquad (2.17)$$

Si las dos moléculas interaccionan mediante un operador energía V_{12}, las energías de los estados ψ_{e+} y ψ_{e-} dependen de la denominada integral de interacción resonante la cual tiene la forma:

$$J = \int \psi_1^* \psi_2 V_{12} \psi_2^* \psi_1 d\tau \qquad (2.18)$$

por lo que la energía correspondiente a la transición espectroscópica en el dímero puede ser expresada mediante la relación[26]

$$\Delta E_{\text{dim}} = \Delta E_{\text{mon}} + \Delta W + 2J \qquad (2.19)$$

donde $\Delta W = W' - W$ (ver Figura 2.2) da cuenta de las diferentes energías de interacción electrostáticas que puedan existir entre los estados excitados y fundamental de las moléculas. En este término se suelen incluir otras componentes no tenidas en cuenta, tales como fuerzas de dispersión y/o solapamiento entre orbitales. Sin embargo, y con frecuencia, este término suele despreciarse. El factor 2 que multiplica a J en la ecuación anterior procede del hecho de que el orbital HOMO está doblemente ocupado.[27]

La integral de la ecuación (2.18) representa la energía de interacción entre los dos momentos dipolares de transición, M, de cada molécula. Este hecho permite evaluar dicha integral, de forma aproximada, sustituyéndola por su equivalente clásico, es decir, por la energía de interacción entre dos osciladores clásicos acoplados. El método consiste en suponer que cada molécula puede ser representada por su dipolo de transición M, y que este puede ser expresado mediante la relación $M = qP$, donde q es la separación de carga y P la longitud del dipolo formado (ver Figura 2.3). La energía de interacción entre las moléculas será por lo tanto

$$J = \frac{q^2}{\varepsilon}\left(\frac{1}{a_1} + \frac{1}{a_2} - \frac{1}{a_3} - \frac{1}{a_4}\right) \qquad (2.20)$$

donde ε es la constante dieléctrica del medio ($\varepsilon \approx 2.5$), a_1 y a_2 representan las distancias entre cargas del mismo signo y, a_3 y a_4 las distancias entre cargas de signo opuesto, tal

como se muestra en la Figura 2.3. La sustitución de la integral (2.18) por la expresión (2.20), constituye la base de la denominada aproximación de los *dipolos extendidos*.[27]

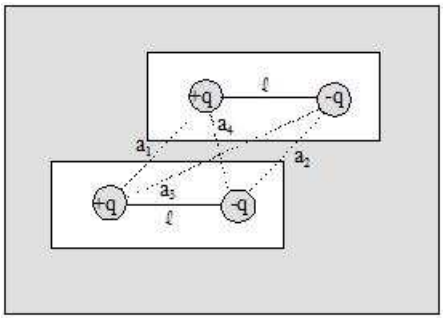

Figura 2.3

Para *r* >> *P*, siendo *r* la distancia entre los centros geométricos de las moléculas (ver Figura 2.4), es posible simplificar la ecuación anterior, ya que

$$q^2\left(\frac{1}{a_1}+\frac{1}{a_2}-\frac{1}{a_3}-\frac{1}{a_4}\right)\approx\frac{q^2l^2}{r^3}=\frac{M^2}{r^3} \qquad (2.21)$$

Esta expresión es válida para un ángulo $\theta = 0$. En general, para cualquier ángulo se cumple que (ver Figura 2.4):

$$J\approx\frac{M^2}{\varepsilon r^3}\left(1-3\cos\left(\theta\right)^2\right) \qquad (2.22)$$

A su vez, la expresión anterior es la base de la denominada aproximación de los *dipolos puntuales*.[28-29] Dada la sencillez de esta última, la utilizaremos como referencia para definir los conceptos de agregados H y J.

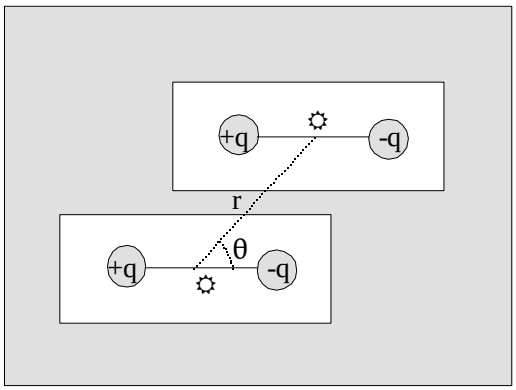

Figura 2.4

Supongamos que nuestro agregado (dímero) posee una estructura apilada en la que θ = 90º (ver Figura 2.4). Esta estructura está representada, asimismo, en la parte central de la Figura 2.2, y será denominada agregado H. Si utilizamos el símil clásico, donde las moléculas pueden ser representadas por dipolos oscilantes, el estado ψ_{e+} correspondería a un acoplamiento paralelo de dichos osciladores. Es decir, las cargas positivas y negativas oscilan en el mismo sentido, lo que da lugar a una cierta energía de repulsión y, por lo tanto, a una situación de mayor energía que la correspondiente al monómero en estado excitado (ver Figura 2.2). Esta situación corresponde a un valor positivo de la integral *J* (ecuación 2.22).

Por el contrario, el estado ψ_{e-} corresponde a un acoplamiento antiparalelo en el que las cargas oscilan en sentido contrario, lo que da lugar a una situación de menor energía (integral *J* negativa). Puesto que el dipolo de transición del agregado es suma de los correspondientes a los monómeros, la resultante para ψ_{e-} es cero, lo que significa que este estado no es activo desde el punto de vista espectroscópico y, por lo tanto, no da lugar a banda de absorción. Este hecho es indicado en la Figura 2.2 mediante línea de puntos. Hay que indicar que esto es cierto solo si las moléculas están orientadas en la misma dirección, en caso contrario los dos estados, ψ_{e+} y ψ_{e-}, serían activos.

Una característica, por lo tanto, de los agregados H, es que la banda de absorción tiene lugar a mayor energía que la del monómero (desplazamiento hacia el azul, ver Figura 2.2).

Supongamos ahora que el dímero posee una estructura en la que $\theta \rightarrow 0^{\circ}$ (ver Figura 2.4). Esta estructura es representada a la derecha de la Figura 2.2, y será denominada agregado J. En este caso, las energías de los estados electrónicos se invierten con respecto a la situación anterior. En efecto, cuando el acoplamiento de los

osciladores es paralelo (estado ψ_{e+}), estos se atraen, lo que da lugar a una cierta disminución de la energía (integral $J < 0$). Por el contrario, cuando el acoplamiento es antiparalelo (estado ψ_{e-}), los osciladores se repelen, dando lugar a un aumento de energía (integral $J > 0$).

Es decir, la principal característica de los agregados J es que su banda de absorción tiene lugar a menor energía que la del monómero. Esta propiedad de ciertos agregados moleculares fue detectada, por vez primera y simultáneamente, por Scheibe[30] y por Jelly,[31] y así son referidos como agregados de Scheibe o agregados J.

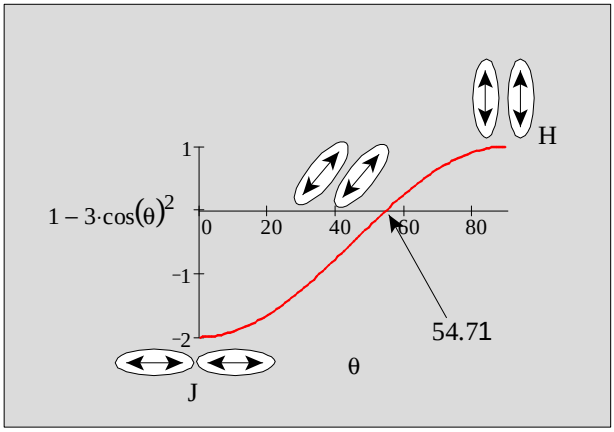

Figura 2.5

La transición entre un agregado H y J puede ser analizada de una forma simplificada a través de la ecuación (2.22). En la Figura 2.5, se representa la función 1-3cos(θ)^2 *vs* θ. Esta función es cero para $\theta = 54.7^o$, por lo que teóricamente a este ángulo, no debe de existir desplazamiento en la banda de absorción del dímero con respecto al monómero (suponiendo $\Delta W = 0$ en la ecuación 2.19). Para $\theta > 54.7^o$ dominan las fuerzas de repulsión y el agregado es H, mientras que para $\theta < 54.7^o$ dominan las fuerzas de atracción y el agregado es J.

La definición anterior de agregados H y J, en base al modelo de dipolos puntuales, está limitada al cumplimiento de la relación $r >> P$. El empleo de la ecuación (2.22) de forma generalizada, en sustitución del modelo de los dipolos extendidos (ecuación 2.20), puede conducir a errores considerables en la interpretación de los resultados. En la Figura 2.6, se muestra un ejemplo de esta afirmación. En la parte izquierda de esta figura se representan los planos de las moléculas y sus centros geométricos separados una distancia *b* y *d*, respectivamente. Con estas consideraciones, y suponiendo que la longitud del dipolo es *l*, es posible definir

$$r = a_1 = a_2 = \sqrt{b^2 + d^2} \qquad (2.23)$$

$$\theta = ar\cos\left(\frac{d}{r}\right) \qquad (2.24)$$

$$a_3 = \sqrt{(\ell + d)^2 + b^2} \qquad (2.25)$$

$$a_4 = \sqrt{(\ell - d)^2 + b^2} \qquad (2.26)$$

Suponiendo que l y b son conocidos, y dando valores a su vez al parámetro d, es posible calcular r (ec. 2.23), θ (ec. 2.24), así como todas las distancias a_i. De esta forma, es posible determinar la relación $J\varepsilon/q^2$, ya sea según el modelo de los dipolos puntuales (ec. 2.20) o el de los dipolos extendidos (ec. 2.22).

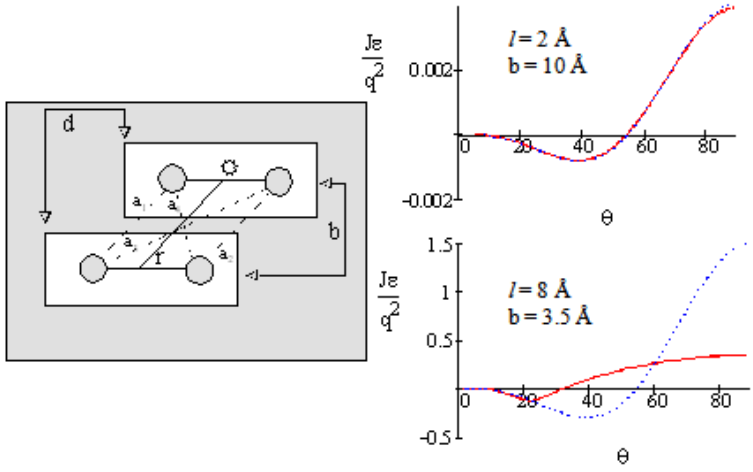

Figura 2.6

En la parte derecha de la Figura 2.6 se muestran dos ejemplos de aplicación de las anteriores expresiones. Así, cuando l = 2 Å y b = 10 Å, los valores de $J\varepsilon/q^2$ para el modelo de los dipolos puntuales (línea azul de puntos) y de los dipolos extendidos (línea roja continua) coinciden prácticamente, como cabe esperar de la relación $r > P$.

Sin embargo, cuando l = 8 Å y b = 3.5 Å, valores que están dentro del rango de los encontrados experimentalmente,[27,32] la variación de $J\varepsilon/q^2$ para ambos modelos es muy diferente. En concreto, la transición entre agregados H y J se sigue produciendo en el modelo de los dipolos puntuales (línea azul de puntos) a un ángulo de θ = 54.7º, mientras que en el modelo de los dipolos extendidos (línea roja continua) dicha transición tiene lugar a θ = 31.9º. Es decir, en este caso, el modelo de los dipolos puntuales no es capaz de predecir correctamente las regiones en las que dominan las fuerzas atractivas y repulsivas entre dipolos. Asimismo, el modelo de los dipolos puntuales exagera la energía de repulsión entre dipolos.

En la Figura 2.6 se observa como $J\varepsilon/q^2$ tiende a cero, cuando θ tiende a cero. En realidad $\theta = 0^o$ sólo cuando $d = 4$ y, por lo tanto, la energía de interacción entre dipolos es cero.

Aparte de las ventajas obvias del modelo de los dipolos extendidos, tiene sin embargo, un inconveniente práctico que hace que este modelo haya sido poco utilizado. En efecto, a partir de la integración de la banda de absorción del monómero en disolución, es posible determinar el valor del módulo del momento dipolar de transición *M*, pero no de *q* y *l* por separado. La determinación de estos valores necesita de un dato experimental adicional. Así, se necesita conocer el desplazamiento de la banda de absorción para un agregado de estructura conocida.

En cualquier caso, la aplicación cuantitativa de ambos modelos necesita del conocimiento previo de algunos parámetros estructurales del agregado, como es la separación entre los planos moleculares. Con frecuencia dicha estructura solo puede ser conocida mediante espectros de difracción de rayos X, si bien, en ocasiones, puede obtenerse información estructural a partir de otros tipos de experimentos. Así, por ejemplo, la determinación de áreas superficiales en la interfase aire-agua en unión con los propios datos espectroscópicos, permite, en situaciones favorables, deducir dicha información.

Para analizar un ejemplo supongamos que, para un determinado cromóforo se observa que el máximo de su banda de absorción se desplaza desde λ_{mon} = 351 nm, para el monómero, hasta λ_{dim} = 339 nm para el dímero. Supongamos además que la integración de la banda del monómero en disolución ha permitido obtener que $M = q \cdot l = 2.56 \cdot 10^{-29}$ C m = 7.7 *D*. A partir de la ecuación (2.19), y suponiendo que $\Delta W = 0$, es posible calcular

$$J = \frac{hc10^7}{2}\left(\frac{1}{\lambda_{dim}} - \frac{1}{\lambda_{mon}}\right) = 10^{-13} erg \qquad (2.27)$$

Si suponemos que la geometría del dímero es similar a la mostrada en la Figura 2.6, es posible combinar las ecuaciones (2.32), (2.35)-(2.38) de forma que

$$J = \frac{M^2}{\ell^2 \varepsilon}\left[\frac{2}{\sqrt{b^2+d^2}} - \frac{1}{\sqrt{(\ell+d)^2+b^2}} - \frac{1}{\sqrt{(\ell-d)^2+b^2}}\right] \qquad (2.28)$$

Si *b* y *d* son conocidas, la ecuación anterior posee una sola incógnita, la longitud del dipolo, *l*, la cual puede ser determinada numéricamente. Así, cuando *b* = 4 Å y *d* = 0, se obtiene, para el ejemplo anterior, *l* = 5.73 Δ y *q* = 0.278 *e*, donde *e* representa la carga de un electrón.

1.3 CALIXARENOS

1.3.1 Antecedentes

Los calixarenos son macrociclos compuestos de unidades fenólicas conectadas por grupos metileno que forman una cavidad hidrofóbica es capaz de formar complejos de inclusión con una amplia variedad de moléculas. Estas moléculas fueron sintetizadas en primer lugar por Adolph von Baeyer como productos de la reacción de fenol con aldehídos en presencia de ácidos fuertes. El trabajo pionero de C. David Gutsche a finales de los 70 condujo a un renovado interés por la química de los productos de la reacción fenol-formaldehído, y a la denominación de tales productos como *calixarenos*.[33] Derivado de la palabra griega *calix* que significa jarrón, y *arene* que indica la presencia de anillos aromáticos, los calixarenos han sido sintetizados con un gran número de tamaños. Un número entre corchetes, situado entre la palabra *calix* y *arene* indica el número de unidades fenólicas enlazadas por puentes metileno que forman la cavidad de la molécula. La substitución de los anillos aromáticos es especificada por prefijos apropiados. La Figura 3.1 ilustra la nomenclatura del calixareno

Si n = 3, y R = *t*-butil el nombre del compuesto es *p*-*tert*-butilcalix[6]arene

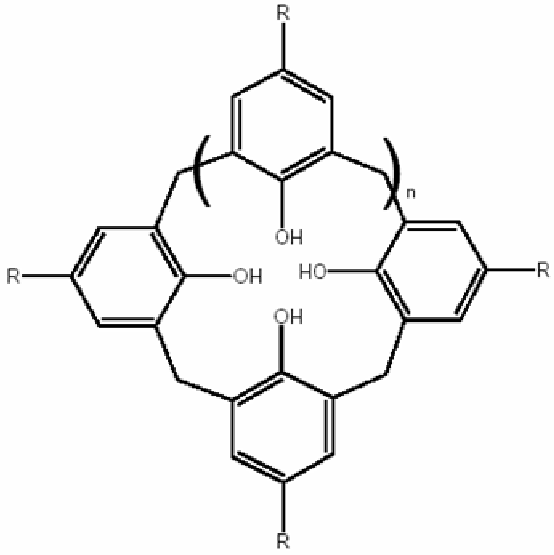

Figura 3.1: Esquema de nomenclatura de los calixarenos.

La motivación detrás de los experimentos de Gutsche fue la posibilidad de que la forma toroidal de los calixarenos podría ser adecuada para fabricar estructuras que imitaran a enzimas. Las enzimas son altamente específicas tanto para las reacciones que catalizan como para la elección de los sustratos. Los calixarenos poseen una cavidad bien definida con propiedades polares (anillo inferior) y no polares (anillo superior). Además, se pueden obtener derivados dependiendo del tamaño de la cavidad y los grupos funcionales con el objetivo de producir compuestos selectivos a los analitos y capaces de formar complejos de inclusión. Por consiguiente, su aplicabilidad a la química bioorgánica fue un importante trampolín para otros muchos investigadores interesados en la química del calixareno.

1.3.2 Características Estructurales

La estructura básica de un calixareno consiste en la repetición de unidades fenólicas enlazadas por grupos metileno para formar una inconfundible cavidad con forma cilíndrica. El lado más ancho de la cavidad está definido como el anillo superior, y el más estrecho es el anillo inferior.[34] Debido a que se pueden derivatizar fácilmente, numerosos esquemas de reacción dan lugar a estos compuestos con una gran variedad de propiedades químicas. Se conocen calixarenos que poseen desde tres hasta veinte unidades fenólicas.[35] La mayoría de los estudios se centran en los derivados calix[4]arenos, calix[6]arenos, y calix[8]arenos. Un factor común a todos los informes es la retención de la cavidad del calixareno. Los tamaños de la cavidad de los

calix[4]arenos, calix[6]arenos, y calix[8]arenos son de 3.0, 7.6, y 11.7 $Å^2$, respectivamente.[36]

La orientación espacial de cada unidad fenólica da origen al tipo de conformación la cual es función de las condiciones de reacción, el número de fenoles enlazados conjuntamente, el tipo de sustituyentes, y algunas veces la longitud del enlace entre los fenoles.[37] Los compuestos originales sin sustituir del calix[4]areno, poseen una conformación en forma de silla con dos anillos aromáticos en un plano y los otros dos a ángulos rectos.[38] La rotación de los grupos metileno entre fenoles da origen a las distintas conformaciones en los calixarenos substituidos. Por ejemplo, los *p-tert*-butilcalix[4]arenos con frecuencia adoptan la conformación cono, cono parcial, 1,2-alternado, o 1,3-alternado.[34] La Figura 2 muestra una representación simplificada de cada conformación. Por convención cuando todos los anillos fenólicos están apuntando hacia arriba la conformación es cono. Cuando uno o dos anillos están señalando hacia abajo, la conformación es cono parcial. Las medidas de resonancia magnética nuclear del protón (^{1}H-RMN) de varios calixarenos en disolución muestran que principalmente aparecen en la conformación cono, pero a temperatura ambiente es posible modificar la conformación.[39]

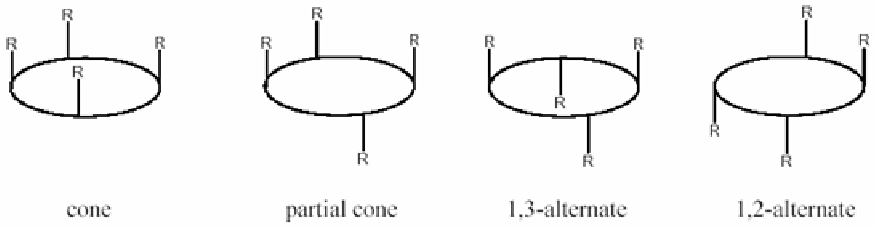

Figura 3.2: Conformaciones de calix[4]arenos sustituidos.

La flexibilidad del calixareno puede ser controlada por cristalización, lo cual permite fijar una conformación en el estado sólido. El control sobre la conformación puede ser alcanzado mediante derivatización del anillo superior o inferior con grupos voluminosos los cuales inhiban la rotación de las unidades fenólicas. Por ejemplo, la unión intramolecular de unidades fenólicas a través de los sustituyentes puede formar compuestos "puenteados"[40] o incluso totalmente cerrados,[41] dependiendo del tamaño del separador. La unión intermolecular da origen a calixarenos dobles los cuales pueden poseer puentes simples[42] o dobles.[43] Se ha llegado a informar de dos calix[6]arenos enlazados por seis puentes.[44]

1.3.3 Otras Propiedades Físicas

Las medidas del punto de fusión del calixareno permiten calcular rápidamente su pureza. La mayoría de los calixarenos tienen puntos de fusión por encima de 250 ºC. Incluso ligeras diferencias entre isómeros dentro de los grupos sustituyentes pueden acarrear dramáticas diferencias en los puntos de fusión de los derivados de calixareno.[45] Estas mismas diferencias pueden afectar a la solubilidad. Los calixarenos más comunes son insolubles en agua, debido a sus componentes aromáticos. Además la solubilidad en disolventes orgánicos es limitada, de este modo resulta compleja su purificación y caracterización. Sin embargo la mayoría son suficientemente solubles para permitir el análisis espectral en un limitado número de disolventes orgánicos. De nuevo, la derivatización puede ser empleada para inducir diferentes solubilidades. Se cumple con bastante precisión que la solubilidad en disolventes orgánicos es incrementada por aquellos sustituyentes que tienden a disminuir el punto de fusión.[46]

A pesar de su baja solubilidad en disolventes orgánicos, se han estudiado las propiedades espectrales de los calixarenos usando espectroscopia infrarroja (IR), ultravioleta (UV), resonancia magnética nuclear (RMN), cristalografía rayos-X, espectrometría de masas (SM), y de fluorescencia. Cada técnica nos proporciona información valiosa sobre la estructura de los calixarenos y otras propiedades usando diferentes tipos de radiación.

Un rasgo espectral distintivo del espectro IR de los calixarenos es la baja frecuencia de vibración de los grupos OH, variando desde 3150 cm^{-1} hasta 3300 cm^{-1}, dependiendo del tamaño de la molécula. Esto es atribuido a los intensos puentes de hidrógeno intramoleculares formados por los grupos hidroxilo del anillo inferior. Los puentes de hidrógeno circulares[47] son más fuertes en el tetrámero y más débiles en el pentámero.[48]

Un par de máximos de absorción cerca de 280 y 288 nm aparecen en el espectro UV de los calixarenos. La relación de intensidades a estas dos longitudes de onda es una función del tamaño del calixareno, 1.30, 0.90, y 0.75 para los derivados *p-tert*-butil del calix[4]areno, calix[6]areno, y calix[8]areno, respectivamente. La absortividad molar (ε_{max}, $L \cdot mol^{-1} \cdot cm^{-1}$) varía desde 9800 hasta 23100 a 280 nm y de 7700 a 32000 a 288 nm, con el incremento del tamaño del calixareno. Los espectros de RMN del calixareno son relativamente simples, debido a que la molécula es simétrica. La región de 3.5-5 ppm en los espectros ^{1}H RMN proporciona un patrón muy claro para el análisis

conformacional, debido a que los puentes metileno se ven afectados por la mayoría de los cambios conformacionales. En la conformación cono, ningún protón está situado dentro de la cavidad. Esto origina un patrón de desplazamiento en el espectro ^{1}H del calix[4]areno, un par de dobletes centrados en 3.2 y 4.9 ppm. Los patrones para el resto de confórmeros son los siguientes: cono parcial, dos pares de dobletes (relación 1:1) o un par de dobletes y un singlete (relación 1:1); 1,2-alternada, un singlete y dos dobletes (relación 1:1); y 1,3-alternada, un singlete. Los grupos OH originan un singlete que varía entre 8-10 ppm dependiendo del tamaño del calixareno, pero que no está relacionado con la fuerza del puente de hidrógeno circular.

La cristalografía de rayos X proporciona pruebas definitivas sobre la estructura de los calixarenos. El primer ejemplo apareció en 1979 cuando Andreetti y colaboradores de la universidad de Parma, Italia, publicaron los datos de un cristal simple del calix[4]areno.[49] La espectrometría de masas ha sido satisfactoriamente usada para determinar los pesos moleculares de los calixarenos. La espectroscopia de fluorescencia ha sido también usada como herramienta útil para obtener información de la capacidad complejadora de los calixarenos y de los microambientes en los complejos de calixareno.

1.3.4 Monocapas y Multicapas de Calixarenos

Las películas que están formadas total o parcialmente por calixarenos han sido ampliamente investigadas en los últimos años. La capacidad de tales películas para adsorber tanto iones como especies neutras ha motivado el interés particular de su uso como dispositivos sensores. Típicos ejemplos de su uso potencial son como sistemas semiconductores, óptica no lineal, materiales piroeléctricos, o almacenamiento de datos.

La formación de monocapas por adsorción o (auto) ensambladas en interfases requiere normalmente de molécula con cadenas largas con diferentes grupos funcionales en cada lado (por ejemplo, ácido esteárico para películas de Langmuir-Blodgett, o tioles alcano para ensamblados sobre oro). Cuando el calix[4]areno es fijado en la conformación cono se presentan dos extremos diferenciados, los grupos fenólicos hidroxi (junto con sus residuos enlazados) y las posiciones para (con sus sustituyentes) los cuales pueden ser independientemente funcionalizados.

Para la formación de películas de Langmuir es necesario el uso de calixarenos anfifílicos, es decir, calixarenos que posean en su estructura tanto sustituyentes hidrofóbicos como hidrofílicos.

Los calixarenos sin sustituir pueden ser considerados moléculas anfifílicas.[50] Sin embargo existen algunas controversias sobre si simples *p-tert*-butilcalix[n]arenos forman monocapas LB estables.[51-52] Los calixarenos más grandes pueden llegar a mantener alguna movilidad conformacional dentro de las monocapas, aunque no es un factor que haya sido investigado sistemáticamente.[53] Para mejorar la estabilidad de las monocapas de calix[n]arenos la principal herramienta es la introducción de sustituyentes que acentúen el carácter anfifílico de la molécula. Los calix[4,6]arenos sustituidos con 4-alquilfenilazo tienen mayor cantidad de grupos OH ácidos que los alquilcalixarenos y por lo tanto un mayor carácter anfifílico, formando así estables monocapas que muestran aumentos en el área límite y en la presión de colapso al incrementar el pH.[54]

Las medidas de área superficial muestran que los derivados sustituidos simétricamente se orientan en la interfase con el eje de la conformación cono perpendicular a la interfase, sin embargo en los derivados menos simétricos, tanto la orientación como la estabilidad parecen depender del patrón de sustituciones.[55]

El pH de la subfase acuosa es un elemento muy importante en la formación de monocapas de calixarenos con grupos susceptibles de protonarse o deprotonarse. Por ejemplo, el *p-tert* butilcalix[4]areno con grupos hidroxilo en el anillo inferior presenta unas isotermas muy distintas según el pH de la subfase usada.[56] Así a pH ácido o neutro se forman partículas de agregados como consecuencia de puentes de hidrógeno inter- y/o intra-moleculares mientras que con subfase básica la monocapa es uniforme debido a dos factores: la formación de puentes de hidrógeno entre los hidroxilos y las moléculas de agua de la subfase y las repulsiones electrostáticas entre los aniones fenólicos adyacentes. La menor agregación y el anclaje a la subfase dan lugar a monocapas más estables.

En la Figura 3.3 se pueden observar las isotermas π-A para los tres tipos de pHs. El cambio de estructura para la monocapa de calixareno en subfase básica se puede apreciar a través de: expansión de la isoterma, cambio en la forma de la isoterma y un área límite similar a la teórica para una molécula de calix[4]areno en orientación paralela.

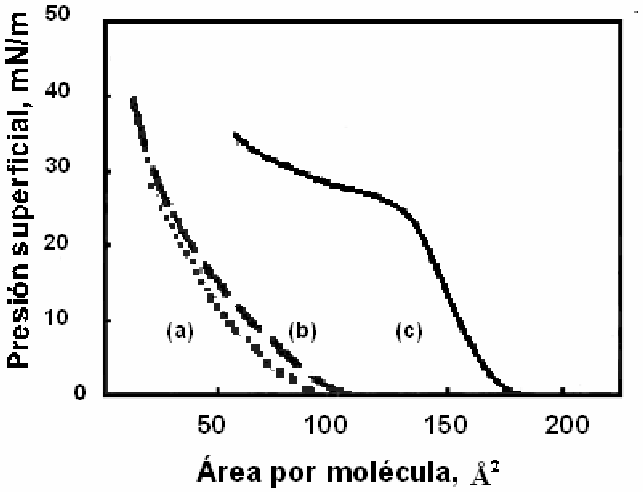

Figura 3.3: Isotermas π-A del *p-tert* butilcalix[4]areno en diferentes subfases: (a) medio ácido; (b) neutro; (c) básico.

Referencias

(1) Roberts, G. G. *Langmuir-Blodgett Films*; Plenum: New York, 1990.

(2) Ulman, A. *An Introduction to Ultrathin Organic Films from Langmuir-Blodgett to Self Assembly*; Academic Press: San Diego, 1991.

(3) Miyama, S.; Nalwa, H. S. *Organic Electroluminescent Materials and Devices*; Gordon and Breach: Amsterdam, 1997.

(4) Tang, C. W.; VanSlyke, S. A. *Appl. Phys. Lett.* **1987**, *51*, 913.

(5) Yang, Y. *MRS Bull.* **1997**, *22*, 31.

(6) Stapff, I. H.; Stümfplen, V.; Wendorff, J. H.; Spohn, D. B.; Möbius, D. *Liq. Cryst.* **1997**, *23*, 613.

(7) Gaines, G. L. J. *Insoluble Monolayers at Liquid-Gas Interfaces*; Wiley-Interscience: New York, 1966.

(8) Adamson, A. W. *Physical Chemistry of Surfaces*; Wiley-Interscience: New York, 1982.

(9) Ishii, T. *Thin Solid Films* **1989**, *178*, 47.

(10) Kuhn, H.; Möbius, D.; Bücher, H. In *Physical Methods of Chemistry*; John Wiley & Sons: New York, 1972; Vol. 1.

(11) Knobler, C. M. *Adv. Chem. Phys.* **1990**, *77*, 397.

(12) Hönig, D.; Overbeck, G. A.; Möbius, D. *Adv. Mater.* **1992**, *4*, 419.

(13) Hada, H.; Hanawa, R.; Haraguchi, A.; Jonezawa, Y. *J. Phys. Chem.* **1985**, *89*, 560.

(14) Cordroch, W.; Möbius, D. *Thin Solid Films* **1992**, *210/211*, 135.

(15) Ahuja, R. C.; Caruso, P.-L.; Möbius, D.; Wildburg, G.; Ringsdorf, H.; Philp, D.; Preece, J. A.; Stoddart, J. F. *Langmuir* **1993**, *9*, 1534.

(16) Martín, M. T.; Prieto, I.; Camacho, L.; Möbius, D. *Langmuir* **1996**, *12*, 6554.

(17) Grüniger, H.; Möbius, D.; Meyer, H. *J. Chem. Phys.* **1983**, *79*, 3701.

(18) Hönig, D.; Möbius, D. *J. Phys. Chem.* **1991**, *95*, 4590.

(19) Kaercher, T.; Hönig, D.; Möbius, D. *Orbit* **1995**, *14*, 17.

(20) Kjaer, K.; Als-Nielsen, J.; Helm, C. A.; Laxhubler, L. A.; Mohwald, H. *Phys. Rev. Lett.* **1987**, *58*, 2224.

(21) Dutta, P.; Peng, J. B.; Lin, B.; Ketterson, J. B.; Prakash, M.; Georgopoulos, P.; Ehrlich, S. *Phys. Rev. Lett.* **1987**, *58*, 2228.

(22) Jacquemain, D.; Leveiller, F.; Weinbach, S. P.; Lahav, M.; Leiserowitz, L.; Kjaer, K.; Als-Nielsen, J. *J. Am. Chem. Soc.* **1991**, *113*, 7684.

(23) Kaganer, V. M.; Mohwald, H.; Dutta, P. *Rev. Mod. Phys.* **1999**, *71*, 779.

(24) Als-Nielsen, J.; Mohwald, H. In *Handbook of Synchrotron Radiation*; Ebashi, S., Koch, M., Rubenstein, E., Eds.; Elsevier: Amsterdam, 1991.

(25) Kuhn, H.; Försterling, H. D. *Principles of Physical Chemistry*; John Wiley & Sons: New York, 1999.

(26) Pope, M.; Swenberg, C. E. *Electronic Processes in Organic Crystals and Polymers*; 2 ed.; Oxford Science Publications: New York, 1999.

(27) Czikkely, V.; Försterling, H. D.; Kuhn, H. *Chem. Phys. Lett.* **1970**, *6*, 207.

(28) McRae, E. G.; Kasha, M. *J. Phys. Chem.* **1958**, *28*, 721.

(29) McRae, E. G.; Kasha, M. *Physical Processes in Radiation Biology*; Academic Press: New York, 1964.

(30) Scheibe, G. *Angew. Chem.* **1936**, *49*, 567.

(31) Jelly, E. E. *Nature* **1936**, *138*, 1009.

(32) Czikkely, V.; Försterling, H. D.; Kuhn, H. *Chem. Phys. Lett.* **1970**, *6*, 11.

(33) Gutsche, C. D. D., B. No, K. Muthukrishnan, R. *J. Am. Chem. Soc.* **1981**, *103*, 3782.

(34) Gutsche, C. D. *Acc.Chem.Res.* **1983**, *16*, 161.

(35) Stewart, D. R. G., C.D. *J. Am. Chem. Soc.* **1999**, *121*, 4136.

(36) Gutsche, C. D. *Calixarenes* **1989**, *The Royal Society of Chemistry, Camdridge*.

(37) Yamato, T. K., K. Tsuzuki, H. *Can. J. Chem.* **2001**, *79*, 1422.

(38) McMurry, J. E. P., J.C. *Tetrahedron Lett.* **1991**, *32*, 5655.

(39) Gutsche, C. D. *Tetrahedron* **1983**, *39*, 409.

(40) Kanamathareddy, S. G., C.D. *J. Am. Chem. Soc.* **1993**, *115*, 6572.

(41) Otsuka, H. S., Y. Ikeda, A. Araki, K. Shinkai, S. *Tetrahedron* **1998**, *54*, 423.

(42) McKervey, M. A. O., M.Schulten, H.R. Vogt, W. Böhmer, V. *Angew. Chem. Int. Ed.* **1990**, *29*, 280.

(43) Beer, P. D. K., A.D. Slawin, A.M.Z. Williams, D.J. *J.Chem.Soc., Dalton Trans.* **1990**, 3675.

(44) Arimura, T. M., S. Teshima, O. Nagasaki, T. Shinkai, S. *Tetrahedron Lett.* **1991**, *32*, 5111.

(45) Böhmer, V. M., F. Zetta, L. *J.Org.Chem* **1987**, *52*, 3200.

(46) Munch, J. H. *Makromol. Chem.* **1977**, *178*, 69.

(47) Saenger, W. B., C. Hingerty, B. Brown, G.M. *Angew. Chem. Int. Ed.* **1983**, *22*, 883.

(48) Keller, S. W. S., G.M. Tobiason, F.L. *Polym. Mater. Sci. Eng.* **1987**, *57*, 906.

(49) Andreetti, G. D. U., R. Pochini, A. *J. Chem. Soc., Chem. Commun.* **1979**, 1005.

(50) Markowitz, M. A., Bielski, R. Regen, S.L. *Langmuir* **1989**, *5*, 276.

(51) Esker, A. R. Z., L-H. Olsen, C.E. No, K. Yu, H. *Langmuir* **1999**, *15*.

(52) Castillo, R.; Ramos, S.; Cruz, R.; Martinez, M.; Lara, F.; Ruiz-Garcia, J. *J. Phys. Chem.* **1996**, *100*, 709
713.

(53) Dei, L.; Lo Nostro, P.; Capuzzi, G.; Baglioni, P. *Langmuir* **1998**, *14*, 4143
4147.

(54) Tyson, J. C. M., J.L. Hughes, K.D. Collard, D.M. *Langmuir* **1997**, *13*, 2068.

(55) Merhi, G. M., M. Coleman, A.W. *Supramol. Chem.* **1995**, *5*, 173.

(56) Kim, J. K., Y. Lee, K. Kang, S. Koh, K. *Synthetic Metals* **2001**, *117*, 145.

CAPÍTULO 2

EXPERIMENTAL

2.1 TÉCNICAS DE FORMACIÓN Y CARACTERIZACIÓN DE MONOCAPAS EN LA INTERFASE AIRE-AGUA

2.1.1 Balanza de Langmuir

Los registros de isotermas presión superficial-área (π-A) y las curvas de estabilidad de área frente al tiempo, a presión superficial constante, constituyen el primer paso en la caracterización de una monocapa de Langmuir. Para la realización de las citadas experiencias se emplea la balanza de Langmuir. Este instrumento consta básicamente de los siguientes elementos: una cuba de material plástico, teflón, donde se aloja el líquido que constituye la subfase (normalmente agua ultrapura MilliQ o una disolución acuosa), y sobre el que se deposita la disolución que contiene el material que va a formar la película; una barrera móvil que separa la superficie de trabajo (donde se esparce la película) de la superficie limpia, y que es la encargada de comprimir la monocapa; y un sistema de medición de presión superficial. La velocidad de compresión utilizada en las diferentes isotermas oscila entre 0.05-0.1 nm^2/min·molécula.

El sistema de medida de presión superficial de las balanzas de Langmuir empleadas en esta Memoria fue del tipo Wilhemy[1]. El dispositivo experimental de este sistema está constituido por una lámina metálica, o de papel, que se encuentra parcialmente sumergida en la subfase y conectada, por el otro extremo, a una microbalanza electrónica de alta sensibilidad. De los tres tipos de fuerza a los que se encuentra sometida la lámina, peso, empuje y tensión superficial, sólo esta última varía por la presencia de la monocapa sobre la subfase respecto de la subfase limpia. Por tanto, la diferencia entre la fuerza medida antes y después de esparcir la monocapa es debida únicamente a la diferencia de tensión superficial, que es precisamente la presión superficial. En la Figura 1 se muestra un esquema de la balanza de Langmuir. En esta Memoria se han utilizado dos balanzas comerciales NIMA de tipo rectangular, modelos 611D y 601BAM, con una y dos barreras móviles respectivamente.

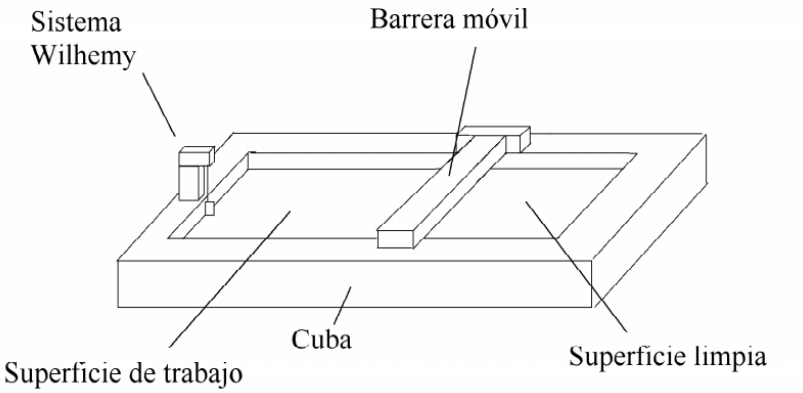

Figura 1: Esquema de una balanza de Langmuir

2.1.2 Espectroscopía de Reflexión

Las medidas de reflexión (ΔR) en la interfase aire-agua se han realizado en un equipo diseñado por *Nanofilm* (actualmente *Accurion*, www.accurion.com), modelo RefSpec[2]. La espectroscopía de reflexión es una técnica muy útil en el estudio de monocapas en la interfase aire-agua,[2-4] ya que registra la reflexión producida por las moléculas que se encuentran en dicha interfase y que contribuyen a resaltar su reflexión. La reflexión en la interfase aire-agua se mide como la diferencia de reflexión producida por la parte de la interfase cubierta con la monocapa respecto a la reflexión de la subfase limpia registrada antes de esparcir la monocapa.

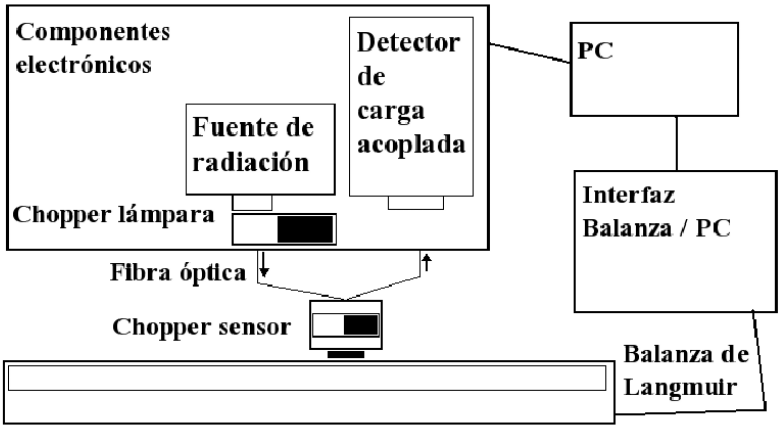

Figura 2: Esquema del reflectómetro RefSpec[2]

En la Figura 2 se puede ver un esquema de funcionamiento del espectrofotómetro de reflexión.[3-4] La fuente de luz consiste en dos lámparas, una de

deuterio y otra de tungsteno, ambas instaladas en un soporte de cerámica. La luz sale por una ventana de cristal de cuarzo, que la colima hacia la fibra óptica. Posteriormente esta radiación pasa por un monocromador instalado en el sensor. De ahí sale e incide en la muestra, esparcida sobre la interfase aire-agua. Este mismo sensor enfoca la luz reflejada hacia una fibra óptica, para que llegue al detector. Existen dos choppers que permiten alternar entre la radiación emitida por la lámpara y la reflejada por la muestra, ambos controlados electrónicamente. El chopper del sensor tiene su parte trasera cubierta por un espejo de forma que, además, sirve como referencia estática para las oscilaciones de la lámpara. En el fondo de la balanza se coloca una placa negra que actúa como trampa de luz para absorber los rayos transmitidos. De esta forma, la radiación reflejada entra al detector CCD, que envía la señal al ordenador donde se registra y procesa adecuadamente.

2.1.3 Microscopía de Ángulo Brewster (BAM)

Las imágenes de microscopía de ángulo Brewster han sido obtenidas en un sistema comercial I-Elli*2000* de *Nanofilm* (actualmente *Accurion*, www.accurion.com). El montaje experimental[5-6] del microscopio BAM, también representado en la Figura 3, se halla acoplado a una balanza de Langmuir donde se extiende la monocapa objeto de estudio.

El dispositivo se compone de un láser verde (Nd:YAG, 50 mW, 532nm) que produce un rayo de luz de 1.3 mm de diámetro, el cual atraviesa un polarizador, donde adquiere polarización *p*, e incide posteriormente sobre la interfase con $i = 53.15^{o}$, ángulo de Brewster para el agua. En este sistema, la intensidad de luz refractada es absorbida por una placa negra (trampa de luz) colocada en el fondo de la balanza, mientras que la reflejada pasa a través de un objetivo con distancia focal de 20 mm y llega a una cámara CCD de alta sensibilidad, que recoge la reflectividad debida a la presencia de la monocapa en la interfase. La cámara CCD es capaz de registrar en forma electrónica la intensidad y el punto de llegada de pequeñísimas cantidades de luz, que son convertidas a imágenes de mapa de bits (768 x 562 píxeles), para su representación y análisis a través de la aplicación informática que controla el equipo. El procesamiento de la imagen incluye la corrección geométrica de ésta, así como el uso de filtros para reducir interferencias y ruido. Asimismo, el brillo de la imagen es reescalado para mejorar el contraste.

La resolución lateral del sistema óptico en el plano de la superficie acuosa es de 2 µm. El microscopio está equipado con un analizador frente a la cámara que permite observar los posibles efectos ópticos de anisotropía en el interior de los dominios en que se organizan las moléculas que forman la película. De este modo, mediante la rotación del analizador respecto a la dirección de polarización p, luz incidente, se pueden observar diferencias en el contraste dentro de un mismo dominio, fenómeno indicativo de una diferente orientación molecular. Tanto el microscopio como la balanza están situados sobre una mesa antivibratoria *Halcyonics* (actualmente *Accurion*, www.accurion.com) MOD-2 S, dentro de una cámara limpia.

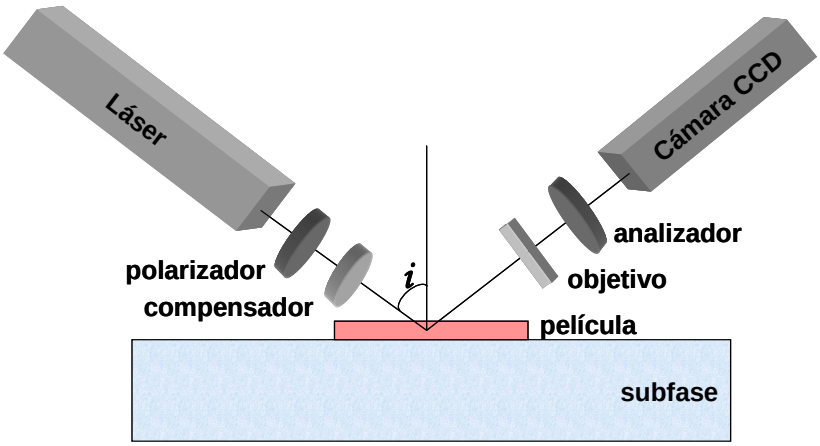

Figura 3: Esquema del Microscopio BAM

2.1.4 Difracción y reflectividad de rayos X

Las medidas de difracción de rayos X de incidencia rasante (GIXD) y las de reflectividad especular de rayos X (XRR) en la interfase aire-agua, fueron realizadas en la línea BW1 del HASYLAB (DESY, Hamburgo, Alemania). Las monocapas fueron preparadas en una balanza de Langmuir con una barrera móvil, termostatizada a 21ºC, equipada con un dispositivo Wilhelmy como sensor de presión, y situada en un contenedor cerrado herméticamente y lleno de helio. En la línea BW1, un haz de rayos X sincrotrón monocromático (λ=1.304Å), se ajusta para que incida en la interfase helio-agua con un ángulo rasante de $\alpha_i=0.85\alpha_c$ ($\alpha_c\approx0.13º$) e ilumine aproximadamente 2x50 mm^2 de superficie. Durante las medidas, la balanza se mueve lateralmente para evitar que la potente radiación X provoque daños en la muestra. Un detector sensible a la

posición lineal (PSD, MYTHEN, Suiza) es girado en torno a la balanza para escanear los valores de la componente en el plano Q_{xy} del vector de dispersión. Los canales verticales del mismo detector sirven para medir la componente fuera del plano Q_z del vector de dispersión entre 0 y 0.8Å. La intensidad de la radiación detectada se corrige en función de la polarización, el área efectiva y el factor de Lorentz. Los datos obtenidos para Q_{xy} y Q_z se ajustan por mínimos cuadrados a curvas modelo, Lorentzianas y Gaussianas respectivamente. La intensidad de radiación difractada en dirección normal a la interfase es integrada en el rango del pico de difracción Q_{xy} para calcular la correspondiente "barra de Bragg".

Para las medidas de reflectividad especular se usó el mismo dispositivo que para las medidas de difracción, pero siendo los ángulos incidente y reflejado iguales y variando en el rango $0.5\ \alpha_c < \alpha_i\ (\alpha_f) < 30\ \alpha_c$, y usando un detector de centelleo de NaI para medir la luz reflectada en el plano del rayo incidente, en función del vector de dispersión fuera del plano Q_z. El perfil de densidad electrónica fue obtenido de los datos de reflectividad, usando el método de aproximación de Pedersen y Hamley con el software StochFit.[7]

2.2 MATERIALES, REACTIVOS Y TRATAMIENTO DE DATOS

Todos los materiales y reactivos usados en las experiencias de la presente Memoria, fueron adquiridos en las diferentes firmas comerciales que se citan en cada capítulo. En todas las experiencias el agua es ultrapura, producida en una unidad Millipore Milli-Q tras un pretratamiento en un sistema Millipore de ósmosis inversa ($18 M\Omega \cdot cm^{-1}$).

Los datos adquiridos de forma digital se han tratado con los programas SigmaPlot,[8] Microcal Origin[9] y MathCad,[10] que a su vez se han utilizado en la realización de las figuras que se presentan en esta Memoria, y en el caso de MathCad, también en algunas de las simulaciones matemáticas. Asimismo, se ha procedido al tratamiento de imágenes con el paquete Corel, que incluye entre otros Corel Photo Paint o Corel Draw,[11] empleándose además este último en la preparación de los esquemas gráficos que aparecen en los distintos Capítulos.

Referencias

(1) Fromherz, P. *Rev. Sci. Instrum.* **1975**, *46*, 1380.

(2) Kuhn, H.; Möbius, D.; Bücher, H. In *Physical Methods of Chemistry*; John Wiley & Sons: New York, 1972; Vol. 1, p 656.

(3) Grüniger, H.; Möbius, D.; Meyer, H. *J. Chem. Phys.* **1983**, *79*, 3701.

(4) Orrit, M.; Möbius, D.; Lehmann, U.; Meyer, H. *J. Chem. Phys.* **1986**, *85*, 4966.

(5) Hönig, D.; Möbius, D. *J. Phys. Chem.* **1991**, *95*, 4590.

(6) Hönig, D.; Overbeck, G. A.; Möbius, D. *Adv. Mater.* **1992**, *4*, 419.

(7) Danauskas, S. M.; Li, D.; Meron, M.; Lin, B.; Lee, K. Y. C. *J. Appl. Cryst.* **2008**, *41*, 1187.

(8) SigmaPlot; 7 ed.; Jandel Scientific: Corte Madera, CA 94925, USA, 2001.

(9) MicrocalOrigin; 6.1 ed.; Microcal Software: Northampton, 1995.

(10) MathCad.; 11 ed.; Mathsoft Inc.: 2003.

(11) CorelDraw; 9 ed.; Corel Corporation: Ottawa, Ontario, Canada, 1995.

CAPÍTULO 3

ESTUDIO DEL COLAPSO DE MONOCAPAS FORMADAS POR LÍPIDO Y PORFIRINA

3.1 Reversible collapse of insoluble monolayers: New insights on the influence of the anisotropic line tension of the domain

In this paper we study the collapse of a mixed insoluble monolayer formed by a cationic matrix, dioctadecyl-dimethylammonium bromide (DOMA), and a tetra-anionic porphyrin, tetrakis(4-sulfonatophenyl)porphyrin (TSPP), in a molar ratio TSPP/DOMA = 1:4. During the collapse of this system, we visualized the formation of circular domains consisting exclusively of trilayer, althogh the domains coalescence was not observed. The coexistence of trilayer and monolayer at the final step of the collapse cannot be interpreted exclusively in terms of a thermodynamic phase equilibrium, intervening as an additional factor the anisotropic line tension of the domain. A high line tension implies a high resistance to the domain deformation, and the anisotropy of the line tension the lack of coalescence between these domains, which has been experimentally observed by BAM for us. Under these circumstances, the domains of material collapsed could enclose monolayer regions where the local surface pressure drops and stopping the collapse process.

The collapse of the TSPP/DOMA system is reversible, i.e. the return of the 3D material to the monolayer fits into a simple kinetics according to the nucleation-growth-collision theory. As for the collapse, the reverse process is also affected by the line tension of the domains. This paper relates the high line tension and the anisotropy line tension of a given domains with the reversible nature of the collapse process.

Paper published in *J. Phys. Chem. B,* ***113*** (2009) 13249-13256

3.1.1 Introduction

Monolayer collapse is of capital importance from a nanotechnological point of view, as it is a physical process in which molecules are self-assembled into supramolecular, 3D structures.[1] Furthermore, monolayer collapse plays a fundamental role in biophysical system, such as in the pulmonary surfactants.[2] A rationale comprehension of the monolayer collapse, as well as a quantitative model, is highly desirable. A Langmuir monolayer can show two- to three-dimensional phase transitions under overcompression, where modified structures are formed in the direction perpendicular to the water surface. Such a transition occurs at a particular surface pressure called the collapse pressure, and the newly formed state is called the collapse state.[3] In the absence of other phenomena, e.g., soluble aggregates, desorption or evaporation, the monolayer insoluble collapse could be described quantitatively through the decrease in the surface area at constant surface pressure.[4,5]

Although a few systems have been described which seem to collapse towards a bilayer,[6-9] for classical amphiphilic molecules, the first step in the collapse is the trilayer formation, but the process could progress towards the multilayer formation. However, some experimental systems have been described where the collapses seem to stop at the trilayer.[10-18] The understanding of the collapse mechanisms for these simple systems is essential to control their possible applications for creating supramolecular architectures by means of the Langmuir-Blodgett technique.

Two different mechanisms have been proposed by which a trilayer can grow from the monolayer of insoluble molecules: (I) the folding of the monolayer, and (II) the direct trilayer growth at the domain edge.[12,13,17,19] In the first case, the bilayer must flow (sliding) over the monolayer. In the second one the domain could be formed both by the bilayer, as the previous case, or by the trilayer, which adopts a more rigid structure than the monolayer.

As demonstrated previously, the mixed monolayers formed by dioctadecyl-dimethylammonium bromide (DOMA) and tetrakis(4-sulfonatophenyl)porphyrin (TSPP) in a molar ratio 4:1, experiment a collapse at high surface pressure.[14] Thus, when an area of $A \approx 0.75$ nm^2/DOMA molecule is reached upon compression, and keeping the surface pressure constant ($\pi_c \geq 33$ mN/m), several small circular bright domains can be observed by BAM. Those bright domains grow spontaneously filling almost all of the field of view in a few minutes. During this phenomenon, the film area

decreases from $A \approx 0.75$ nm^2 at $t = 0$ s to ~ 0.3 nm^2 at $t \rightarrow \infty$. The experimental results obtained confirm that the collapse corresponds to a phase transition between a monolayer and a trilayer with well-defined structure.[14] Also, from ellipsometry measurement we have demonstrated that the bright domains correspond to the trilayer structure.[14] Moreover, the collapse is reversible, i.e. when the surface pressure decreases below its collapse value the monolayer is regenerated from the trilayer.

However, in the final step of the collapse process ($A \approx 0.3$ nm^2), the interface is not completely covered by the trilayer, as one would expect for a classical phase transition. We observed that this phenomenon is due to the absence of coalescence between domains which originates monolayer enclosed regions where the local surface pressure drops below the collapse surface pressure. We studied this phenomenon and its influence on the experimental *A-t* relaxation curves is analyzed for the collapse and the reverse process, as well.

3.1.2 Experimental

Materials: Dioctadecyldimethylammonium bromide (DOMA) was purchased from Sigma Chemical Co. and used as received. Tetrakis (4-sulfonatophenyl) porphyrin (TSPP) was supplied by Fluka and used without purification. A mixture of dichloromethane, methanol and water, ratio 15:9:2 (v/v/v), was used as spreading solvent for solving both components. The pure solvents were obtained without further purification from Panreac (Spain) and Baker Chemicals (Germany). The water for the subphase and for the mixture spreading solvent was prepared with a Millipore Mill-Q unit, pretreated by a Millipore Reverse Osmosis system (>18 MΩ×cm^{-1}).

Preparation of the mixed monolayers at the air–water interface: Mixed monolayers of TSPP/DOMA, in a molar ratio of 1:4, were prepared by cospreading (the mixed solution of the two components) onto a pure water subphase at 21 ºC on a Nima Langmuir trough provided with a Wilhelmy type dynamometric system using a plate of filter paper for good wettability. After cospreading of the mixed solution on the water surface, 15 min were left for evaporation of the solvent and the monolayers were compressed at a speed of ~ 0.1 nm^2 min^{-1} molecule^{-1}.

Brewster angle microscopy: Images via Brewster angle microscopy (BAM) were obtained with a I-Elli2000 apparatus (supplied by Nanofilm Technologies,

Göttingen, Germany) using a Nd:YAG diode laser, which can be recorded with a lateral resolution of 2 µm. The image processing procedure included a geometrical correction of the image, as well as a filtering operation to reduce interference fringes and noise. Furthermore, the brightness of each image was scaled to improve contrast. The microscope and the film balance were located on a table with vibration isolation (anti-vibration system MOD-2 S, Halcyonics, Göttingen, Germany) in a large class 100 clean room.

3.1.3 Results and Discussion

3.1.3.1 Time-Area curves at constant collapse Surface Pressure. Monolayers of TSPP/DOMA, in a molar ratio of 1:4, were formed at the air-water interface as was described previously.[14] Figure 3.1 (inset) shows a cyclic π–A isotherm where the area, A, is expressed per DOMA molecule. The most noticeable phenomenon observed is the monolayer collapse as the mixed film is compressed at $A < 0.75$ nm^2.

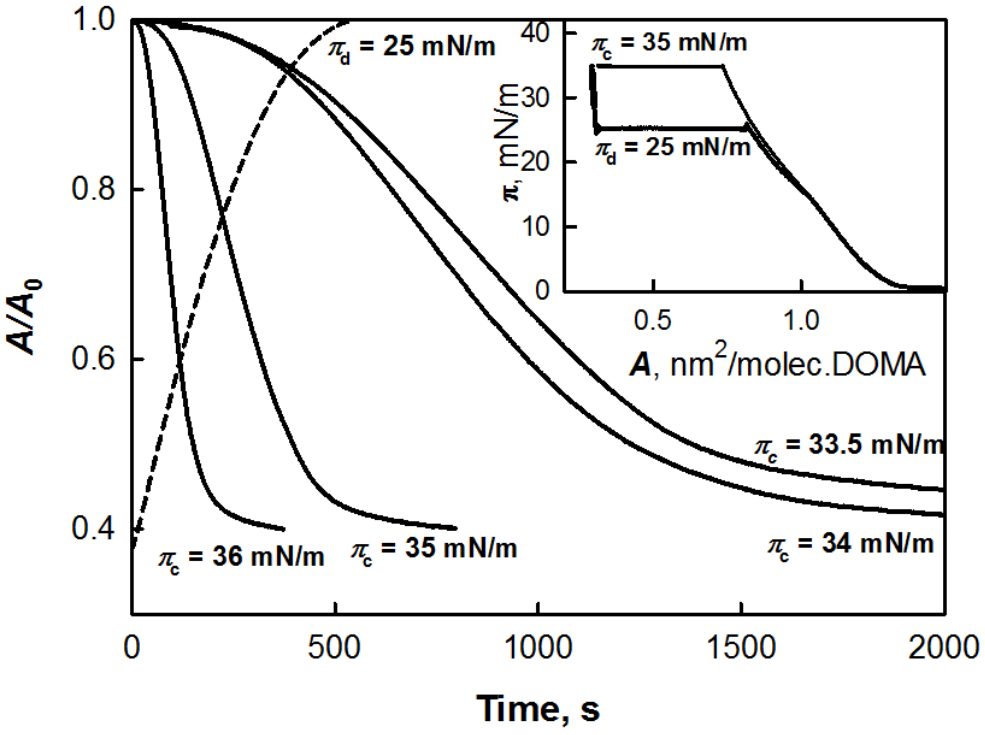

Figure 3.1: Black solid line; time–area curves (A/A_0, *vs t*, where $A_0 = A_{Max}$) for four different π_c values, ranges from 33.5 – 36 mN/m. Black dashed line; time–area curve (A/A_∞, *vs t*, where $A_\infty = A_{Max}$) for π_d = 25 mN/m. Inset; Cyclic surface pressure-area isotherms of TSPP/DOMA = 1:4 (solid line) at the air-water interface, under compression from 0 to 35 mN/m, evolution with time at π_c = 35 mN/m, decompression to 25 mN/m, evolution with time at π_d = 25 mN/m, and decompression from 25 to 0 mN/m.

The kinetics of the monolayer collapse has been studied by applying a constant surface pressure. First, the film was compressed to a fixed surface pressure (π_0 = 32 mN/m) below the collapse surface pressure. After compression, time for stabilization of the film was allowed. A complete stabilization of the film was considered when the molecular area did not change with time. After stabilization, the surface pressure was increased to a new constant value ($\pi_c \geq 33.5$ mN/m). A spontaneous area reduction of the monolayer was registered (*A*–*t* curves). Figure 3.1 shows the area variation as A/A_0, *vs* time (solid lines), where A_0 is the surface area when π_c is reached (t = 0 s) and A is the surface area at a given time t. Four different values of collapse pressure (π_c) have been used, ranging from 33.5 – 36 mN/m. For the collapse process, the initial area is the maximum area $A_{Max} = A_0$ (0.75 nm^2/DOMA molecule).

As can be seen, the relaxation process occurs in a shorter time as π_c increases. For any value of $\pi_c \leq 36$ mN/m, at an infinite time, $A/A_0 \approx 0.4$. For $\pi_c > 38$ mN/m the spontaneous monolayer area reduction occurs in very few seconds, so the collapse starts during the initial compression process ($\pi_0 \rightarrow \pi_c$).

The A/A_0–t curves show an interesting behaviour. Measuring the time (τ) for which a fixed A/A_0 value is reached for the different π_c values, for example for A/A_0 = 0.8, the following values are obtained, τ = 706, 632, 206 and 75 s, for π_c = 33.5, 34, 35 and 36 mN/m, respectively. The plot A/A_0 *vs* t/τ, shows that all the curves are superimposed, which is indicative that the collapse mechanism is conserved independently from the applied π_c.

To investigate the stability of the monolayers formed at the air-water interface, successive compression-expansion cycles of the films were carried out. In all the cases small or null hysteresis was observed (see supporting information).

3.1.3.2 Direct visualization of film morphology by BAM. Brewster angle microscopy (BAM) offers the possibility of visualizing the film morphology directly. Mixed TSPP/DOMA =1:4 monolayer at the air–water interface was studied by BAM (Figure 3.2). Monolayer (2D) to trilayer (3D) transformation was observed, as reported for supersaturated monolayers.[20] BAM images were recorded simultaneously in the *A* *vs* *t* measurement. At the initial time (t = 0), under a constant surface pressure π_c, the monolayer appears as an homogeneous film (images not shown). After a short time,

small bright domains with circular forms appear on the film. The bright domains are surrounded by a darker area. The domains grow spontaneously along their radial direction. For a constant A/A_0 value, the number of domains increases, and the average size of the domain decreases when the applied π_c increase. In any case, for $\pi_c \leq 38$ mN/m at infinite time, the bright domains fill an area fraction of the observed surface of ~ 0.8-0.85, while the dark regions fill an area fraction of the observed surface of ~ 0.2–0.15, approximately.

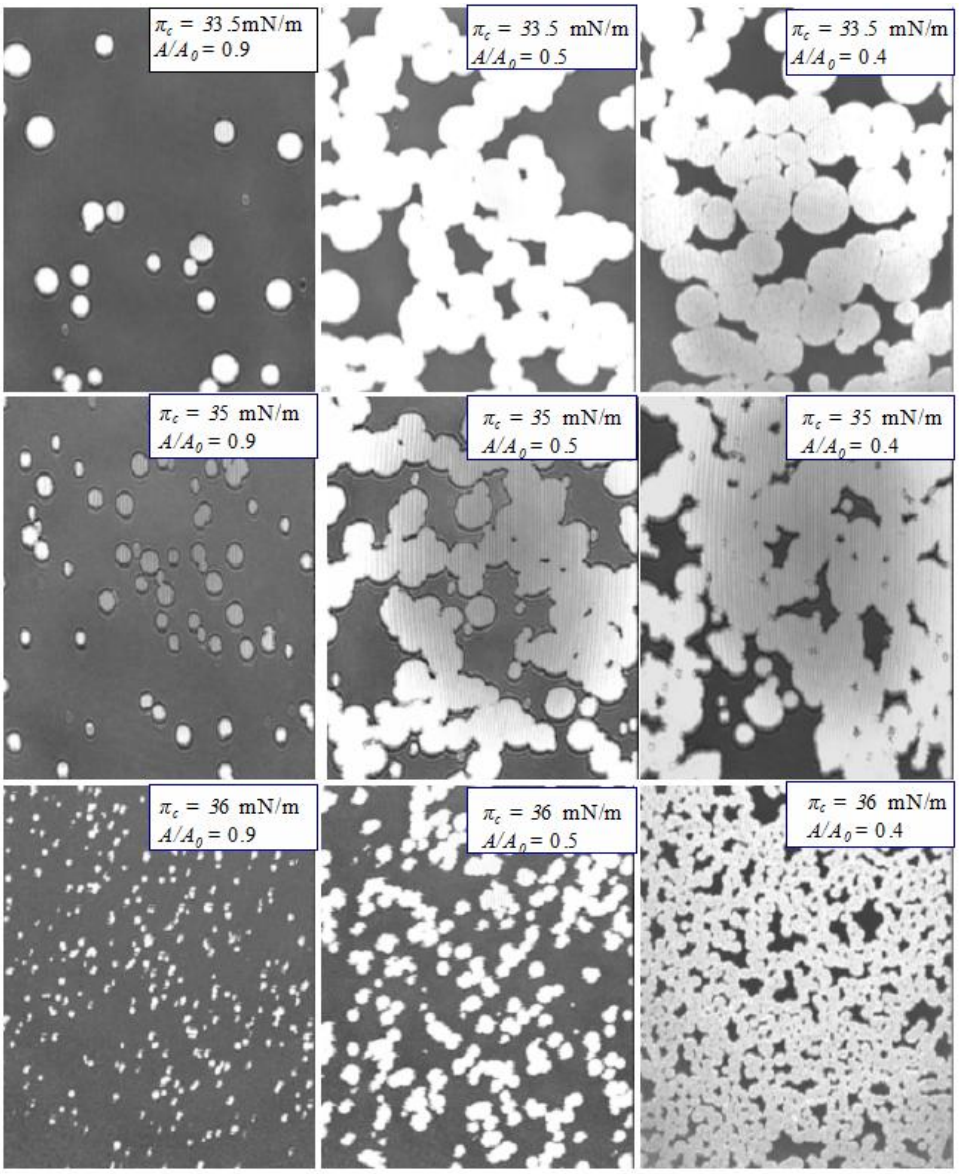

Figure 3.2: The growing of the domains observed by BAM for π_c = 33.5, 35 and 36 mN/m, at three A/A_0 values, for the mixed TSPP/DOMA monolayer. Image size: 400 μm width.

During the decompression process the domains disappear completely, as is described below. If a second compression of the film is realized for the same collapse surface pressure, the BAM images show domain with similar form and size that those observed for the first compression step (see supporting information), indicating the reversible character of the collapse.

3.1.3.3 Failure in the application of the classical nucleation-growth-collision (NGC) theory.

The decreasing of the area, A/A_0, *vs* time, *t*, as displayed in Figure 3.1, is a consequence of the transference of monolayer material from monolayer (2D) to trilayer (3D). This behavior could be analyzed by means of the classical NGC theory. This theory was introduced for insoluble monolayers by Vollhardy and Retter.[5,21-23] The NGC theory assumes the formation and subsequent growth of 3D centers, considering the overlap of the growing nuclei in the subsequent stages of the process. According to the model, the variation of area with time is expressed as:

$$\frac{A\ t}{A_0} = \frac{A_\infty}{A_0} + \frac{A_0 - A_\infty}{A_0} \exp\left[-k\ \ t - t_{ind}\ ^{n}\right] \qquad (1)$$

where A_0 and A_∞ denote molecular area values at initial and infinite time, respectively, *k* is a constant, t_{ind} is an induction time, and *n* an integer or semi-integer number, which depends on the nucleation mechanism.

Although it is possible to obtain a good fit between equation (1) and our experimental data, these numerical fits should be interpreted with caution, as shown below. Thus, the experimental data (A/A_0 *vs t*) were fitted to equation (1) by using A_∞/A_0 = 0.4, and t_{ind}, *k* and *n* as unknown parameters. Figure 3.3A shows the experimental data for π_c = 35 mN/m (grey dotted line) and the predictions of equation 1 (solid line). The obtained values for the parameters were; t_{ind} = -13 s, *k* = 0.015 s^{-n} and *n* = 2.51. As can be seen, there is a general good agreement between experimental data and theoretical predictions. The negative induction time could be related with the elapsed time from the stabilization pressure (π_0 = 32 mN/m), to the surface pressure π_c. The value $n \approx 2.5$ was obtained for all the π_c values analyzed. This *n* value corresponds to hemisphere clusters and progressive nucleation.[5]

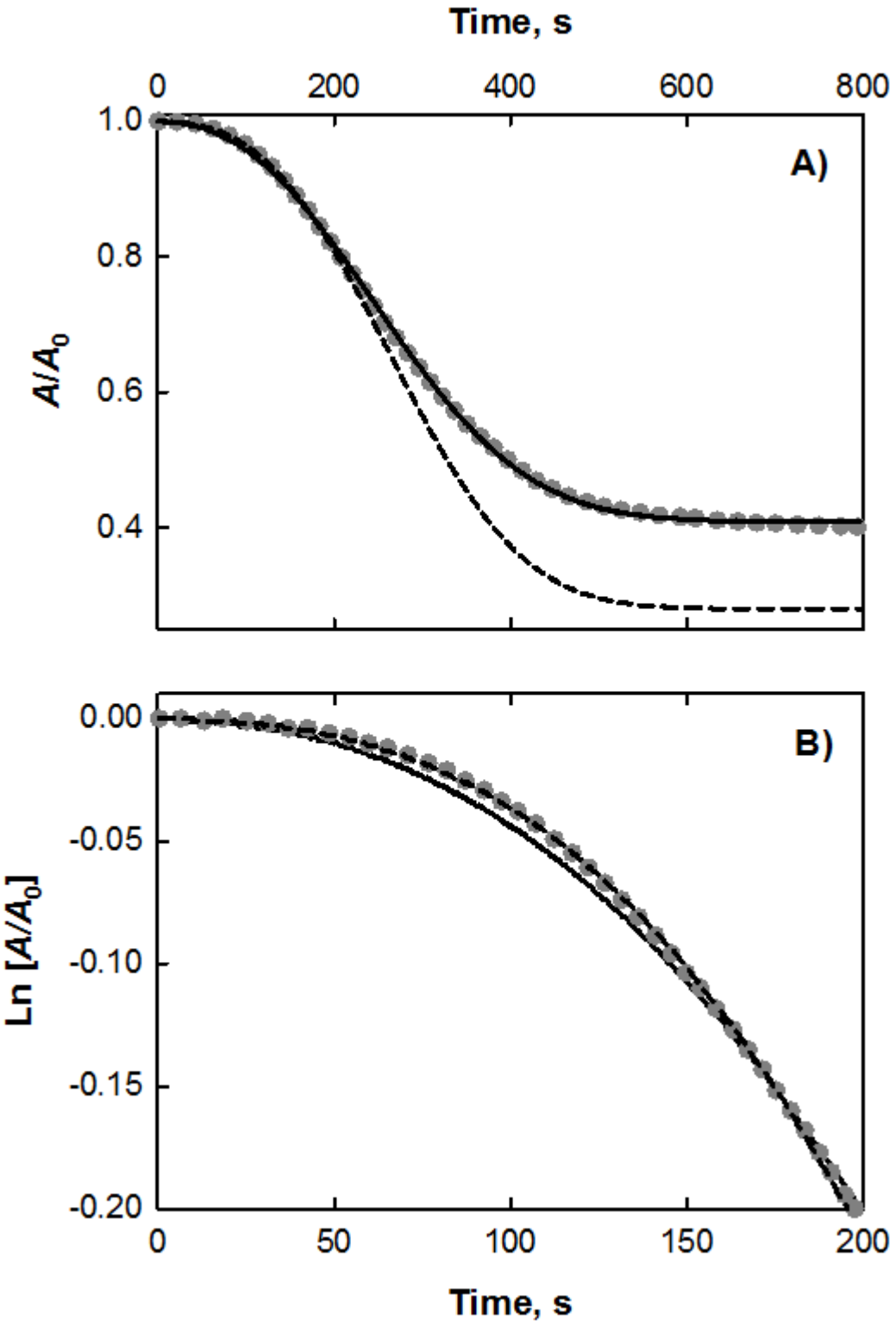

Figure 3.3: A) Grey dotted line; experimental A/A_0 *vs t* data for π_c = 35 mN/m. Solid line; predictions of equation (1) for A_∞/A_0 = 0.4, t_{ind} = -13 s, k = 0.015 s^{-n} and n = 2.51. Dashed line; predictions of equation 1 for A_∞/A_0 = 0.28, t_{ind} = -12 s, k = 7.296×10^{-3} s^{-n} and n = 2.94. B) Plot of Ln(A/A_0) *vs t* for the same conditions that A).

However, there are two facts that make us think that the good agreement between experimental data and theoretical predictions is circumstantial. First, the nuclei observed in BAM images are cylinders that grow along their edges. Therefore, values of $n = 2$ (instantaneous) or $n = 3$ (progressive) are expected.[5] Second, the NGC theory is based on the collision and overlapping of the growing domain, i.e. the NGC theory assumes that in the final step of the monolayer collapse, the whole surface is covered by the 3D domains. In this context, the Avrami expression for the overlapping of growing centres is used to obtain the equation (1).[5,24-26] However, as displayed in Figure 3.2, in the final step of the monolayer collapse there are regions covered by domains, but there are also regions where the collapse does not take place and the monolayer still persists.

In Figure 3.3B plot of Ln(A/A_0) *vs t* for the experimental data (π_c = 35 mN/m, grey dotted line), as well for the predictions of equation 1 (solid line, for t_{ind} = -13 s, k = 0.015 s^{-n} and n = 2.51) are shown. The plot is zoomed into the region of the initial times. As can be seen, for these time values there is a slight deviation between the experimental data and theoretical predictions.

An eye on the circular domains formed by π_c = 33.5 nM/m and A/A_0 = 0.4 (see Figure 3.2), which correspond to an infinity time relaxation, permits us to observe that the domains are in collision, but they neither coalesce nor are deformed. This behavior must be related with the rigid structure of the domains.

3.1.3.4 Excluded surface regions: monolayer existence beyond the collapse. The BAM images shown by A/A_0 = 0.4 in Figure 3.2 represents the final step of the collapse. Surprisingly, for a $\pi_c \geq 33.5$ nM/m, there are regions in which the monolayer persists in the final step of the collapse. Neither the growth of the nuclei nor the appearances of new nuclei are observed hereafter. However, the surface pressure remains constant. From a thermodynamic point of view, new nuclei should be formed in the monolayer regions and the nuclei should continue to grow.

The proposed explanation for this phenomenon is that in regions where the monolayer persists, ("excluded surface" regions for the collapse), the local surface pressure drops below a certain threshold value. This drop in the local surface pressure inhibits the nucleation and the nuclei growth processes. It should be highlighted that this concept implies the existence of regions inside the monolayer under a local surface pressure below collapse surface pressure $\pi < \pi_c$, for a macroscopic situation of a

monolayer under a global $\pi > \pi_c$. The origin of these excluded surface regions is explained as follows. When the available area decreases to values close to the collapse final area, some monolayer regions are enclosed by domain collision: excluded surface regions (see black regions in Figure 3.2 for A/A_0 = 0.4, and Scheme 1). The excluded surface regions are isolated from each other. In this way, the collision between collapsed domains might form an interconnected rigid network which sustains extra pressure, while the actual pressure in the monolayer remains lower than the collapse pressure. The nuclei growth from the molecules located inside the excluded surface regions is not possible, given that the promotion of molecules from the monolayer to the domain should be accompanied by a reduction in the enclosed area (approximately a reduction of two thirds for the trilayer formation). Then, the promotion of molecules from the monolayer to the trilayer is prohibited due to the rigid network of the domains. Initially the domains grow, but the inside area does not decrease in a proportional way. As a consequence, the surface pressure drops inside the enclosed regions. The enclosed regions are transformed into excluded surface regions for the nucleation and growth (see Scheme 1).

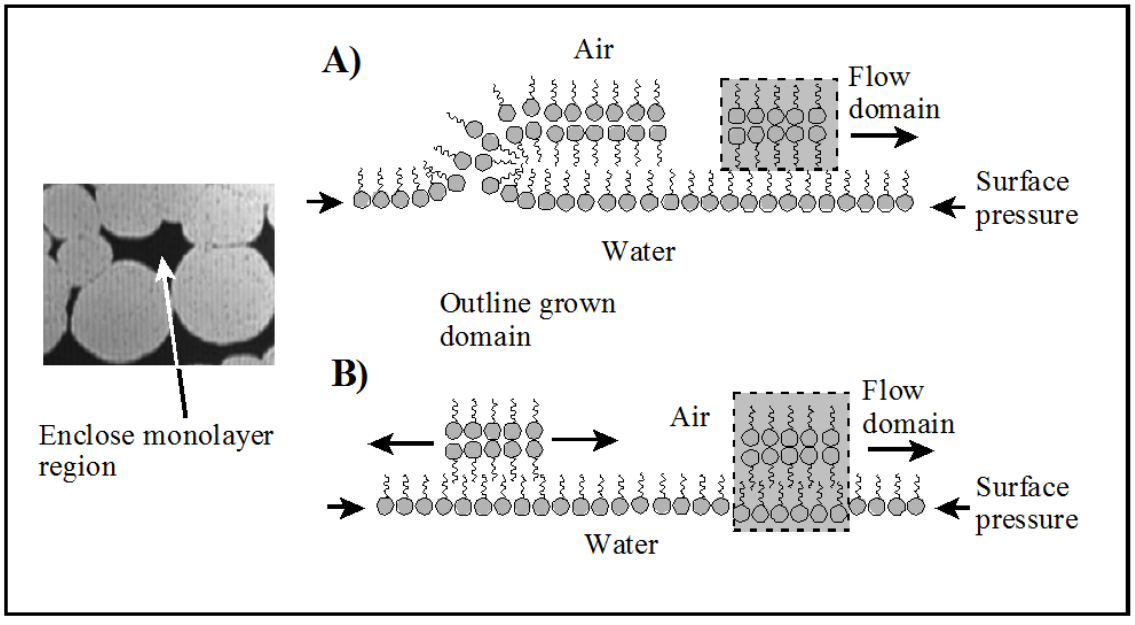

Scheme 1: Left; Zoom of the BAM image corresponding to an enclosed monolayer region (black region). A) Illustration of a 3D domain consisting of bilayer floating over the monolayer. B) Illustration of a 3D domain consisting of a trilayer immersed in the monolayer.

Vollhardt and Retter define the critical surface pressure required for the formation of the 3D nuclei (π_{crit}), and the minimum surface pressure at which the nuclei continue to grow (π_e),[27] being $\pi_e < \pi_{crit}$. The drop of the surface pressure inside the enclosed region must be below π_e.

Excluded surface regions are not expected to be found in monolayers that collapse via folding. In the case of monolayer folding, the surface pressure is applied continuously on the whole monolayer. The drop of the surface pressure in the monolayer would not be possible if the 3D domain consisted of bilayer floating over the monolayer (see Scheme 1A). There is an important conclusion from the previous explanation; in our system the 3D domain must be immersed in the monolayer, in contact with the aqueous subphase, and formed by the trilayer (Scheme 1B). In this way, discontinuity arises, and distinct values of local surface pressure are allowed.

3.1.3.5 Absence of domain coalescence and/or deformation: physical insights.

Under the perspective of the traditional monolayer collapse via trilayer formation, total domain coalescence is assumed to occur. However, as BAM images show, for the DOMA/TSPP mixed monolayer, there is no coalescence and/or deformation of domains, even for an infinite time. This result seems surprising, as it contradicts the classical assumption of total film covering by the trilayer upon collapse. The physical explanation for this phenomenon implies the consideration of an additional parameter: the line tension of the domains. The circular form of the domains indicates the minimization of its perimeter and consequently its energy; therefore the domains must be fluid, and should coalesce under surface pressure,[28] against what is observed experimentally. Meunier et al.[29,30] suggested that an anisotropic contribution to the line tension is essential to stabilize the domains in determinate situations. Anisotropy in the line tension does not permit the domains to be fused, whereas isotropic line tension allows the domains to be fused while touching each other.[31] The anisotropic line tension could be originated by the different tilt of the lipid at the boundary of the domains, which remember the behavior of the liquid crystal.[32]

Therefore, the monolayer collapse is obviously a change of phase, although this cannot be interpreted exclusively in terms of a thermodynamic equilibrium, intervening, as an additional factor the anisotropic line tension of the domains. A high line tension

implies a high resistance to the domain deformation, and the anisotropy of the line tension involves the lack of coalescence between these domains.

In the spirit of obtaining new insights on the line tension influence, a relaxation experiment was performed. In this experiment, a constant surface pressure of π_c = 33.5 mN/m was applied, allowing the film to reach the final step of the collapse process (see A/A_0 = 0.398 in Figure 3.4). After that, the surface pressure was increased in steps of 1 mN/m, allowing an extra time after each surface pressure increment for the stabilization of the film. Figure 3.4 shows recorded BAM images obtained from this experiment. As can be seen, with the increasing of surface pressure, A/A_0 decreases lightly, for example, for π = 40 mN/m, the area decreases to A/A_0 = 0.346, but neither the coalescence nor the deformation domain are evident. At π = 40 mN/m, the appearance of bright streaks at the contact line between domains is observed. The bright streaks may be related with the superposition of neighboring domains. Moreover, the appearance of new nuclei in the black regions of the film cannot be observed.

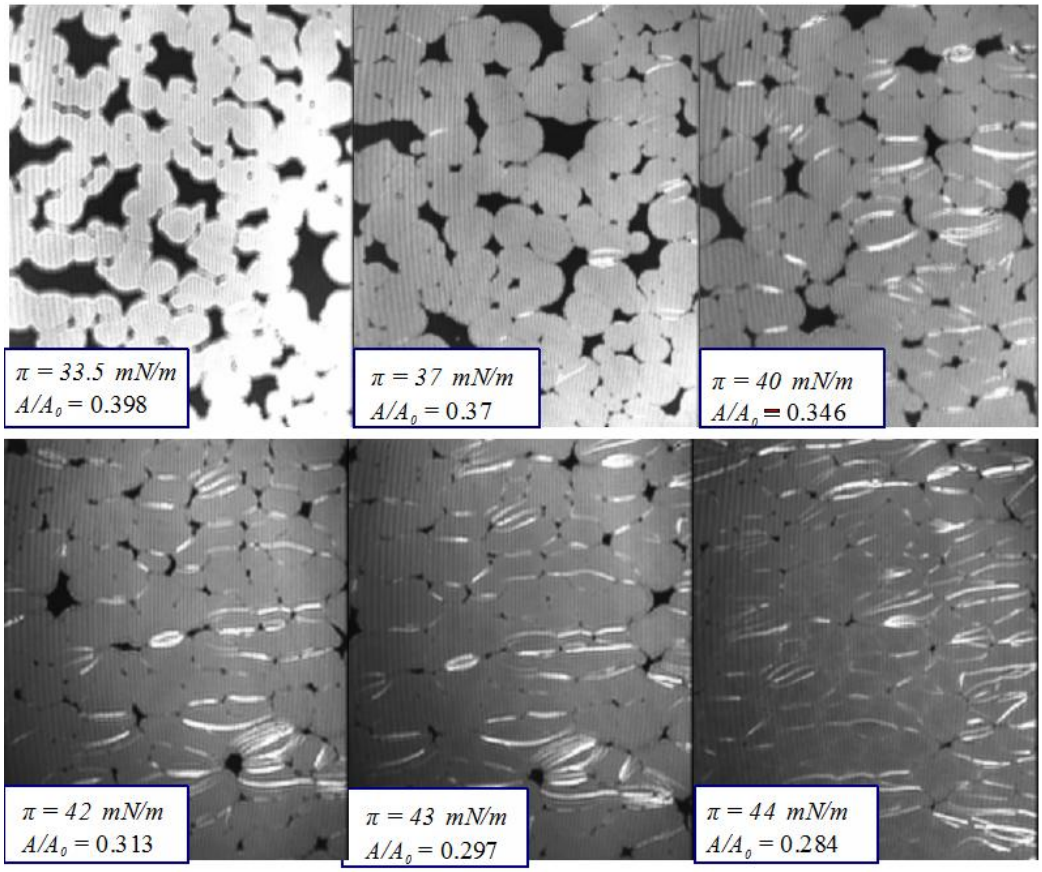

Figure 3.4: BAM images obtained after a relaxation experiment at π_c = 33.5 mN/m. After the final step of the collapse process, the surface pressure was increased in steps of 1 mN/m, waiting after each pressure

increase to the stabilization of the film. Only BAM images obtained at 37, 40, 42, 43 and 44 mN/m are shown.

The application of a surface pressure above 40 mN/m results in domain deformation, but no domain coalescence was observed. For this surface pressure the domains are forced to grow with a non circular geometry. At 44 mN/m, the excluded surface regions (black monolayers region) disappear almost completely being the fraction of dark area less than 1%. In this experiment the surface pressure π_e is reached inside the excluded surface regions, but the π_{crit} is not reached.

3.1.3.6 Revisiting NGC theory: accounting for partial collapse.

For the NGC theory, A_∞ is defined as the area when the interface is completely covered with domains with homogeneous structures. The fulfillment of equation (1) implies that neither the rate of nucleation nor the rate of growth of nuclei change over the whole relaxation process, and that the growing nuclei coalesce as a final stage of the process. This assumption leads to a complete collapse of the monolayer at infinite time: the whole monolayer is converted into a trilayer structure. However, if the collapse is not completed, the experimental area A_∞ represents an apparent value without physical meaning as referring to the model represented by equation (1).

The absence of coalescence between domains prevents us to apply the equation (1), at least for the full relaxation period observed in Figures 1-3. During the first stages of the nucleation, when there is no collision between nuclei, the A_∞ value must correspond to a hypothetical situation where the entire surface should be coated by the domains. Therefore, it is not correct to use the apparent value $A_\infty/A_0 \approx 0.4$, as was used previously for the numerical fit shown in Figure 3.3 (solid line). This fact was considered previously by Rugonyi et all,[17] who assumed that for a trilayer transformation A_∞ must be 1/3 of the A_0.

If θ is defined as the surface fraction occupied by the domains, as observed by BAM. Then, A/A_0 is expressed as:

$$\frac{A}{A_0} = 1-\theta + \frac{A_\infty}{A_0}\theta \qquad (2)$$

Thus, when $A/A_0 \approx 0.4$ (final step of monolayer collapse at a constant π_c, Figure 3.2), the surface fraction recovered by the domains is $\theta \approx 0.8 – 0.85$, therefore from the

equation (2), $A_\infty/A_0 \approx 0.25$ -0.29, i.e. as $A_0 \approx 0.75$ nm^2, then $A_\infty \approx 0.19$ - 0.22 nm^2. This calculated A_∞/A_0 value agrees with the experimental value obtained at π = 44 mN/m, from Figure 3.4 where the total surface is almost covering with trilayer. The experimentally obtained area reduction is slightly lower than that expected for a trilayer formation (from $A_0 \approx 0.75$ nm^2, to $A_\infty \approx 0.25$ nm^2). This difference is ascribed to an arrangement somewhat more compact of the molecules in the domain than in the monolayer.

Fitting the experimental A/A_0 *vs t* data to equation (1), for $A/A_0 > 0.8$ (implying $\theta < 0.28$) an improved agreement between calculated and experimental data is obtained, as shown in Figure 3.3B. Using A_∞/A_0 = 0.28, t_{ind}, k and n can be calculated. Figure 3.3B show the experimental data for π_c = 35 mN/m (grey dotted line), and the predictions of equation 1 (dashed line). The values of the parameters obtained were as follows: t_{ind} = -12 s, $k = 7.296\times10^{-3}$ s^{-n} and n = 2.94. As can be seen from Figure 3.3B [Ln(A/A_0) *vs t*], for the region of lower times, there is an excellent agreement between experimental data and theoretical predictions. The value $n \approx 3$ was obtained by using values of A_∞/A_0 ranging between 0.25-0.29. Furthermore, $n \approx 3$ is obtained for all the analyzed π_c values. This n value implies that the rate of the radial growth of a nucleus, considered to be a circular disk, does not vary with time and that the nucleation is progressive (small rate constant).[5]

Therefore, the application of the NGC theory should be realized with caution. Equation (1) is applicable, in the full range of time, only when the coalescence of the domain takes place.

3.1.3.7 The kinetics of the return of the material collapsed to the monolayer: Trilayer to monolayer transition.

The collapse of a DOMA/TSPP mixed monolayer is a reversible process.[14] After the monolayer collapse reach its final point, the molecular area maintains a constant value. Film structure, as formed by both monolayer and trilayer regions, may be decompressed by using a new constant surface pressure value, π_d. The surface pressure π_d should be slightly below π_c. For a $\pi_d \geq 30$ mN/m, the film area does not increase, indicating that the monolayer recovering from the trilayer does not occur. However, for $\pi_d < 30$ mN/m an expansion of the film was observed. Figure 3.1 shows the A/A_{Max} vs t expansion curve for π_d = 25 mN/m (dashed line).

Vollhardt and Retter demonstrated, by using a two-step surface pressure experiment, that at the equilibrium surface pressure π_e the preformed nuclei cease to grow.[27] The decompression experiment described here is also a two-step surface pressure experiment. The difference is that for our case, $\pi_d < \pi_e$ and, therefore the nuclei must decrease for an ideal case. From a formal perspective, the NGC theory (equation 1) can be applied to a phase-change 3D → 2D. The main consideration is that the monolayer and trilayer exchange their roles. That is, the monolayer is the final state. The initial state is a mixed monolayer and trilayer state. Values of A_0 and A_∞ are also exchanged. The maximum area in this expansion process coincides with the area at the end of the experiment, $A_\infty = A_{max}$.

Figure 3.5 shows BAM images obtained during the expansion process. As can be seen, the bright domains (trilayer) decrease in size, while retaining their circular form, approximately. Eventually, bright domains disappear completely. In none of the expansion experiments the occurrence of holes, i.e. dark regions due to the monolayer formation, inside the domain was observed.

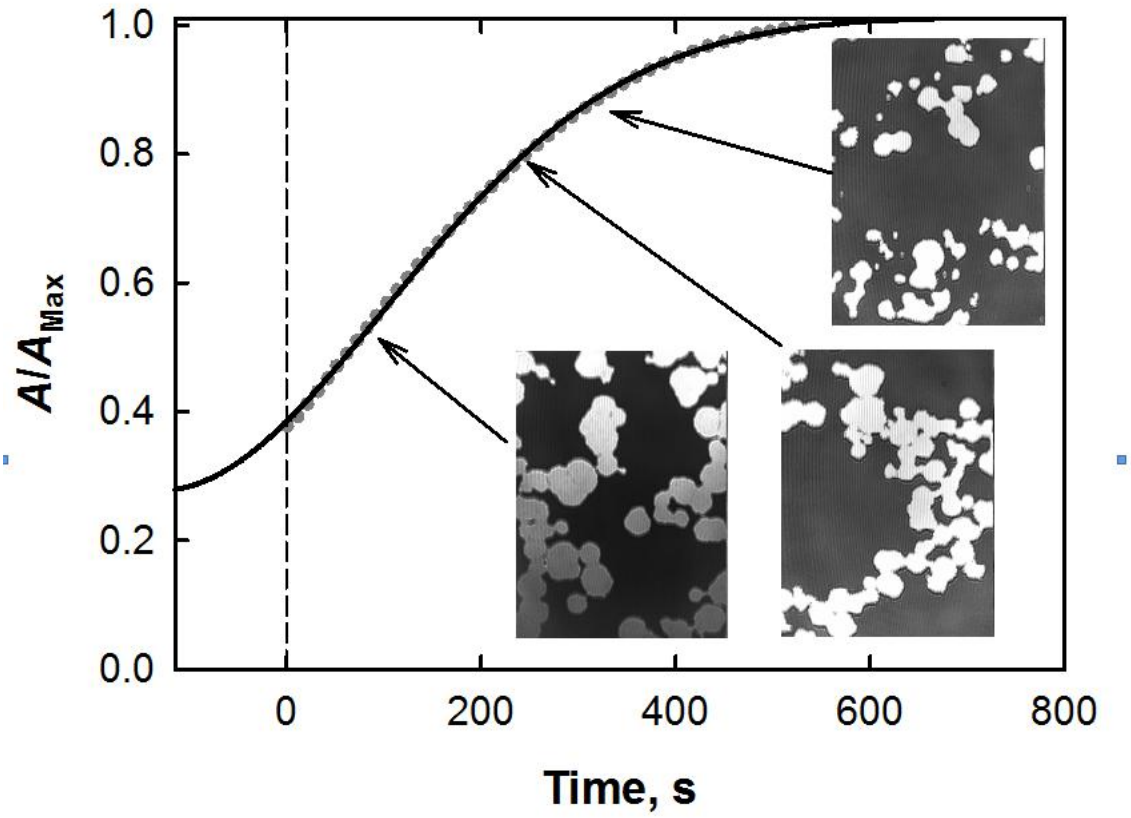

Figure 3.5: Grey dotted line; experimental A/A_∞, *vs t*, (where $A_\infty = A_{Max}$) for π_d = 25 mN/m. Solid line; predictions of equation 3 for ; A_0/A_∞ = 0.26, t_{ind} = -130.3 s, $k = 1.19\times10^{-5}$ s^{-n} and n = 1.95. Also some BAM images obtained during the expansion process are shown.

For the film expansion process, A_0 is the theoretical area for a film completely formed as a trilayer. This A_0 area is not experimentally accessible. In this case A_0 corresponds to the area A_∞ for the compression process. For the monolayer expansion process, A_∞ is the area for the monolayer, as completely recovered, at π = 25 mN/m. This A_∞ value can be measured experimentally ($A_\infty \approx 0.82$ nm^2, see inset in Figure 3.1). In this way, equation (1) can be easily transformed for decompression into:

$$\frac{A\ t}{A_\infty} = 1 + \frac{A_0 - A_\infty}{A_\infty} \exp\left[-k\ \ t - t_{\text{ind}}\ ^{n} \right] \qquad (3)$$

The fit of the experimental data (A/A_∞ *vs* t) to equation (3) by using A_0/A_∞, t_{ind}, k and n as unknown parameters is shown in Figure 3.5 as a solid line. The obtained parameters were as follows; $A_0/A_\infty = 0.26$, $t_{\text{ind}} = -130.3$ s, $k = 1.19\times10^{-5}$ s^{-n} and $n = 1.95$. It should be noted that in this case, there is coalescence between monolayer regions. Therefore, all the set of experimental data could be used for the numerical fit of equation (3). The possibility of using experimental data recorded during all the expansion time is a fundamental difference with the collapse process, where only the initial data may be used, due to the lack of coalescence between domains.

As $A_\infty \approx 0.82$ nm^2, and $A_0/A_\infty = 0.26$, $A_0 \approx 0.21$ nm^2 is obtained. A_0 corresponds to the theoretical area when the film is completely formed as a trilayer, a value coincident with the previously obtained. The negative value of t_{ind}, accounts for the time required for an interface fully covered by the trilayer to reach the starting point of the expansion experiment (t = 0, see Figure 3.5). The values of $n \approx 2$ were obtained for all the experiments performed. This value is consistent with an instantaneous nucleation with cylindrical edge growth. It is noticeable that for the collapse process the nucleation was progressive, whereas for the inverse process the nucleation was instantaneous.

The conceptual difficulty involved in defining the critical size of the nucleus, and the nucleation rate for the inverse process of the collapse is worthy of special note. One may assume that after the 3D film is formed and π_d is applied, some holes (monolayer) are formed. These holes in the 3D phase will be unstable unless they reach a given critical size. The number of such critically sized holes will be the equivalent to the number of nuclei for the condensation, being positive the hole growth rate. With these considerations, Equation (3) is acceptable and the collapse reversible.

In spite of the formal equivalence between nucleation and its inverse process, theoretical difficulties arise in the case of an interface completely covered by a trilayer or a more compact film. For a case of a trilayer under expansion, the monolayer should be formed from the holes appearing inside the trilayer domain. However, the creation of these holes inside the domain trilayer is highly improbable, since the area occupied by a molecule in the monolayer is three times larger than the molecular area occupied in the trilayer, approximately. A 3D rigid domain with high line tension cannot be expanded due to hole formation without a fracture of the whole crystalline lattice: the energy cost to cause such a fracture may be very high. The irreversibility of many collapse processes could be caused by this phenomenon. The return from an interface completely covered by collapsed material with high line tension in the monolayer state is only possible at the barrier, at the perimeter of the Langmuir trough, or through the film fractures. For these cases, the collapse will be irreversible.

For our case, the absence of holes inside the domains in the expansion process (see Figure 3.5), is an indication of the absence of the creation of holes. Therefore, it is assumed that all holes were created instantaneously at the beginning of the expansion process (negative time regions in Figure 3.5). This fact gives an explanation to why the nucleation process for the 3D $\rightarrow$ 2D transition is instantaneous. In fact, the holes (monolayer) already exist since the domains do not coalesce during the collapse (exclude regions). One consequence of the above reasoning is that the collapse is reversible for our system, and therefore the relaxation process follows the model of equation (3), because of the absence of domain coalescence during the collapse. A general conclusion may be drawn from this study: the collapse of condensed phases can be reversible only if the domains do not coalesce previously, at least for domains with high line tension.

3.1.4 Conclusions

The reversible collapse of a mixed monolayer DOMA:TSPP in a molar ratio 4:1 has been described thanks to BAM images and theoretical modeling. The collapse mechanism occurs via trilayer formation. Trilayer regions appear as bright domains with circular forms. Along the collapse process, the bright domains increase their size, but neither coalesces nor are deformed with compression. Moreover, in the final step of the

collapse there are regions in which the monolayer persists. These monolayer regions are enclosed by the surrounding trilayer domains and isolated from each other.

The presence of the monolayer in the final step of the collapse has been explained in terms of the drop of the surface pressure inside the enclosed regions. The collision between collapsed domains might form an interconnected rigid network which sustains extra pressure, while the actual pressure in the monolayer remains lower than the collapse pressure. The nuclei growth from the molecules located inside the monolayer enclosed regions are not possible, given that the promotion of molecules from the monolayer to the domain should be accompanied by a reduction in the enclose area (approximately a reduction of two thirds for the trilayer formation). Then, the promotion of molecules from the monolayer to the trilayer is prohibited due to the rigidity of the domains. Initially the domains grow, but the inside areas do not decrease in a proportional way. As a consequence, the surface pressure drops inside the enclosed regions. An important conclusion is that the domain must be formed by the trilayer (Scheme 2B) and not by bilayer floating over the monolayer.

In the case of high values of the collapse surface pressures, the domains can grow in a non-circular way, eventually filling the observed surfaces completely. Under this condition of high surface pressure, the domains never coalesce due to their anisotripic line tension. The monolayer collapse process is a phase change. However, the monolayer collapse cannot be interpreted exclusively in terms of thermodynamics equilibrium, intervening as an additional factor, the anisotropic line tension of the domains. A high line tension of a given domain implies a high resistance to deformation, and the anisotropy of the line tension the lack of coalescence between domains. Due to the lack of coalescence, the NGC theory (equation 1) cannot be applied to the DOAM:TSPP collapse, at least for the full relaxation time range. For short times and according to the NGC theoretical model, the collapse corresponds to a progressive nucleation with cylindrical edge growth.[5]

The collapse of the DOMA:TSPP system is reversible. Thus, the return kinetics from 3D → 2D phases could be analyzed from the NGC theory. For this expansion process, the monolayer and trilayer exchange roles. It is noticeable that for the collapse process the nucleation was progressive, whereas for the reverse process the nucleation was instantaneous. For a decompressing interface which is completely covered with trilayer at the initial time, or a more compact film, the monolayer should be formed

from the holes appearing inside the trilayer film. However, the creation of these holes inside the condensed films is highly improbable, since the area occupied by a molecule in the monolayer is three times greater than that which occupies the trilayer, approximately. A 3D rigid and homogeneous film cannot expand toward the monolayer through the hole formation without a fracture. The irreversibility of many collapse processes could be caused by this phenomenon. The return of the collapsed material toward the monolayer is only possible at the perimeter of the Langmuir trough, or through of fractures of the films.

However, for 3D structures formed by domains which do not completely cover the interface, the return to the monolayer takes place at the perimeter of the domains without hole formation inside the domains which is coherent with an instantaneous nucleation process. The reversible character of the collapse is probably due to the lack of coalescence between domains which favors the return of the molecules toward the monolayer.

3.1.5 Supporting Information

Surface Pressure – Area Isotherms, and BAM Images, for the second compression step.

The next figure shows a first π–A compression isotherm (black line), including the collapse process. After the stabilization at 33.5 mN/m, the film was expanded (see manuscript and Ref 14), just to reach an area of 1.8 nm^2/molecule DOMA. At this point, a second π–A compression isotherm was realized (red line). As can be seen the isotherms are almost coincident.

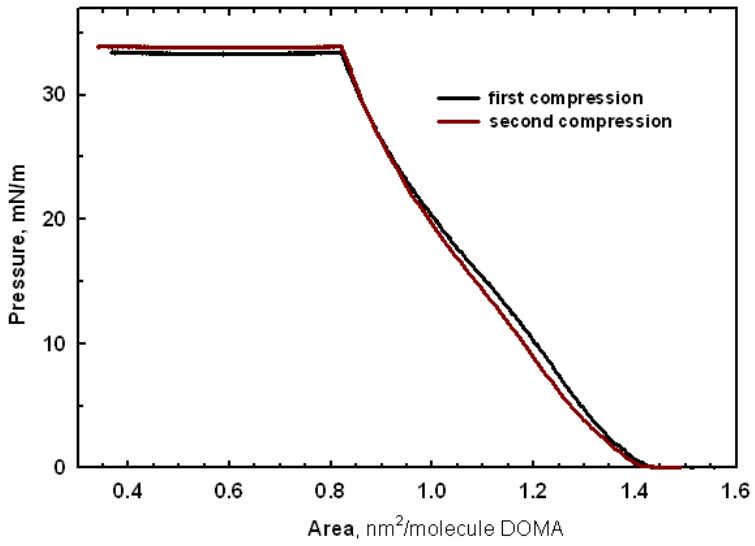

The next figure shows the BAM images along the first and second compression processes. The three images on top are obtained during the first cycle of compression, once the collapse has begun. For surface pressure below the collapse surface pressure, the monolayer appears as an homogeneous film. The BAM image at the left of the second row, correspond to the beginning of the second compression where we can observe the absence of domains. The next three BAM images at the bottom of the figure correspond to the second compression step, for the same surface areas that those during the first compression step, approximately. As can be seen the form and size of the domains are similar, which indicates the reversible character of the process.

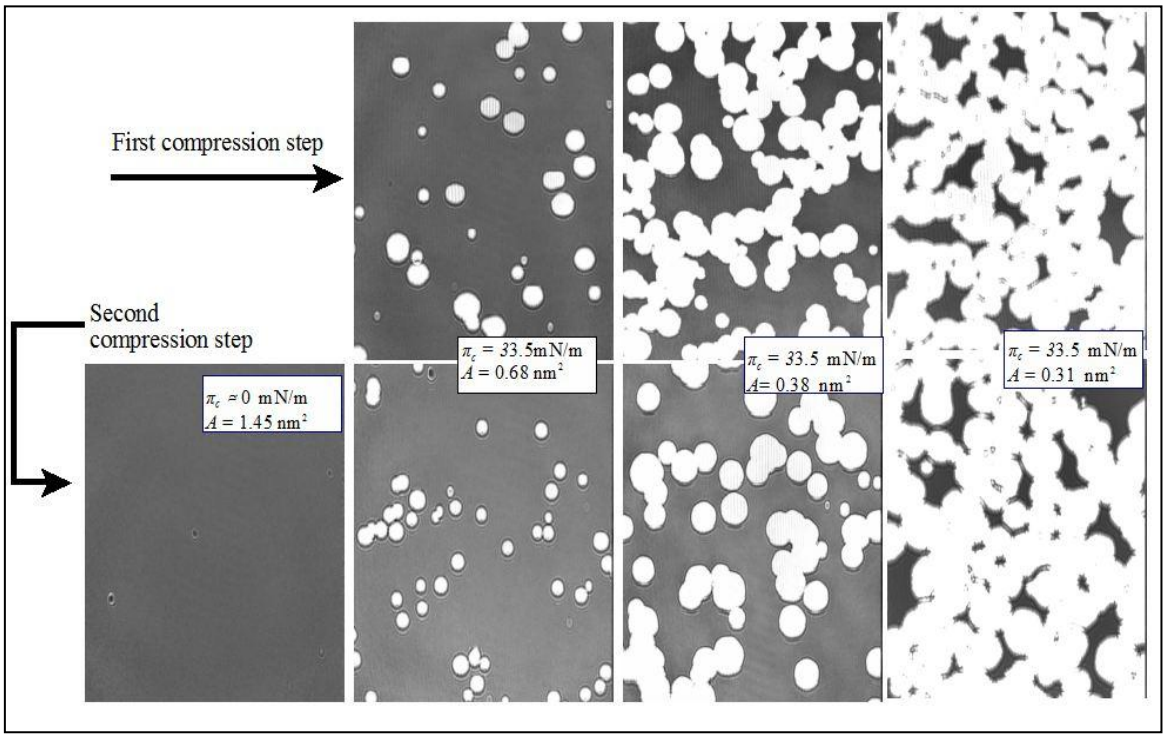

Acknowledgment. We thank the Spanish CICYT for financial support of this research in the framework of Project CTQ2007-64474/BQU (FEDER A), and also thank the Junta de Andalucía (Consejería de Innovación, Ciencia y Empresa) for special financial support P06-FQM-01698 and P08-FQM-4011.

References

(1) Rapaport, H.; Kuzmenko, I.; Belfeld, M.; Kjaer, K.; Als-Nielsen, J.; Popovitz-Biro, R.; Weissbuch, I.; Lahav, M.; Leiserowitz, L. *J. Phys. Chem. B* **2000**, *104*, 1399.

(2) Lee, K. Y. C. *Annu. Rev. Phys. Chem.* **2008**, *59*, 771.

(3) Gaines, G. L. *Insoluble Monolayers at Liquid-Gas Interface*; Interscience: New York, 1966.

(4) Smith, R. D.; Berg, J. C. *J. Colloid Interface Sci.* **1980**, *74*, 273.

(5) Vollhardt, D.; Retter, U. *J. Phys. Chem.* **1991**, *95*, 3723.

(6) Wagner, J.; Michel, T.; Nitsch, W. *Langmuir* **1996**, *12*, 2807.

(7) Chen, X.; Wiehle, S.; Weygand, M.; Brezesinski, G.; Klenz, U.; Galla, H. J.; Haufe, G.; Chi, L. *J. Phys. Chem. B* **2005**, *109*.

(8) Vaknin, D.; Bu, W.; Satija, S. K.; Travesset, A. *Langmuir* **2007**, *23*, 1888.

(9) Bu, W.; Vaknin, D. *Langmuir* **2008**, *24*, 441.

(10) Mul, M. N. G. D.; Mann, J. A. *Langmuir* **1994**, *10*, 2311.

(11) Salfer, R.; Michel, T.; Nitsch, W. *Colloid Surf. A: Physicochem. Eng. Aspects* **2002**, *210*, 253.

(12) Gourier, C.; Knobler, C. M.; Daillant, J.; Chatenay, D. *Langmuir* **2002**, *18*, 9434.

(13) Schief, W. R.; Antia, M.; Discher, B. M.; Hall, S. B.; Vogel, V. *Biophys. J.* **2003**, *84*, 3792.

(14) Perez-Morales, M.; Pedrosa, J. M.; Martin-Romero, M. T.; Möbius, D.; Camacho, L. *J. Phys. Chem. B* **2004**, *108*, 4457.

(15) Deng, J. J.; Viers, B. D.; Esker, A. R.; Anseth, J. W.; Fuller, G. G. *Langmuir* **2005**, *21*, 2375.

(16) Kundu, S.; Datta, S.; Hazra, S. *Langmuir* **2005**, *21*, 5894.

(17) Rugonyi, S.; Smith, E. C.; Hall, S. B. *Langmuir* **2005**, *21*, 7303.

(18) Kundu, S.; Datta, A.; Hazra, S. *Langmuir* **2008**, *24*, 9386.

(19) Nikomarov, E. S. *Langmuir* **1990**, *6*, 410.

(20) Siegel, S.; Honig, D.; Vollhardt, D.; Mobius, D. *J. Phys. Chem.* **1992**, *96*, 8157.

(21) Vollhardt, D. *Adv. Colloid Interface Sci.* **1993**, *47*, 1.

(22) Vollhardt, D.; Ziller, M.; Retter, U. *Langmuir* **1993**, *9*, 3208.

(23) Vollhardt, D. *Adv. Colloid Interface Sci.* **2006**, *123*, 173.

(24) Avrami, M. *J. Chem. Phys.* **1939**, *7*, 1103.

(25) Avrami, M. *J. Chem. Phys.* **1940**, *8*, 212.

(26) Avrami, M. *J. Chem. Phys.* **1941**, *9*, 177.

(27) Vollhardt, D.; Retter, U. *Langmuir* **1998**, *14*.

(28) Vollhardt, D. *Colloid Surf. A: Physicochem. Eng. Aspects* **1998**, *143*, 185.

(29) Hénon, S.; Meunier, J. *J. Chem. Phys.* **1993**, *98*.

(30) Riviére, S.; Meunier, J. *Phys. Rev. Lett.* **1995**, *74*.

(31) Mufazzal-Hossain, M.; Kato, T. *Langmuir* **2000**, *16*.

(32) Yamamoto, T.; Manaka, T.; Iwamoto, M. *Eur. Phys. J. E* **2009**, *29*, 1.

CAPÍTULO 4

ORGANIZACIÓN LATERAL EN MONOCAPAS FORMADAS POR LÍPIDOS Y COLORANTES

4.1 Control of the lateral organization in Langmuir monolayers via molecular aggregation of dyes

This paper shows that it is possible to construct well-defined 2D structures at the air-water interface in which the lateral organization is controlled by means of the preparation of mixed films, and selecting the components so that there are attractive interactions between them. The goal here is to establish the lateral connection between components through self-aggregation of the dye. This can be achieved by selecting a suitable balance between the sizes of the hydrophobic and polar groups. In such a way, the domain structure depends on the ability of the tilt dye to fill the available area.

Thus, the molecular organization and the domain morphology of mixed films containing dimyristoyl-phosphatidic acid (DMPA) and the hemicyanine dye, 4-[4-dimethylamino)styryl]-1-docosylpyridinium bromide (SP) have been studied by using Grazing Incidence X-ray Diffraction (GIXD), Brewster angle microscopy (BAM) and reflection spectroscopy at the air–water interface. For this mixed system, the formation of circular domains with bright horizontal regions and dark vertical regions was observed. Furthermore, depending on the temperature, it is observed as branches grow from circular domains, whose brightness depends on the growth direction. Thus, BAM images allow us to observe some branches that, as their growth direction changes, their brightness also changes simultaneously. The GIXD experiment permits us to relate the circular domains with an orthorhombic phase and the branches grown from the circles with an Overbeck phase. In both cases, the formed structures are induced by the hemicyanine aggregation. Circular BAM domain textures have been simulated by using the Fresnel equations for biaxial anisotropic materials.

Paper published in *J. Phys. Chem. C*, **114** (2010) 16685-16695

4.1.1 Introduction

The development of methods to build well-ordered assemblies of molecules into larger structures is a current objective of the supramolecular chemistry.[1,2] In this sense, the air–water interface is an ideal model for these purposes, as it is easy to prepare in a pure state and also because the surface coverage can be smoothly adjusted by using the Langmuir trough technique.[3] However, Langmuir monolayers are interesting not only in a fundamental way but also as a means to build ordered system on mesoscopic length scales.[4] The domains observed in Langmuir monolayers at high surface pressures indicate large structures formation. At the nanoscopic scale, the physical properties of these domains are determined by the relations between chemical composition, structure, and organization of these materials.[5] However, at the mesoscopic scale the domain shape is controlled by the competition between the dipolar energy of the domain and the line tension energy.[6] Thus, the repulsive dipolar interaction of the molecules within a domain favors a large boundary-to-area ratio, by which the electrostatic energy is reduced.[7] In this case, the domain morphology does not entirely correspond to the molecular lattice structure.[8]

To design well-defined structures in which the lateral organization is controlled, we need somehow to compensate the repulsion energy between dipoles. One method to compensate this repulsion energy is to form monolayers containing different components with attractive interactions between them. Thus, Vollhardt et al. studied melamine-type monolayers, where the amphiphilic molecules are connected by hydrogen bonds through nonsurface-active species as barbituric acid.[2] This type of bonding leads to the formation of large domains with long-range orientation of the molecules. Another method to compensate the repulsion energy between dipoles and used recently by us,[8] is the preparation of mixed monolayers of an anionic phospholipid (DMPA) and a water-soluble cationic dye (methylene blue, MB), which is retained at the interface by electrostatic interactions, establishing lateral connections through self-aggregation of the dye.

This paper attempts to show that the method used in the DMPA:MB system can be applied in a general manner to other dyes that show self-aggregation, under the condition of a suitable balance between the sizes of the hydrophobic and polar groups. Thus, if a_c is the interfacial area occupied by the hydrophobic group when alkyl chains are fully extended, and a_0 is the minimum interfacial area occupied by the head group,

dyes to be selected should obey $a_c \geq a_0$. In this way, the domain structure depends on the ability of the dye to fill the available area excess (a_c - a_0).

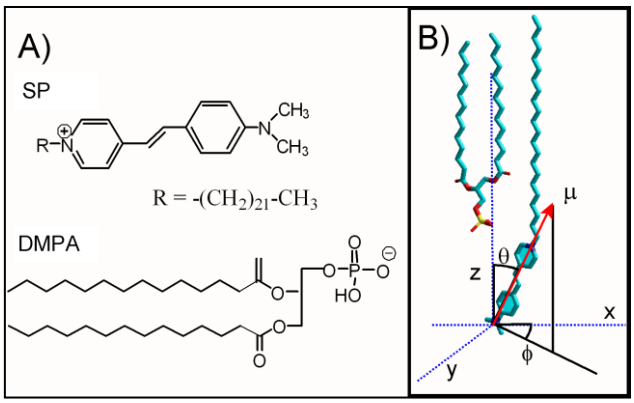

Scheme 1: A) Molecular structures of hemicyanine, SP, and dimyristoyl-phosphatidic acid, DMPA. B) Graphical definition of the transition dipolar moment, μ, the polar tilt angle, θ, and the azimuthal angle, ϕ, of the SP molecules in presence of the DMPA molecule (the interface plane coincides with *x*-*y* plane).

To verify the above approach, mixed films containing dimyristoyl-phosphatidic acid (DMPA), and an amphiphilic hemicyanine dye (SP) in a molar ratio 1:1, have been studied. It is known as the hemicyanine group suffers H-aggregation at the air-water interface,[9-15] and therefore it is a suitable compound for the study indicated. The behaviour of this mixed monolayer has been studied by using reflection spectroscopy,[16-19] Brewster angle microscopy (BAM),[20-25] as well as Grazing Incidence X-ray Diffraction (GIXD).[5,26-30] BAM technique has revealed an exciting large variety of morphological textures, also designated as condensed phase domains. These domains can exhibit a striking inner anisotropy and form subdomains of different brightness which have been attributed to regions of different molecular orientation.[24,25,31-35] Specifically for the SP:DMPA = 1:1 system, we observed the formation of circular domains with bright horizontal regions and dark vertical regions. Furthermore, depending on the temperature, it is observed as branches grow from circular domains, whose brightness depends on the growth direction. Thus, BAM images allow us to see some branches that changing their growth direction, their brightness changes simultaneously. In our system, the SP molecules absorb at 532 nm (wavelength of the laser used in BAM), being the SP absorption the origin of the appearance of the domain textures. The experimental circular domains textures have been simulated in the basis of the Fresnel equations for biaxial anisotropic materials on isotropic substrates. This

simulation permits us to obtain information about the rearrangement of the dye polar group in the domains. Furthermore, additional information on the rearrangement of the alkyl chain has been obtained from GIXD

4.1.2 Experimental

Materials. Hemicyanine dye, 4-[4-Dimethylamino)styryl]-1-docosylpyridinium bromide (SP) and dimyristoyl-phosphatidic acid (DMPA) were purchased from Sigma-Aldrich and used as received. Their molecular structures are depicted in Scheme 1. A mixture of chloroform:methanol, ratio 3:1 (v/v), was used as spreading solvent for solving both components. The pure solvents were obtained without purification from Aldrich (Germany). Ultrapure water, produced by a Millipore Milli-Q unit, pre-treated by a Millipore reverse osmosis system (> 18.2 MΩ cm), was used as a subphase. The subphase temperature was 21ºC with pH 5.7.

Methods. Two different models of Nima troughs (Nima Technology, Coventry, England) were used in this work, both provided with a Wilhelmy type dynamometric system using a strip of filter paper: a NIMA 611D with one moving barrier for the measurement of the reflection spectra, and a NIMA 601, equipped with two symmetrical barriers to record BAM images. The monolayers were compressed at a speed of ~ 0.1nm nm^2 min^{-1} $molecule^{-1}$.

UV–visible reflection spectra at normal incidence as the difference in reflectivity (ΔR) of the dye film-covered water surface and the bare surface[36] were obtained with a Nanofilm Surface Analysis Spectrometer (Ref $SPEC^2$, supplied by Accurion GmbH, Göttingen, Germany).

Images of the film morphology were obtained by Brewster angle microscopy (BAM) with a I-Elli2000 (Accurion GmbH) using a Nd:YAG diode laser with wavelength 532 nm and 50mW, which can be recorded with a lateral resolution of 2 μm. The image processing procedure included a geometrical correction of the image, as well as a filtering operation to reduce interference fringes and noise. The microscope and the film balance were located on a table with vibration isolation (antivibration system MOD-2 S, Accurion, Göttingen, Germany) in a large class 100 clean room.

Grazing Incidence X-ray Diffraction measurements of the monolayer were performed at 21°C at the BW1 beamline, HASYLAB, DESY (Hamburg, Germany). A

Langmuir film balance equipped with a single movable barrier and a Wilhelmy plate for monitoring the lateral pressure was placed in a hermetically closed container filled with helium. At BW1, a monochromatic synchrotron X-ray beam (λ=1.304 Å) was adjusted to strike the helium/water interface at a grazing incidence angle α_i=0.85α_c (α_c=0.13°) and illuminated roughly 2x50 mm^2 of the surface. During the measurements, the trough was laterally moved to avoid any sample damage by the strong X-ray beam. A linear position-sensitive detector (PSD, MYTHEN, Switzerland) was rotated to scan the in-plane Q_{xy} component values of the scattering vector. The vertical channels of the PSD measured the out-of-plane Q_z component of the scattering vector between 0 and 0.8 Å^{-1}. The diffraction data consisted of Bragg peaks at diagnostic Q_{xy} values. The accumulated position-resolved counts were corrected for polarization, effective area, and Lorentz factor. Model peaks taken as Lorentzian in the in-plane direction and as Gaussian in the out-of-plane direction were least-square fitted to the measured intensities. The diffracted intensity normal to the interface was integrated over the Q_{xy} window of the diffraction peak to calculate the corresponding Bragg rod. The thickness of the monolayer was estimated from the FWHM of the Bragg rod using ~0.9(2π)/FWHM(Q_z). Experimental details are described in the literature.[5,26-30]

4.1.3 Results and Discussion

4.1.3.1. Surface Pressure-Area Isotherms and Brewster Angle Microscopy (BAM)

The surface pressure-area (π-A) isotherms of pure SP have been published previously.[9,37] The limit area per molecule of hemicyanine in pure dye film is close to 0.33 nm^2.[13] BAM images of SP monolayers reveal inhomogeneous films (see Supporting Information), with the coexistence of dark regions surrounded by bright areas. This situation persists at high surface pressures, which is indicative of an irregular structure in the monolayer formed. π-A isotherms of SP show the dependence on the counterion type and concentration used,[9,13-15,37] which significantly affects the H-aggregation shown for this compound at the air-water interface.[9-15] Presumably, such inhomogeneity of the SP monolayers is due to the imbalance between the perpendicular sections of the alkyl chain (~0.2 nm^2) and of the polar group (~0.33 nm^2), which

prevents the formation of organized large-size structures at the interface. As a strategy to promote a proper balance between the sizes of the hydrophobic and hydrophilic groups, we have studied mixed monolayers of SP and DMPA at different molar fractions, $x = n_{SP}/(n_{SP} + n_{DMPA})$. Thus, for a molar ratio $x = 0.5$ (SP:DMPA = 1:1 monolayers), the DMPA molecule provides two aliphatic chains to the set, so the minimum perpendicular section of the 1:1 mixture would be around 0.6 nm^2 per SP molecule. The anionic DMPA can also offset the positive charge of the SP molecule, which favors the complete miscibility of the mixture. Finally, it has to be highlighted the fact that the alkyl chains of DMPA are shorter than that of SP. Therefore, it is expected the DMPA headgroup is next to the hemicyanine pyridyl group, although close to the hydrophobic region of the assembly, so that the DMPA polar group does not avoid the hemicyanine aggregation by the dye molecular tilt (see the idealized sketch shown in Scheme 1B). Consequently, the hemicyanine group would have freedom of movement, bending properly to allow its aggregation.

Monolayers of SP:DMPA = 1:1 ($x = 0.5$) have been formed at the air–water interface by the co-spreading method. Figure 1 (top-left) shows its surface pressure–area (π–A) isotherm at 21ºC. As can be seen, the take-off of the isotherm occurs at 2.2 nm^2/SP molecule, and the isotherm shows an overshoot at 10 mN/m and 1.54 nm^2, approximately. After the overshoot, the surface pressure increases again with the decreasing area per molecule. At $\pi = 50$ mN/m, the surface area is $A = 0.6$ nm^2/SP molecule, which corresponds to three totally vertical alkyl chains, that is, two per DMPA molecule and one per SP molecule. Simultaneous to the isotherm recording, the morphology of the mixed monolayer at the air–water interface is directly observed by BAM. At low surface pressure only gas phase is observed (Figure 1A). When the surface area decreases, the monolayer appears to be homogenous (Figure 1B), indicating the complete miscibility of the components. At $\pi \approx 8$ mN/m, small circular domains appear (Figure 1C). These circular domains have inner textures with different brightness. Thus, the circle regions located above and below are darker than the environment, while the lateral regions of the circle are brighter. Before the overshoot, some branches grow from the circles. The brightness of these branches depends on the direction of their growth, that is, those growing in the horizontal direction are dark, while they are bright along the vertical direction, which one is coincident with the laser incidence. After the overshoot, BAM allows us to observe some branches changing the

direction of their growth together with their brightness (Figure 1D). Under further compression, the branches grow lengthwise, but not transversally (see Figures 1E and 1F). Finally, at high surface pressure, the surface is completely covered with branch domains with different brightness, depending on their longitudinal direction (Figures 1G and 1H).

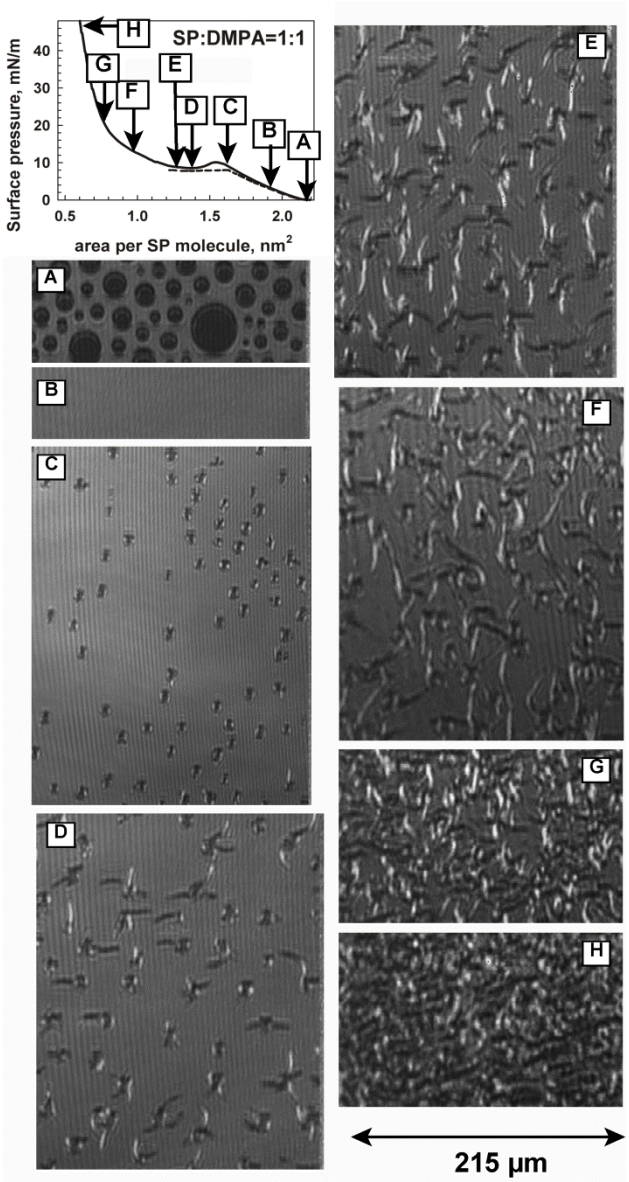

Figure 1: Surface pressure–area (π–A) isotherms of the mixed SP:DMPA monolayer in a molar ratio 1:1 at T = 21 ºC (top-left). Dashed line represents the isotherm under compression from 0 to 8 mN/m and the area evolution at 8 mN/m. A)–H) BAM images of the mixed SP:DMPA = 1:1 monolayer under different surface pressures at the air−water interface. Image size: 215 µm width.

On the other hand, the temperature has a dramatic effect on the morphology of the domains. Figure 2 (top-left) shows the π–A isotherms at 17, 21 and 25ºC for the SP:DMPA = 1:1 monolayer. Under these conditions, the take-off of the isotherms decreases and the isotherm overshoot is shifted to higher surface pressures as the temperature increases. However, at high surface pressure the isotherm areas are independent of the temperature. Figure 2 also shows BAM images recorded at 25ºC and 17ºC. For both temperatures circular domains with inner textures can be observed. At 25ºC, and as in the previous case, branches grow from these domains, which are wider and shorter on average than those observed at 21°C, and also the brightness of the branches depends on the direction of the growth (Figure 2B and 2C). Notoriously, there is no growth of branches at 17ºC (Figures 2D-2F). In any case, circular domains have the same inner textures that in the previous case.

The BAM images shown in Figures 2D-2E correspond to the π–A isotherm at 17°C, during the first compression cycle. When the monolayer is decompressed, and a second compression process is realized, some hysteresis at low surface pressure happens (see Figure 2, top-left, grey line). The hysteresis at low surface pressure is related to the fact that the domains do not disappear completely when the monolayer is expanded. However, a significant phenomenon is observed during the second compression process, that is, the circular domains grow much more than those in the previous cases (see Figure 2F and 2G). Initially (Figure 2F), circular domains have the same inner textures that those during the first compression. However, during the growth of such domains, the outer layers of them adopt a slightly different brightness, and result in the formation of branches (Fig. 2G).

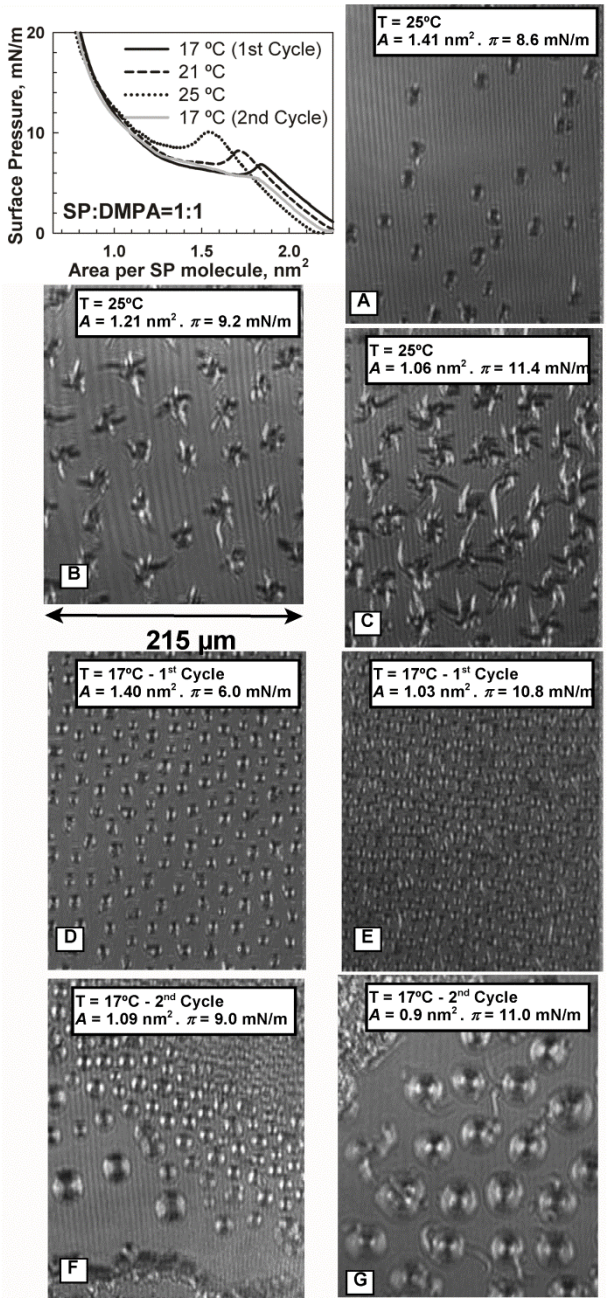

Figure 2: *π–A* isotherms of the mixed SP:DMPA monolayer in a molar ratio 1:1 at 17 ºC (first and second compression processes), 21 ºC and 25 ºC (top-right). A)–G) BAM images of the mixed SP:DMPA = 1:1 monolayer under different surface pressures and temperatures. Image size: 215 µm width.

It is necessary to indicate that the isotherm overshoot cannot be observed during the second compression isotherm (Figure 3, grey line), and neither for the *π–A* curves obtained during the expansion of the monolayer (data not shown). An additional experiment was realized, which consisted in comprising the SP:DMPA = 1:1 monolayer up to a surface pressure prior to the overshoot ($\pi \approx 8$ mN/m), and the spontaneous

evolution of the monolayer at this constant pressure was registered (see top-left in Figure 1, dashed line). We observed that the area decreased to a value close to 1.2 nm^2/per SP molecule, while BAM images showed circular domains and branches growing from the circles, with similar textures than those described in Figure 1. Based on the above indicate, the existence of the isotherm overshoot could be interpreted in terms of a *dynamic jump,*[38] related to the kinetics of the monomer attachment to 2D aggregates. In fact, the formation of oligomers results in the decrease of the excess surface pressure of the monolayer. In these cases, the existence of the overshoot can be qualitatively explained by the fact that the aggregation rate is relatively slow due to the increase of the number of monomers in the aggregate.

It should be noted that the BAM images of pure DMPA monolayer or pure SP monolayer, do not show the morphological behavior observed in Figures 1 and 2.[39,40] It has been shown how some macrocations can be electrostatically attached to a DMPA matrix,[41-46] forming domains without internal textures, because of the weak or no aggregation between these macrocations. However, hexagonal and circular domains with inner textures were observed for mixed DMPA/Methylene Blue (MB) monolayers,[8] although those circular domains had different textures in comparison with those observed here. As for MB, we can assert that the molecular aggregation of SP induces the formation of domains with well-organized structure. Moreover, the texture of the domains observed depending on their orientation, is indicative of anisotropic structures. An additional fact that deserves mention is the absence of the coalescence between domains.

Figure 3 shows the π–A isotherms of SP:DMPA monolayers, obtained at various molar fractions of SP, as well as some BAM images recorded simultaneously. In this figure, the isotherm areas are expressed per molecule. It has to be pointed out that the isotherm overshoot could not be observed for $x \neq 0.5$. For $x = 2/3$, small circular domains with inner textures and without branch growth can be observed by BAM (Figures 3A-B). However, in this mixture the domains are poorly displayed, because the reflectivity of the brightest areas of the domains is similar to the reflectivity of the surrounding areas. For $x = 1/3$ (Figures 3C-D), domains without inner textures are observed (Figure 3C), which are transformed into a lattice structure at high surface pressure (Figure 3D). As in the previous case, domains without structure are formed for $x = 1/6$, but the domains coalesce in this case as the surface pressure increases. For high

surface pressure, the plot of the area per molecule *vs* composition at a constant pressure shows a minimum at x = 0.5 (see Supporting Information), which agrees with the formation of a 1:1 complex. Moreover, only one collapse pressure is observed for all the binary mixtures, which is indicative of miscible components.

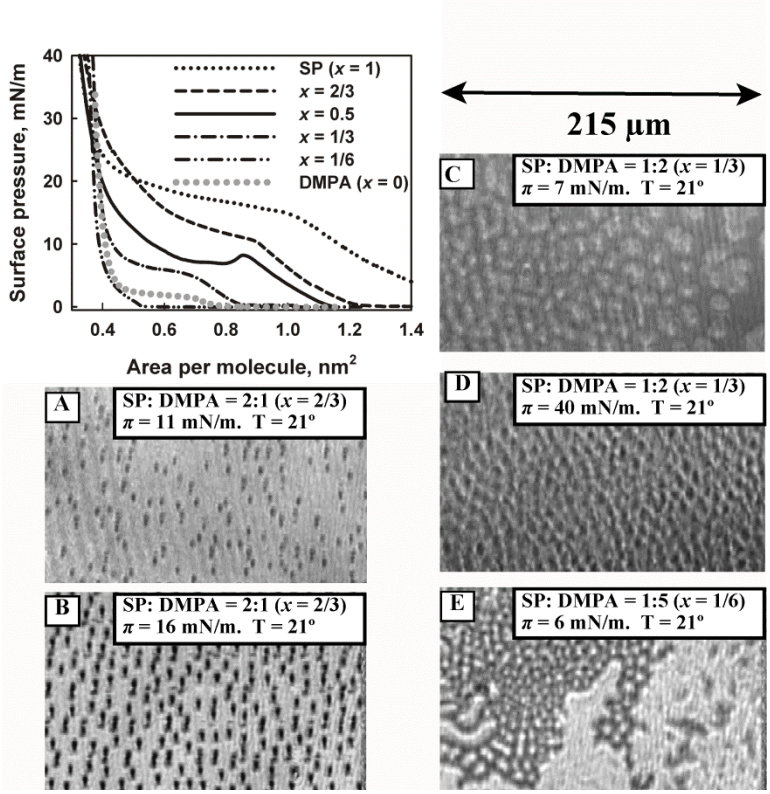

Figure 3: Surface pressure–area (π–A) isotherms of the mixed SP:DMPA monolayer at various mole fractions of SP (x) at T = 21°C. The isotherm areas are expressed per molecule, (top-left). A)–E) BAM images of the mixed SP:DMPA monolayer at different x values. The experimental conditions are indicated in the figure. Image size: 215 µm width.

Additionally, some experiments for the SP:DMPA = 1:1 monolayer, by using buffered subphase (acetic acid /acetate 10^{-5} M), were carried out. We observed that isotherms and BAM images do not show any differences from those obtained by using unbuffered subphase.

4.1.3.2. Synchrotron Grazing Incidence X-ray Diffraction (GIXD)

Grazing Incidence X-ray Diffraction (GIXD) measurements have been performed in order to obtain quantitative information about the 2D symmetry of Langmuir monolayers. GIXD is sensitive only to the condensed parts of the monolayer, giving an ordered structure that can result in X-ray diffraction. The liquid expanded phase contributes to the background scattering. Structural changes along compression occurring for the SP:DMPA = 1:1 mixed monolayer have been monitored. The X-ray diffraction patterns were recorded before and after the overshoot of surface pressure (ca. 10 mN/m). Moreover, the further effect of maintaining the surface pressure under a constant value of 10 mN/m has been studied, as it implies an elongation of the branches observed by BAM (see Figure 1). GIXD has been also performed at a higher value of surface pressure of 25 mN/m. Figure 4 shows the corrected X-ray intensities as a function of the scattering vector components Q_{xy} and Q_z for the mixed SP:DMPA monolayer at 10 mN/m and different times after compression. Diffraction peaks and rods values are depicted in Table 1, among with their full-width at half-maximum values. Quantitative information on the unit cell parameters can be found in Table 2. Tilt angle and cross sectional area are also described. For comparison purposes, the pure DMPA monolayer has also been studied (see Supporting Information). The pure DMPA monolayer shows three different phases, as going from low to high surface pressures. At 5 mN/m the lipid forms an Overbeck (Ov) phase. With compression of the monolayer, at 10 mN/m the DMPA monolayer undergoes a phase transition to a L_2 phase. In the L_2 phase, the distortion of the lattice is significantly smaller. The tilt angle of the hydrocarbon chains is also reduced. At a high surface pressure of 30 mN/m, the DMPA monolayer shows a LS phase, in which the lipid tails are untilted. The transition into the non-tilted state occurs at ~15 mN/m. Therefore, an increase of the lipid ordering, as well as a progressive decrease of the in-plane area, is observed with compression of the monolayer (see Supporting Information).

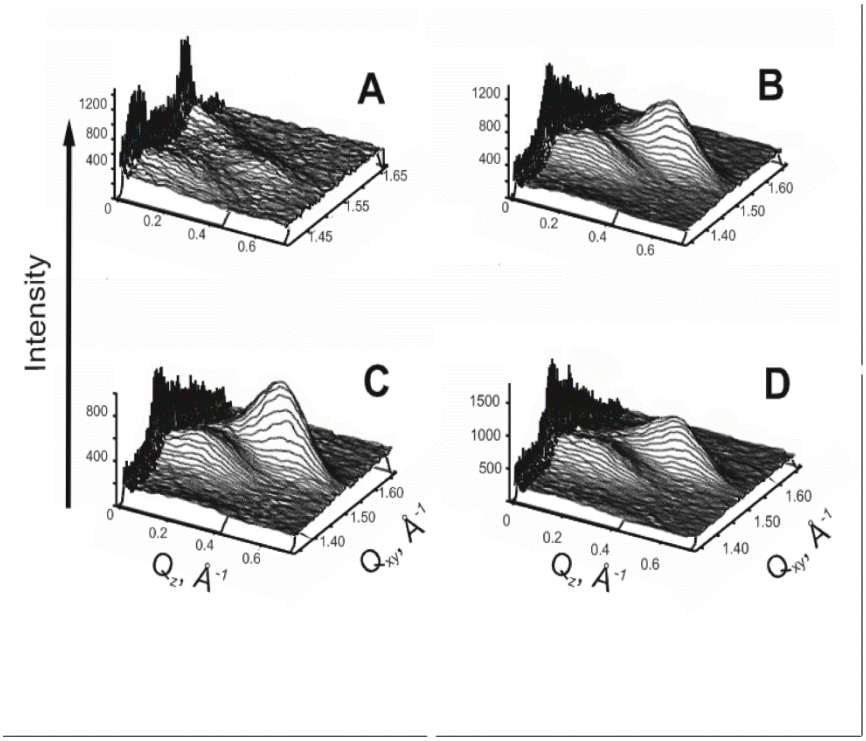

Figure 4: 3D plots of the corrected X-ray intensities versus the in-plane and out-of-plane scattering vector component Q_{xy} and Q_z for the mixed SP:DMPA monolayer in a molar ratio 1:1 at T = 21°C. A) π = 10 mN/m, before surface pressure overshoot (see isotherm of Fig. 1). B) π = 10 mN/m, after ca. 20 minutes of maintaining the surface pressure constant (after the overshoot). C) π = 10 mN/m, after ca. 40 minutes of maintaining the surface pressure constant. D) π = 25 mN/m.

Figure 4 (A) shows the diffraction patterns for the mixed monolayer SP:DMPA = 1:1 just before the overshoot of surface pressure (see isotherm in Figure 1), at ca. 10 mN/m. Two crystalline phases can be distinguished: a) an orthorhombic, untilted phase. This phase shows two Bragg peaks both at Q_z = 0, with Q_{xy} = 1.44 Å^{-1} and Q_{xy} = 1.58 Å^{-1}. The hydrocarbon tails are tightly packed. b) An Overbeck (Ov) phase[47,48] showing two Bragg peaks at Q_{xy} = 1.45 Å^{-1}, Q_z = 0.23 Å^{-1}, and Q_{xy} = 1.52 Å^{-1}, Q_z = 0.46 Å^{-1}. The overshoot of surface pressure causes a modification of the mixed monolayer, observed by BAM as growth of branches (see Figure Fig. 1 C-F). The effect of this mesoscopic rearrangement on the molecular structure of the mixed monolayer is described using GIXD. Figure 4(B) shows the diffraction patterns for the 1:1 mixed monolayer after a waiting time of ca. 30 minutes. The Bragg peaks belonging to the orthorhombic phase give a weaker signal, indicating a decreasing amount with time in the mixed monolayer. However, they can still be quantified. The structural parameters of the orthorhombic phase do not significantly change with further compression of the mixed monolayer.

Regarding the Ov phase, the intensity of the diffraction peaks increases their intensity with time at a constant pressure of 10 mN/m. This increase indicates a larger contribution of this phase to the global structure of the monolayer. The distortion of the lattice decreases slightly with time, but the chain tilt and the cross-sectional area are unchanged (see Table *2*). This relaxation may be related with the growth of the branches observed by BAM (Figure 1, C-F). Figure 4 (C) shows a decrease of the intensity for the orthorhombic phase Bragg peaks. An increase of the intensity for the Bragg peaks belonging to Overbeck phase can also be observed. As seen in Table *2*, there is no significant change in the structural parameters for the Overbeck and orthorhombic phases. The crystalline structure of the mixed monolayer has also been examined at a high value of surface pressure. Figure 4 (D) shows the diffraction patterns for the 1:1 mixed monolayer at a surface pressure of 25 mN/m. As noted previously, there is a further increase of intensity for Bragg peaks belonging to Overbeck phase. This behavior permits us to relate the circular domains with the orthorrombic phase and the branches grown from the circles with the Overbeck phase.

As seen in Table 2, for the Overbeck phase a little decrease of the tilt angle of the hydrocarbon chains, while maintaining the packing, is observed. There is a slight increase in the distortion of the lattice. Additional information from the full-width at half-maximum of Bragg rods (fwhm(Q_z)) can be obtained. The length of the scatter l can be defined as $l = 0.88(2\pi)/\text{fwhm}(Q_z)$.[49] For the orthorhombic phase, l is ca. 1.7 nm, corresponding to the length of the DMPA hydrocarbon chains on *all-trans* conformation. In the case of the Overbeck phase, l is ca. 2.5 nm. This length agrees well with the length of the hydrocarbon chain for the SP molecule in *all-trans* conformation. Therefore, it is expected that in this phase the DMPA molecule is packed with the glycerol group region stretched and also forming part of the scattering unit. This conformation confirms the assumption in section 1. Based on the shorter length of the DMPA chains, the DMPA molecule is able to interact to a higher extent, in this case even ordering the glycerol region, with SP molecules.

Table 1: In-plane Q_{xy} and out-of-plane Q_z components of the scattering vector of the mixed SP:DMPA = 1:1 monolayer at T = 21°C. The full-width at half-maximum (FWHM) of the peaks are given in parentheses.

Table 1							
π, mNm^{-1}	Orthorrombic phase			Overbeck phase			
	Q_{xy1}, Å^{-1}	Q_{xy2}, Å^{-1}	Q_z, Å^{-1}	Q_{xy1}, Å^{-1}	Q_{xy2}, Å^{-1}	Q_{z1}, Å^{-1}	Q_{z2}, Å^{-1}
10 (directly after compression)	1.446 (0.112)	1.582 (0.033)	0 (0.34)	1.453 (0.053)	1.526 (0.080)	0.231 (0.23)	0.462 (0.23)
10 (after 20 min)	1.447 (0.026)	1.580 (0.063)	0 (0.34)	1.466 (0.036)	1.521 (0.053)	0.228 (0.22)	0.456 (0.22)
10 (after 40 min)	1.451 (0.033)	1.580 (0.057	0 (0.35)	1.469 (0.031)	1.521 (0.052)	0.23 (0.22)	0.46 (0.22)
25	1.452 (0.031)	1.577 (0.066)	0 (0.31)	1.470 (0.033)	1.527 (0.057)	0.22 (0.22)	0.44 (0.22)

Table 2: Primitive unit cell parameters, distortion values, tilt angle, projection of hydrocarbon chains in xy plane (A_{xy}) and cross sectional area of hydrocarbon chains (A_0) of the mixed SP:DMPA = 1:1 monolayer at T = 21°C.

Table 2	Orthorhombic phase							
π, mNm^{-1}	a, Å	$b = c$, Å	α, deg	$\beta = \gamma$, deg	distortion	tilt angle, deg	A_{xy}, Å^2	A_0, Å^2
10 (directly after compression)	4.465	4.485	125.6	117.2	0	0	19.4	19.4
10 (after 20 min)	4.473	4.884	125.5	117.3	0	0	19.4	19.4
10 (after 40 min)	4.477	4.884	125.3	117.3	0	0	19.4	19.4
25	4.488	4.874	125.2	117.4	0	0	19.4	19.4
	Overbeck phase							
π, mNm^{-1}	a, Å	$b = c$, Å	α, deg	$\beta = \gamma$, deg	distortion	tilt angle, deg	A_{xy}, Å^2	A_0, Å^2
10 (directly after compression)	5.081	4.838	116.6	121.7	0.0663	16.8	20.9	20.0
10 (after 20 min)	5.013	4.832	117.5	121.2	0.0496	16.7	20.7	19.8
10 (after 40 min)	4.999	4.828	117.6	121.2	0.0469	16.8	20.7	19.8
25	5.002	4.815	117.4	121.3	0.0513	16.1	20.6	19.8

4.1.3.3. Reflection Spectroscopy and determination of SP polar angle in the mixed SP:DMPA monolayers

Reflection spectroscopy detects only those molecules which are at the interface and contribute to enhanced reflection from the air–water interface.[36] This technique gives us valuable information on the organization, density and orientation of the chomophore molecules located at the air–water interface.[3,19,41,44] Reflection spectra ΔR of SP:DMPA = 1:1 monolayers on water subphase at different surface pressures, are shown in Figure 5A.

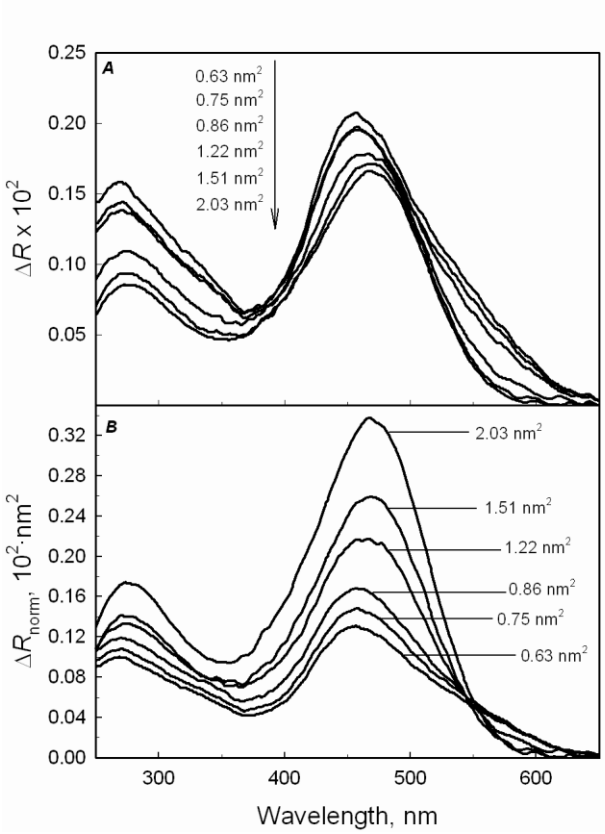

Figure 5: A) Reflection spectra Δ*R* of the mixed SP:DMPA monolayers, molar ratio 1:1. The surface areas are indicated in the Figure. B) Normalized reflection spectra.

For low values of absorption, the reflection Δ*R* has been shown to be proportional to the surface concentration of the dye, and is given in a reasonable approximation by[16,19,36,41]

$$\Delta R = 2.303\times10^{3}\,\Gamma\, f_{orient}\,\varepsilon\sqrt{R_i} \qquad (1)$$

where Γ is the surface concentration in mol cm^{-2}, R_i = 0.02, the reflectivity of the interface air–water at normal incidence, ε the extinction coefficient given as L mol^{-1} cm^{-1}, and f_{orient} is a numerical factor that takes into account the different average orientation of the square transition moment of the dye in solution as compared to the monolayer at the air–water interface. For the domains observed in BAM images, the features of inner bright and dark regions indicate anisotropy. However, for a large region of the interface which includes numerous domains with a random distribution an isotropic film in the plane is considered and, therefore there is not preferential azimuthal angle, ϕ. This just happens during the reflection measurements. In this case, f_{orient} is[19]

$$f_{orient} = \frac{3}{2}\left\langle \sin\ \theta^{2} \right\rangle \qquad (2)$$

where brackets indicate average values. The polar angle, θ, is defined as the angle between the SP transition moment, μ, and the normal to the air–water interface, while the azimuthal angle, ϕ, is defined as the angle between the projection of μ on the *x-y* plane and the x axis (see Scheme 1B).

If we considered that Γ = 1/($A \times N_A$), where A is the area per SP molecule and N_A the Avogadro constant, we can rewrite equation (1) as

$$\Delta R_{norm} = \Delta R \times A = 5.407 \times 10^{8}\ f_{orient}\ \varepsilon \qquad (3)$$

The corresponding product $\Delta R \times A = \Delta R_{\mathrm{norm}}$ are shown in Figure 5B. The quantity ΔR_{norm} is proportional to the product $f_{orient} \cdot \varepsilon$, and represents the reflection normalized to the surface density of SP. Therefore, they show more clearly the changes of orientation and/or association than the directly measured spectra.

At low surface pressures (π < 5 mN/m), the spectra present a low-energy band at 475 nm, corresponding to the π-π* transition over the chromophore in trans configuration, and a band at 265 nm arising from the isolated transition on the pyridinium and phenyl moieties.[50,51] As the surface pressure increases, some phenomena take place in the reflection band: 1) ΔR_{norm} at 475 and 265 nm decreases, which should be related to the decreasing of the polar tilt angle of the chromophores; 2) for π > 5 mN/m, the maximum wavelength of the low-energy band shifts to shorter

wavelengths (from 475 nm to 459 nm), this fact must be attributed to the formation of H aggregates of the SP chromophores.[37,50-52]

The oscillator strength is defined as[53]

$$f = \frac{4\varepsilon_0 2.303 m_e c_0}{N_A e^2} \int_{Band} \varepsilon d\nu = 1.44 \times 10^{-19} \int_{Band} \varepsilon d\nu \qquad (4)$$

where ε_0 is the permittivity of vacuum, m_e the electron mass, e the elementary charge, and c_0 the speed of light in a vacuum. In eq 4, the numerical factor 1.44×10^{-19} is expressed in mol L^{-1} cm s. From equations 1, 3 and 4, is possible to define an apparent oscillator strength determined from the measured reflection spectra as[19]

$$f_{app} = f \times f_{orient} = 2.6 \times 10^{-12} \int_{Band} \Delta R_{norm} d\nu \qquad (5)$$

where the numeric factor 2.6×10^{-12} is expressed in nm^{-2} s. Moreover, the ratio between the apparent oscillator transition and the oscillator strength from the solution gives the orientation factor, $f_{orient} = f_{app} / f$. If the oscillator strength for any aggregation degree is conserved, according to the Davidov model,[8,53-55] the average polar tilt angle θ could be evaluated by using eq 2. However, the oscillator strength of the hemicyanine group depends on the solvent polarity,[13] so we do not have a proper reference value for f.

An alternative way to estimate the chromophore angle is assuming that the hemicyanine group is located flat with respect to the interface for large surface areas, that is, $\theta \approx 90º$. In these cases, for $A > 1.8$ nm^2, $f_{app} \approx 1.2$ has been calculated, and thus the oscillator strength is $f \approx 0.8$ (equations 2 and 5). This value is close to those published for species with similar dye groups, and ranged between 0.67-0.78.[13]

The interface is completely covered by domains for $A \leq 0.7$ nm^2, where the surface pressure increases sharply (see Figure 1). $A \approx 0.7$ nm^2 should be the area corresponding to that occupied for hemicyanine molecule (or per DMPA) in the circular and branch domains. For these areas, values of $f_{app} \approx 0.7$ were obtained, and according to eq 2, $\theta \approx 50º$.

Therefore, the reflection spectra analysis shows two fundamental phenomena as the surface pressure increases, firstly the formation of H aggregates (shifting of the

visible band toward lower wavelengths), and secondly the tilt of the hemicyanine group (decreasing of the apparent oscillator strength).

The area limit per SP molecule in the pure dye film is close to $A_0 \approx 0.33$ nm^2,[13] and corresponds to a vertical orientation of the hemicyanine group. The polar angle obtained, $\theta \approx$ 50º, is indicative that the hemicyanine group extends to occupy much of the available area at the air-water interface. The projected area of the chromophore onto the surface assuming a tilt angle of 50 degrees has been estimated by means of HypeChem 6.0,[56] obtaining a value of 0.64 nm^2, approximately. This value agrees with the idea that the polar group of DMPA hardly occupies a net area at the interface, and is probably located next to the hemicyanine pyridyl group, but immersed in the boundary between hydrophobic and hydrophilic regions (see Scheme 1B).

4.1.3.4. The organization of hemicyanine polar group and the simulation of Circles Domain Textures

Scheme 2A shows some circular domains observed by BAM at different temperatures. Also, Scheme 2B shows some domains observed at 17 °C for a second cycle under compression. As discussed earlier, the texture of these domains is the same, that is, with bright lateral and dark vertical regions.

The experimental BAM reflectivity is a relative amount. If the exposition time to the reflected light (auto set function in the BAM equipment) is increased, improved resolution of the dark regions is achieved, counter the decreased resolution for the bright areas (Scheme 2C). In this case, although the general texture is similar to that observed previously at 21 ºC, the circular domain textures show a thin vertical grey region surrounded by darker regions (see Scheme 2C).

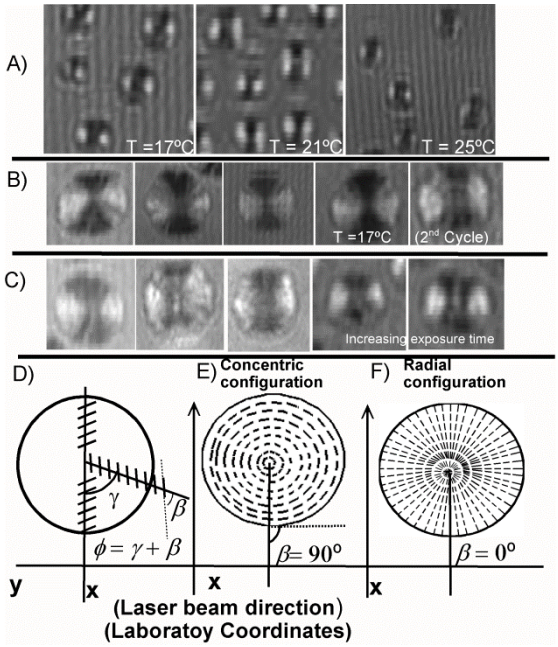

Scheme 2: A) Zoom of experimental circular domains observed by BAM at different temperatures. B) Domains observed at 17 °C during the second cycle of compression. C) Domains observed at 17 °C during the second cycle of compression by increasing the opening time of the BAM camera lens. D) Organization model of the 2D circular domain of the mixed SP:DMPA = 1:1 film and definition of γ (the angle formed between the x axis and any radial circle), and β (angle between projection of the dipole moments on the x-y plane and the radial direction). Dashed line represents the projection of the transition dipole on the x-y plane. E) Concentric configuration (β = 90º). F) Radial configuration (β = 0º).

In a BAM experiment, p-polarized light reaches the air−water interface with an angle α = 53.15º, Brewster angle. Usually, the different BAM textures are observed due to changes of the refractive index resulting from differences in thickness, density and/or molecular orientation between the different regions of the film. However, for our system, the SP molecules absorb at 532 nm laser beam (see Figure 3). As previously suggested, the domain formation is induced by the SP aggregation whose absorption originates the strong changes in the film refractivity. Therefore, this phenomenon would be mainly responsible for the appearance in a first approximation of domain textures. In such a case, the Fresnel equations for biaxial anisotropic materials on isotropic substrate should be used to calculate the reflection of the film.[57]

The SP:DMPA = 1:1 mixed film is assumed to be a biaxial material with complex refractive indices of $N_q = n_q - ik_q$ ($q \equiv x$, y and z, See Supporting Information).

To obtain the BAM images the analyzer was fixed at 0º, and therefore, only the p component of the reflection is detected. Thus, the N_y component does not affect to the final result. Moreover, the absorption coefficients can be expressed as follows: $k_x = k_0 \times \sin(\theta) \times \cos(\phi)$, and $k_z = k_0 \times \cos(\theta)$. Assuming values for the different constants (k_0, n_y,

n_z, θ, ϕ, and the thickness of the film, d), the absolute reflectivity of the film can be determined. Following, this absolute reflection must be transformed into a relative grey level scale (from 0 to 255) for the simulation of the domain texture. Details of the simulation procedure are given in the Supporting Information. From reflection spectra $\theta \approx 50^{\circ}$ is calculated, being estimated the values for $k_0 \approx 0.15$, $n_y = n_z \approx 1.6$, and $d \approx 3.7$ nm. In such a way, the reflectivity depends exclusively on ϕ. This simulation model is only approximate because the anisotropy of the DMPA alkyl chains is not considered.

From now on, the axis x (laboratory coordinates) is defined as the projection of the laser incidence axis on the interface (see Scheme 2D).

If the presence of the vertical gray region in the circular domains is ignored, at this discussion point, we can consider that the reflectivity inside each circle changes progressively with the rotation angle, being brighter at the lateral position of the circle than at the vertical position. Also, the reflectivity is almost constant for any radius of the circle, which permits us to suppose that the azimuthal angle ϕ of the hemicyanine group is constant for a given radial direction (see Scheme 2D). In any case, some small changes in the texture can be appreciated, which should be linked to fluctuations in the molecular orientation.

It is denoted by γ the angle formed between the x axis and any radius of the circle (circle rotation angle), and β the angle between projection of the dipoles moment on the x-y plane and the radial direction (see Scheme 2D). In this way, the azimuthal angle is $\phi = \gamma + \beta$. Schemes 2E and 2F show sketches for $\beta = 90^{\circ}$ (concentric configuration) and $\beta = 0^{\circ}$ (radial configuration) respectively, where dashed lines represent the projection of the transition dipole on the x-y plane.

As previously observed, the regions located at the lateral position of the experimental circle domains are always brighter than those located at the vertical position. Usually, this type of texture indicates a preferential perpendicular orientation of the transition dipoles along to the radial direction ($\beta = 90^{\circ}$, Scheme 2E-concentric configuration). However, the reflected light (p-polarized) of thin films under Brewster angle incidence is not a linear phenomenon and the simulation is necessary to clarify some experimental details as, for example, the thin grey vertical region observed in the texture domain. As discussed below, this phenomenon is not due to a change in the dipole orientation, but an optical effect resulting from the reflection at the Brewster angle incidence.

Figure 6A shows the results of the circular domain simulation for different polar tilt angles θ, and for different β angles, by using k_0, n_y, n_z and d values estimated previously. In any case, the simulated brightness (reflectivity) of the domains is a relative amount, and is related to the minimum and maximum reflection of each case (see Supporting Information). We have observed that for $\theta \geq 60º$ and $\beta = 90º$ (concentric configuration), the texture appearance of the domain is approximately coincident with that experimentally registered (Schemes 2A and 2B). However, for $\theta \leq 30º$, where the absolute reflectivity is low (see Supporting Information), the texture appearance is also coincident with the experimental domains when $\beta = 0º$ (radial configuration) (Schemes 2A and 2B).

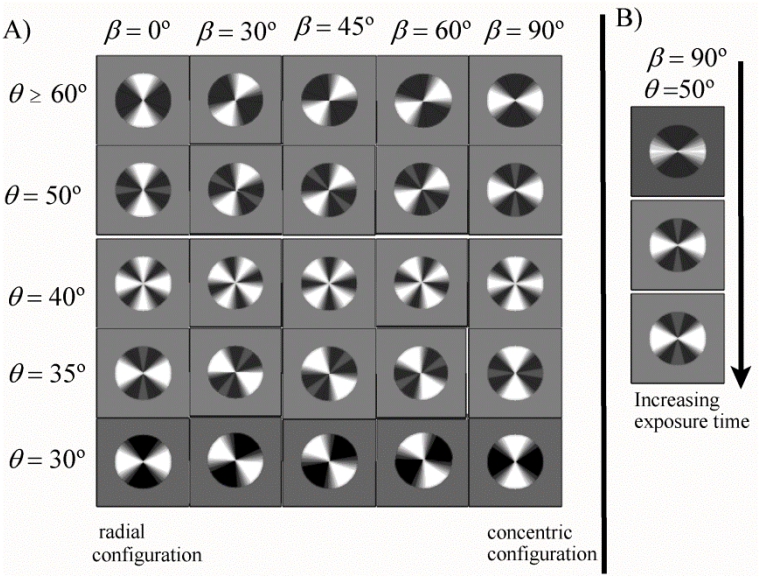

Figure 6: A) Circular domain simulation for different polar angle tilt, θ, and different angle β, by using $k_0 = 0.15$, $n_y = n_z = 1.6$, and $d = 3.7$ nm. B) Theoretical texture of the circular domains, for $\theta = 51º$ and $\beta = 90º$, where the exposure time to the light is simulated (see Supporting Information).

For $\theta = 50º$ and $\beta = 90º$, and for $\theta = 35º$ and $\beta = 0º$, the model predicts the appearance of a narrow gray region along the vertical direction of the circular domain, surrounded by darker regions (see Figure 6A). This fact agrees with the experimental texture observed when the reflectivity increases (see Scheme 2C). The theoretical textures of the circular domains, for $\theta = 50º$ (from reflection spectroscopic analysis) and $\beta = 90º$, are shown in Figure 6B, where the exposure time to the light has been also simulated (see Supporting Information). The results show the thin gray vertical region

could be better defined as the exposure time increases. For β = 90º, the size of this gray region decreases as θ increases, disappearing completely when $\theta \geq$ 60º. For β = 0º, the size of this gray region decreases as θ decreases, disappearing completely for θ = 30º.

Unfortunately, the theoretical texture changes as a function of θ (Figure 6A), cannot be observed because the experimental polar angle remains almost constant under any experimental condition, even when the temperature is changed. Therefore, the two situations in which the texture of the simulated domains matches with those experimental, that is, $\theta \approx$ 50º and β = 90º, or $\theta \approx$ 35º and β = 0º, cannot be distinguished.

However, it is possible to change the texture of the experimental domains varying slightly the incidence angle of the polarized light. Thus, for the k_0, n_y, n_z and d values used previously, the Fresnel's equations predict the maximum reflection for ϕ = 0º and 180º when $\alpha \leq 53°$, and independently of the θ value. Whereas if $\alpha \geq 53.8°$, the reflection is maximum for ϕ = 90º and 270º, also for any θ value (see Supporting Information). Figures 7a, 7b and 7c (top) show domain textures with $\alpha = 52°$, $\alpha = 53.15°$ and $\alpha = 54°$, respectively.

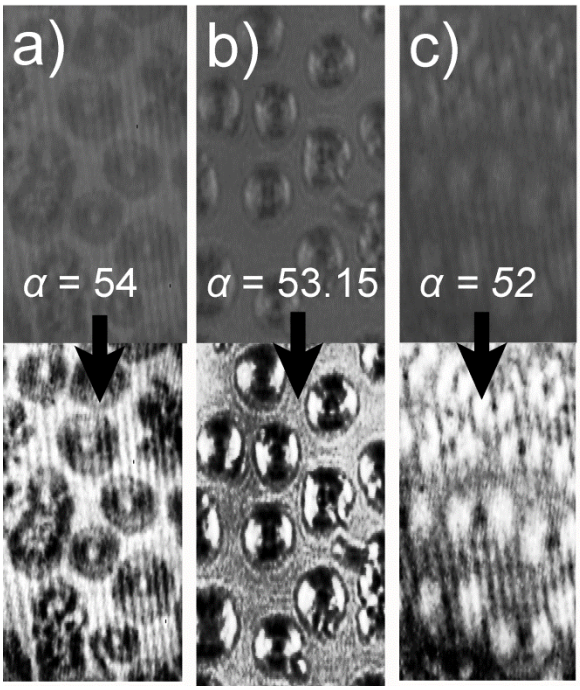

Figure 7: Top: Experimental domains texture (T = 17 ºC) by using $\alpha = 52°$, $\alpha = 53.15°$ and $\alpha = 54°$. Bottom: Equalized images.

For α = 52° and α =54°, the reflectivity increases considerably, and image resolution becomes worse. To improve such situation, the images in Figure 7 were equalized (bottom). As clearly observed, the domain texture is inverted when α changes from 52º to 54º. The key to distinguish between the two options proposed by the simulation ($\theta \approx$ 50º and β = 90º, or $\theta \approx$ 35º and β = 0º) is the following: for the experimental domain, the texture is the same for α = 52° and α = 53.15°, and therefore, in both cases the maximum reflectivity corresponds to ϕ = 0º and 180º. In these cases, since the bright regions are located in the lateral positions of the circles, γ = 90° or 270°, and with $\phi = \gamma + \beta$, β = 90º or 270º can be deduced, that is, a concentric configuration. Therefore, one could argue that $\theta \approx$ 50º. This result is coincident with that previously obtained from the reflection spectra.

Inside the circular domains obtained for the SP:DMPA = 1:1 system, the hemicyanine group adopts concentric configuration but, in any case, the alkyl chains rearrange in orthorhombic configuration, as tested by GIXD.

4.1.3.5. Branches formation and hemicyanine polar group organization

At 17 ºC, during the second compression process, and when the circular domains are large enough, rings are formed around them, which are broken away from the central structure. This phenomenon is clearly observed in Figure 2G and Scheme 3A, and may help us to understand the mechanism of formation and growth of branches arising from the circular domains.

In circular domains, the SP molecules are aggregated along the radial direction with β = 90º (concentric configuration, see Scheme 2D), which somehow must minimize the domain energy. However, this energetic advantage seems to disappear when the domain grows too much, at least for external molecules whose circle curvature becomes negligible. Likewise, neither circular domains nor branches growing from them coalesce under compression, indicating an anisotropic line tension.[58-60] The anisotropic line tension may be originated by the different tilt of the lipid at the boundary of the domains, similar to the behavior of the liquid crystal.[61] In this case, like in liquid crystals, small defects originate the formation of regions or branches that grow independently of the central domain, and for which anisotropic line tension prevents their coalescence with the central domain. The number of defects increases with the

temperature, and so the proliferation of the number of branches arising from circular domains.

Once a branch is formed after the breakup of a ring segment of the circular domain, its growth is only along and not across the branch. Therefore, the growth of this branch-like domain is different to that for circular domains. Like for liquid crystal phases, the average projection of the dipole transition in the interface could be described by a unit vector called the director and denoted by **n** (see Scheme 3B). Because of the branch growth, the molecular aggregation is the phenomenon that defines the **n** direction. The molecular aggregation at the end of the branches is energetically favorable with respect to the aggregation at the circular domains. As commented previously, the brightness of these branches depends on the direction of their growth, that is, of the **n** direction. Thus, branches grown along the vertical direction are bright, whilst they are dark in the horizontal direction. Intermediate brightness is obtained as a function of the angle between x axis and **n**. When a branch changes its direction growth, its brightness changes simultaneously (see Scheme 3C). These changes in the brightness of the branches should be interpreted due to changes in the direction of the molecular aggregation, because of fluctuations or collisions with other domains. In any case, we must remember that BAM reflectivity is a relative magnitude.

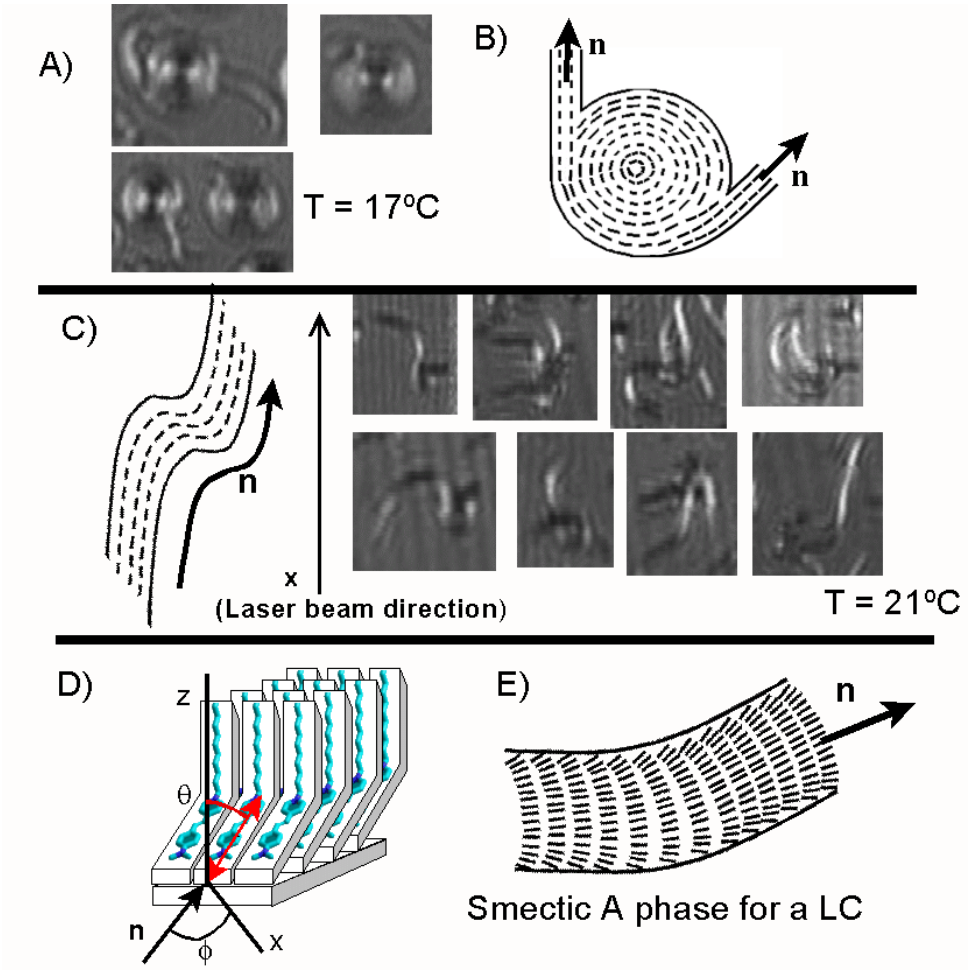

Scheme 3: A) Circular domains observed at 17 ºC (second compression process). B) Model of the branch growth, and definition of director, **n**. C) Simultaneous changes of reflectivity and the direction of growth for branch domains; a sketch interpreting such changes as a function of the direction changes of the director, **n**. E) Drawing of the aggregation of the hemicyanine group. F) Model of fan-type configuration for branch domains.

A sketch of the aggregation of the hemicyanine group is depicted in Scheme 3D. For simplicity, the DMPA molecule is not represented. The model resembles two-dimensional smectic A phase (see Scheme 3E), similar to that described for liquid crystal where there are positional order along the director and the layer normal to the director. In this case, the azimuthal angle, ϕ, is defined by the angle between **n** and x axis (laboratory coordinates). Anyhow, we must remember that the alkyl chains are packed in an Overbeck phase, as by GIXD. However, for the polar group, the orientation order is not perfect. For example, Scheme 3C shows how for some branches growing in the vertical direction, the central region of the branch is brighter than the lateral regions, which is related to the tilt of the dipole with respect to the director, possibly in a fan-type configuration (see Scheme 3E). This phenomenon increases with

the temperature (see branched domains in Figure 2C) and can be related to the anisotropic line tension of the domains.

4.1.4. Conclusions

In this work, the formation of mesoscopic 2D structures at the air-water interface from mixed SP:DMPA monolayers has been reported. For this system, lateral aggregation of the hemicyanine group induces the formation of domains with long-range order, showing different textures and indicating the existence of anisotropy. Thus, circular domains with bright horizontal regions and dark vertical regions have been observed. Furthermore, depending on the temperature, it is observed how branches grow from circular domains, whose brightness depends on the growth direction. Thus, BAM images allow us to see some branches that change their growth direction and their brightness simultaneously.

GIXD experiments for the SP:DMPA = 1:1 mixed monolayer show the coexistence of two phases, orthorhombic and Overbeck, at 10 mN/m, which account for the packaging of the alkyl chains. With increasing the waiting time at 10 mN/m, the Overbeck phase is increased at the expense of the orthorhombic phase, which increases its contribution to the global structure along the isotherm. At a high value of surface pressure of 25 mN/m, almost all the mixed monolayer is in the Overbeck phase, although there is still a small part of the monolayer in the orthorhombic phase. The orthorhombic phase structure is not modified along the isotherm, while the Overbeck phase structure is slightly modified under compression. This behavior permits us to relate the circular domains with the orthorhombic phase and the branches grown from the circles with the Overbeck phase. However, the texture of the domain formed observed by BAM does not depend on the packing of alkyl chains, but the rearrangement of the hemicyanine polar group, because this group absorbs at the laser wavelength used in BAM.

The experimental circular domain textures have been simulated in the basis of the Fresnel equations for biaxial anisotropic materials on isotropic substrates. Therefore, the refractivity of the film can be calculated. In our simulation model, it has been assumed that the reflectivity is only caused by the absorption of the hemicyanine group. The simulation results support that the tilt angle of the hemicyanine group must be around 50° (polar angle), in good agreement with the value obtained from reflection

spectra at the air-water interface. The light reflection (p-polarized) of thin films under Brewster angle incidence is a complex phenomena and the simulation is necessary to clarify some experimental details, for example, the thin grey vertical region surrounded by darker regions in the texture of circular domains. As demonstrated, this phenomenon is not due to a change in the dipole orientation, but to an optical phenomenon observed for certain values of polar angle, when the reflectivity is measured at the Brewster angle.

The experimental data obtained by means of GIXD and BAM are complementary and give us information about the rearrangement in the lipid (GIXD) and polar (BAM) regions of the monolayer, respectively. It is the hemicyanine aggregation which induces the domain formation, but there must be geometrical compatibility between the polar groups and alkyl chains to make possible the formation of large domains with well-defined structures.

The geometry of the structures formed depends crucially on a proper balance between the vertical sections of the hydrophobic and hydrophilic groups. We design a_c, as the interfacial area occupied by alkyl chains when are fully extended, i.e at high surface pressures. Thus, for the SP:DMPA = 1:1 monolayer, $a_c \approx 0.6$ nm^2. Moreover, we design as a_0 at the minimum interfacial area occupied by the surfactant hydrophilic or head group. Monolayers with $a_0 > a_c$ could result in stable but heterogeneous films, like for SP monolayers without DMPA (see Supporting Information), where $a_c \approx 0.2$ nm^2 and $a_0 \approx 0.33$ nm^2. When $a_0 << a_c$, homogeneous monolayers can be obtained, although generally unstable, and consequently with low collapse pressures. This happens, for example, for monolayers formed by substances without polar group, such as semifluorinated alkanes.[62,63] In general for homogeneous, insoluble and stable monolayers, $a_0 \leq a_c$, although the interactions between hydrophilic groups determine to a great extent the properties of the monolayer. For the mixed SP:DMPA = 1:1 monolayer, we cannot determine the contribution of DMPA polar group to the a_0 value. However, the experimental results indicate that the hemicyanine group tilts to fill the available surface excess at the interface (a_c - a_0), resulting in a effective packing where $a_0 \approx a_c$. The high lateral aggregation energy of the hemicyanine group counters the repulsion between dipole moments in the monolayer. This fact stabilizes the monolayer and enables the domains growth to mesoscopic sizes. In this way, the domain structure depends on the ability of the dye to fill the available area.

4.1.5 Supporting Information

1) Surface pressure-area isotherms and Brewster Angle Microscopy (BAM) of pure SP

Figure 1A shows the surface pressure-area isotherms and BAM images of pure SP on water subphase at 21 ºC.

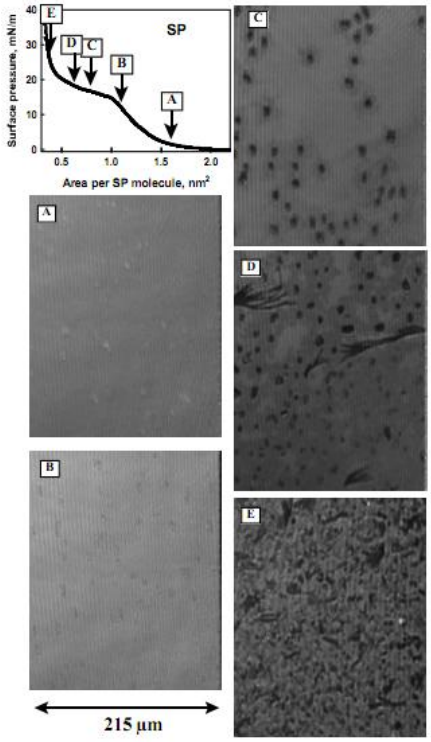

Figure 1A

2) Figure 2A shows the area per molecule *vs* mole fraction of SP at different constant values of surface pressure.

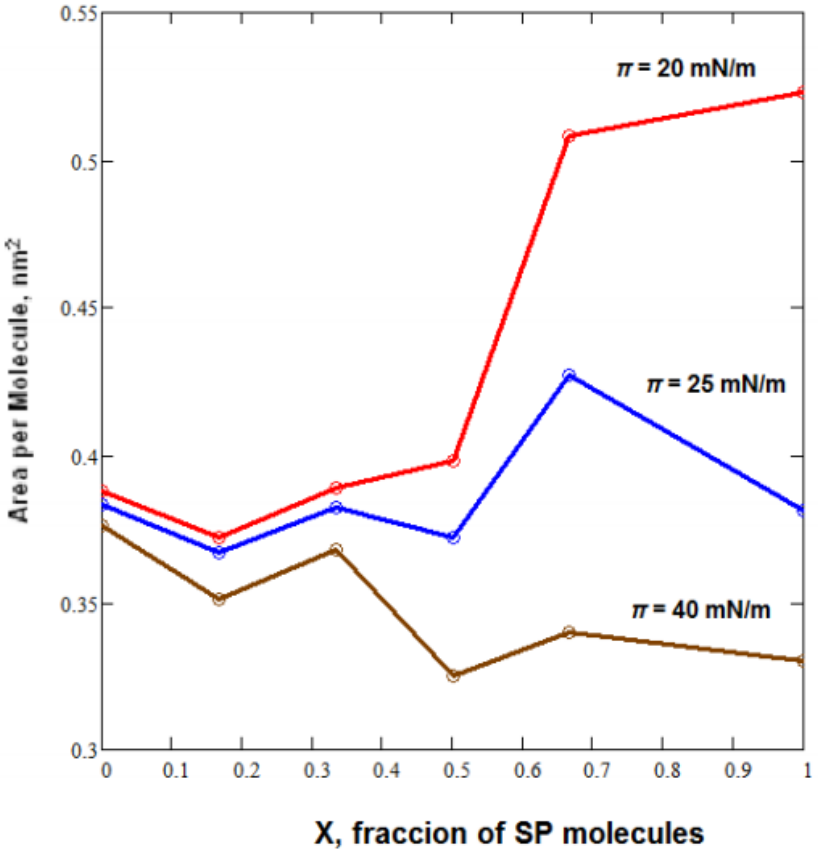

Figure 2A

3) GIXD of DMPA monolayer.

Figure 3A shows the contour plots of the corrected X-ray intensities as a function of the in-plane and out-of plane scattering vector Q_{xy} and Q_z components, for a pure DMPA monolayer at T = 21°C. The GIXD measurements were performed at different values of surface pressure. From left to right: 5, 10 and 30 mN/m.

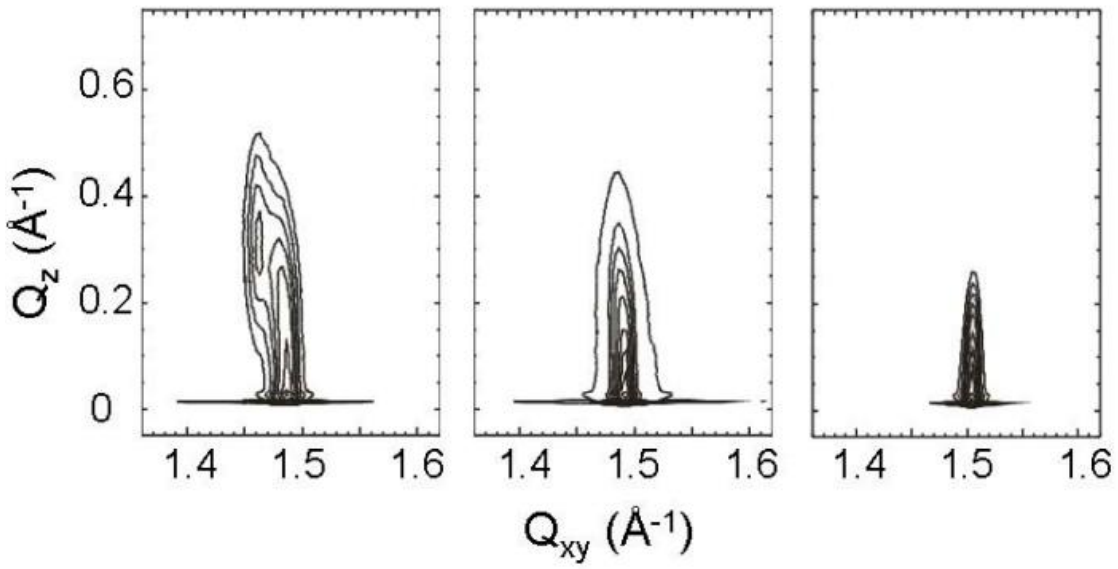

Figure 3A

Structural parameters of the DMPA monolayer are given in the next. Table: Primitive unit cell parameters, distortion values, tilt angle, projection of hydrocarbon chains in xy plane (A_{xy}) and cross sectional area of hydrocarbon chains (A_0) of a pure DMPA monolayer at T = 21°C.

π, mNm^{-1}	a, Å	$b = c$, Å	α, deg	$\beta = \gamma$, deg	distortion	tilt angle, deg	A_{xy}, Å^2	A_0, Å^2
2	4.862	4.966	121.4	119.3	0.0279	13.9	21.1	20.4
5	4.861	4.937	121.0	119.5	0.0207	12.6	20.9	20.4
10	4.902	4.873	119.6	120.2	0.0081	8.6	20.6	20.4
15	4.843	4.843	120	120	0	0	20.3	20.3
30	4.843	4.843	4.120	120	0	0	20.3	20.3

4.) *Reflection of an anisotropic thin film on isotropic substrate, and simulation of circles domain textures.*

The anisotropic thin film is assumed to be a biaxial material with complex refractive indices (N_{1x}, N_{1y}, N_{1z}). The reflection incidence angle, α_0, and transmission angle, α_2, of multiply reflected waves (Figure 4A) are constants and related by $n_0\sin(\alpha_0) = n_2\sin(\alpha_2)$, where $n_0 = 1$ (air) and $n_2 = 1.333$ (water) show the real refractive indices of the ambient and substrate, respectively.

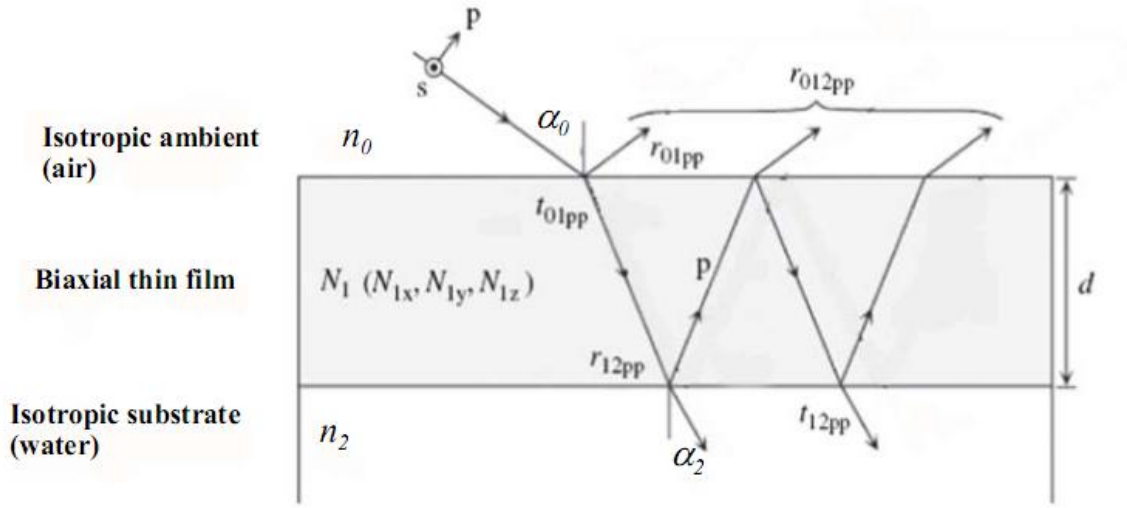

Figure 4A

In BAM microscopy, the incident light is p-polarized and when the analyzer is set to 0º, only the p component of the reflection is observed. In such a case, the light reflection at the ambient/film interface can be expressed as follows (Fujiwara, H. *Spectroscopic Ellipsometry. Principles and Applications*; John Wiley & Sons: Chichester, England, 2007):

$$r_{01pp} = \frac{N_x N_z \cos\alpha_0 - n_0 \left(N_z^2 - n_0^2 \sin\alpha_0\right)^{2^{1/2}}}{N_x N_z \cos\alpha_0 + n_0 \left(N_z^2 - n_0^2 \sin\alpha_0\right)^{2^{1/2}}}$$

$$r_{12pp} = \frac{n_2 \left(N_z^2 - n_2^2 \sin\alpha_2\right)^{2^{1/2}} - N_x N_z \cos\alpha_2}{n_2 \left(N_z^2 - n_2^2 \sin\alpha_2\right)^{2^{1/2}} + N_x N_z \cos\alpha_2}$$

The total reflection coefficients for p-polarizations

$$r_{012pp} = \frac{r_{01pp} + r_{12pp} \exp\ -i2\beta_p}{1 + r_{01pp} r_{12pp} \exp\ -i2\beta_p}$$

where

$$\beta_p = \frac{2\pi d}{\lambda} \frac{N_x}{N_z}\ N_z^2 - n_0^2 \sin\ \alpha_0\ ^{2\ 1/2}$$

being λ = 532 nm the wavelength of the laser beam and d the thickness of the biaxial thin film. The reflectances for p-polarized waves are obtained by

$$R_p = \left| r_{012pp} \right|^2$$

The complex refractive indices of anisotropic materials along the x, y, and z axes are given by $N_x = n_x - ik_x$, $N_y = n_y - ik_y$, and $N_z = n_z - ik_z$, respectively. As only the p-component of the reflection is analyzed, the N_y component does not affect to the final result. On the other hand, the absorption coefficients can be expressed by means of

$$k_x = k_0 \sin\ \theta\ ^2 \cos\ \phi\ ^2$$

$$k_z = k_0 \cos\ \theta\ ^2$$

where the angles θ and ϕ are those defined in Scheme 1 (see the manuscript) and α_0 = 53.15º (Brewster angle). From molecular models, we estimate that $d \approx 3.7$ nm, thickness of the film, included DMPA and SP molecules. The estimation was realized for a totally vertical configuration of the alkyl chains and a fixed angle θ = 50º between the hemicyanine group and the alkyl chain. Moreover, k_0 can be determined approximately from the reflection under normal incidence, by using the following relation (Pérez-Morales, M.; Pedrosa, J. M.; Muñoz, E.; Martín-Romero, M. T.; Möbius, D.; Camacho, L. *Thin Solid Films* **2005**, *488*, 247)

$$k = k_0 \cos\ \theta\ = \frac{\lambda \cdot \Delta R}{4\pi \cdot d \cdot \sqrt{R_i}}$$

where λ = 532 nm is the wavelength of the laser and $\Delta R = 7.9 \times 10^{-4}$ is the reflection at 532 nm from the reflection spectrum at high surface pressure (see Figure 5

of the manuscript). Thus, we can obtain $k_0 \approx 0.15$. To simplify the simulation, it is assumed for all cases: $n_y = n_z$, obtaining n_z from the Fresnel equations under normal incidence, as the value that reproduces the experimental ΔR at 532 nm, and thus $n_z \approx 1.6$. In such a way, the reflectivity depends exclusively on θ and ϕ.

Figure 5A shows the changes of reflectivity, R_p *vs* γ, for $\beta = 90º$ ($\phi = \gamma + \beta$, see Scheme 2 of the manuscript) at different θ values. We can observe that for $\theta \geq 45º$, the reflectivity is maximum at $\gamma = 90º$ and 270º, that is, for $\phi = 0º$ and 180º, while for $\theta \leq 40º$, the reflectivity is maximum at $\gamma = 0º$ and 180º, that is, for $\phi = 90º$ and 270º. The transition region between both behaviors comprises the θ values, ranged between 30º-60º.

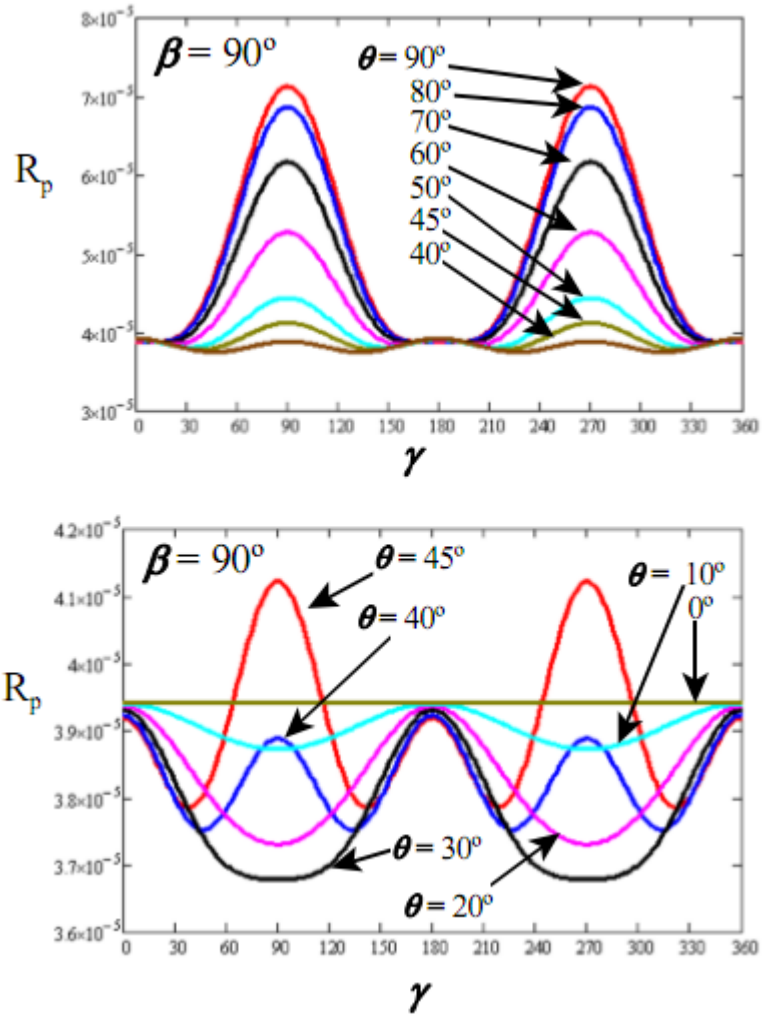

Figure 5A

Figure 6A displays the reflectivity obtained for $\theta = 50º$ and $\beta = 90º$.

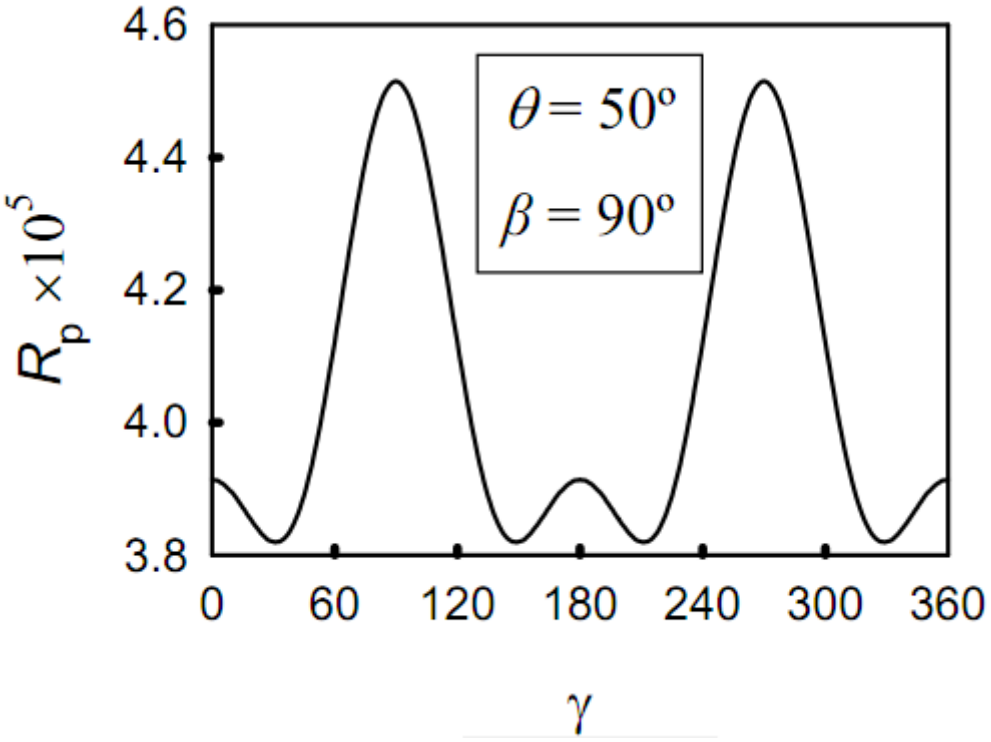

Figure 6A

For the simulation of BAM domains, the reflectivity is transformed in gray levels from 255 (white) to 0 (black). Figure 7A shows this transformation. Also, this figure displays the polar representation of the reflectivity (center) and domain simulation after the assignation of gray levels for each radial direction.

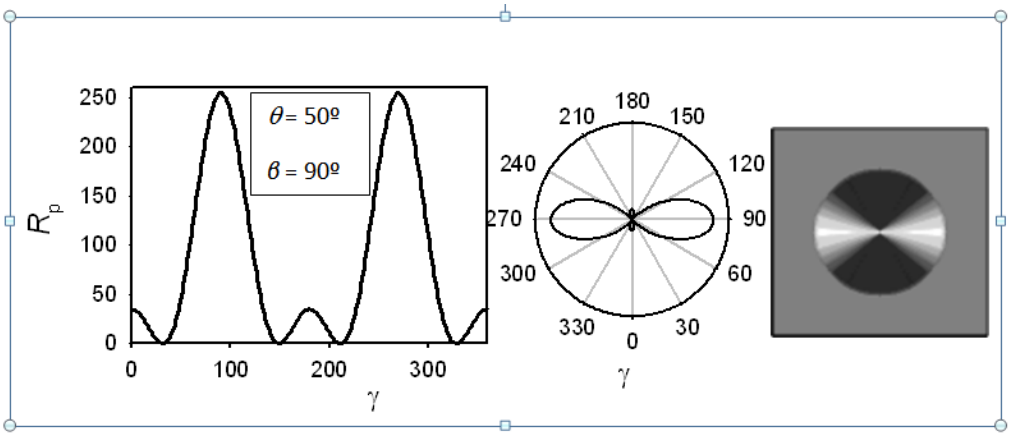

Figure 7A

The contrast and clarity of the image can be improved by means of the instrumental option of the BAM, the auto set gray level. When the auto set option is clicked, the gray level is rescaled by increasing the exposure time to the light in such a way that only the reflectivity under the threshold value can be discerned, being this threshold the new maximum reflectivy possible, that is, 255. If we take as reference the situation of Figure 7A, an increasing of the exposure time of 3/2 enhances the reflectivity in this amount just to the threshold of 255, as represented in Figure 8A, where the domain is also simulated.

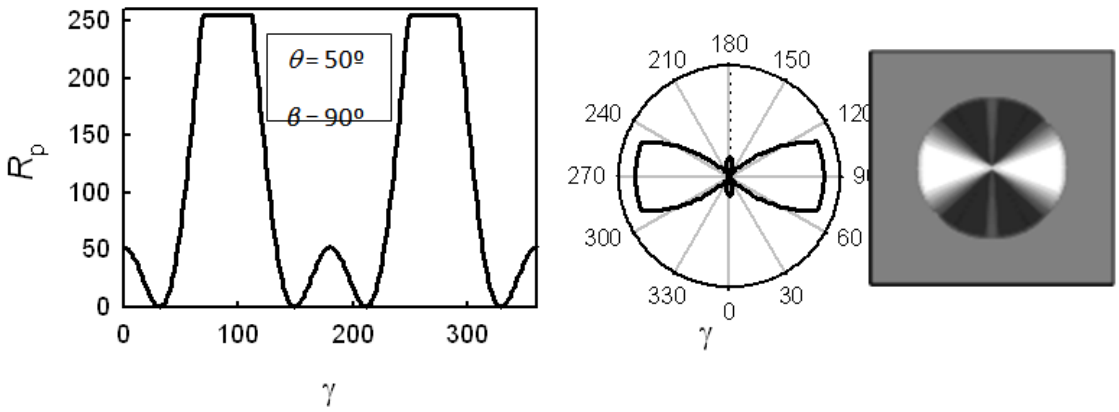

Figure 8A

These last conditions were utilized for the domain simulation, which is shown in Figure 6 of the manuscript.

In such a way, we can continue increasing the reflectivity. For example, Figure 9A shows the result after an exposure time of 2 with respect to the situation in Figure 7A.

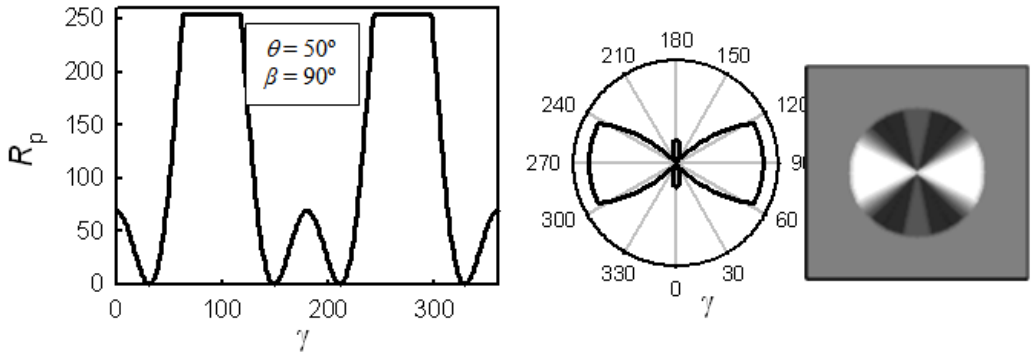

Figure 9A

5. *Reflection of an anisotropic thin film on isotropic substrate, under incidence angles different of the Brewster angle.*

Figure 10A shows the film reflectivity for $\alpha = 52°$ being $\beta = 90º$. As can be seen, the reflectivity is maximum for $\gamma = 90º$ and 270º provided that $\theta > 0º$. Therefore, the reflectivity will be maximum for $\phi = \gamma + \beta = 0º$ and 180º. This behavior is similar to that observed at the Brewster angle for $\theta > 60º$ (see Figure 5A).

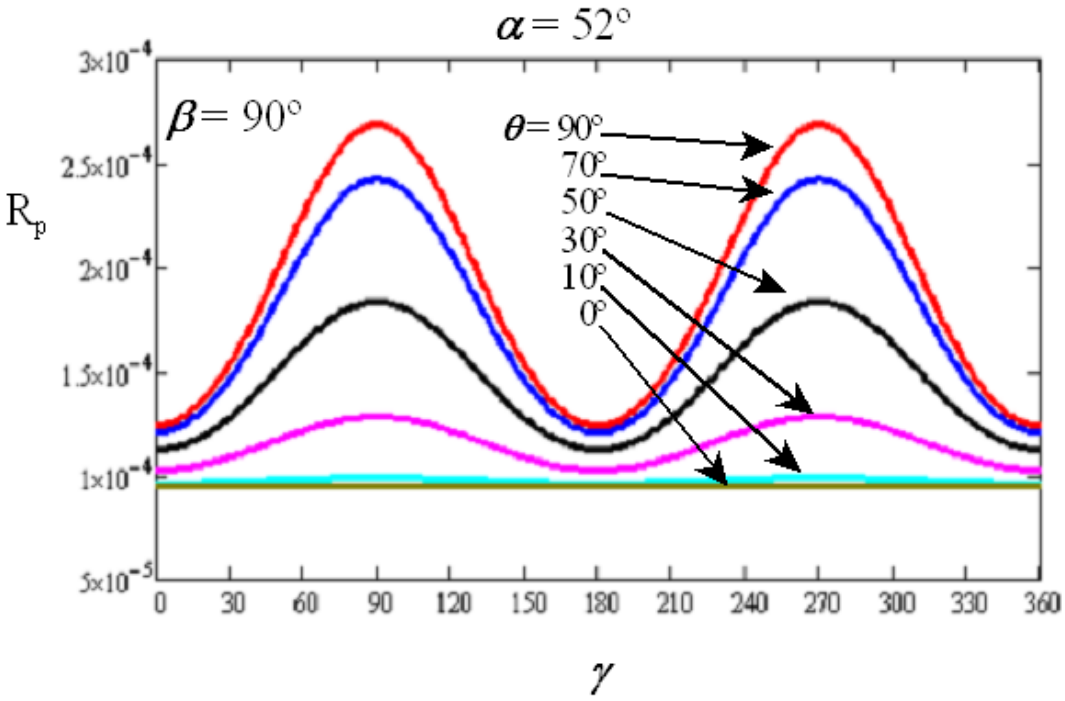

Figure 10A

Figure 11A displays the film reflectivity for $\alpha = 54°$ being $\beta = 90º$. As can be seen, the reflectivity is maximum for $\gamma = 0º$ and 180º provided that $\theta > 0º$. Therefore, the reflectivity will be maximum for $\phi = \gamma + \beta = 90º$ and 270º. This behavior is similar to that observed at the Brewster angle for $\theta < 30º$ (see Figure 5A).

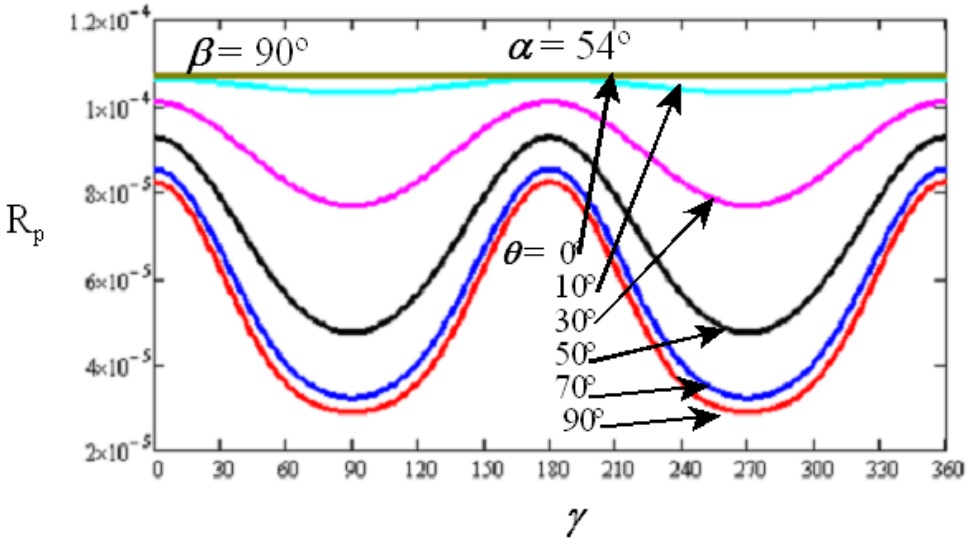

Figure 11A

Acknowledgment. We thank the Spanish CICYT for financial support of this research in the framework of Project CTQ2007-64474/BQU (FEDER A), and also thank the Junta de Andalucía (Consejería de Innovación, Ciencia y Empresa) for special financial support P06-FQM-01698 and P08-FQM-4011.

References

(1) Lehn, J.-M. *Angew. Chem., Int. Ed. Engl.* 1990, *29*, 1304.

(2) Vollhardt, D.; Liu, F.; Rudert, R. *Journal of Physical Chemistry B* 2005, *109*, 17635.

(3) Pérez-Morales, M.; Pedrosa, J. M.; Martín-Romero, M. T.; Möbius, D.; Camacho, L. *J. Phys. Chem. B* 2004, *108*, 4457.

(4) whitesides, G. M.; Grzybowski, B. *Science* 2002, *295*, 2418.

(5) Kaganer, V. M.; Möhwald, H.; Dutta, P. *Rev. Mod. Phys.* 1999, *71*, 779.

(6) Thirumoorthy, K.; Nandi, N.; Vollhardt, D. *Journal of Physical Chemistry B* 2005, *109*, 10820.

(7) Johann, R.; Vollhardt, D.; Möhwald, H. *Colloid Polym. Sci.* 2000, *278*, 104.

(8) Giner-Casares, J. J.; de Miguel, G.; Pérez-Morales, M.; Martín-Romero, M. T.; Muñoz, E.; Camacho, L. *J. Phys. Chem. C.* 2009, *113*, 5711.

(9) Young, M. C. J.; Jones, R.; Tredgold, R. H.; Lu, W. X.; Ali-Adib, Z.; Hodge, P.; Abbasi, F. *Thin Solid Films* 1989, *182*, 319.

(10) Kajikawa, K.; Anzai, T.; Shirota, K.; Takezoe, H.; Fukuda, A. *Thin Solid Films* 1992, *210*, 699.

(11) Schildkraut, J. S.; Penner, T. L.; Willand, C. S.; Ulman, A. *Opt. Lett.* 1988, *13*, 134.

(12) Carpenter, M. A.; Willand, C. S.; Penner, T. L.; Williams, D. J.; Mukamelt, S. *J. Phys. Chem* 1992, *96*, 2801.

(13) Turshatov, A. A.; Mobius, D.; Bossi, M. L.; Hell, S. W.; Vedernikov, A. I.; Lobova, N. A.; Gromov, S. P.; Alfimov, M. V.; Zaitsev, S. Y. *Langmuir* 2006, *22*, 1571.

(14) Turshatov, A. A.; Zaitsev, S. Y.; Sazonov, S. K.; Vedernikov, A. I.; Gromov, S. P.; Alfimovc, M. V.; Möbius, D. *Colloids and Surfaces A-Physicochemical and Engineering Aspects* 2008, *329*, 18.

(15) Fang, J. Y.; Uphaus, R. A.; Stroeve, P. *Thin Solid Films* 1994, *243*, 450.

(16) Orrit, M.; Möbius, D.; Lehmann, U.; Meyer, H. *J. Chem. Phys.* 1986, *85*, 4966.

(17) Kawai, T.; Umemura, J.; Takenaka, T. *Langmuir* 1989, *5*, 1378.

(18) Ahuja, R. C.; Möbius, D. *Langmuir* 1992, *8*, 1136.

(19) Pedrosa, J. M.; Martín-Romero, M. T.; Camacho, L.; Möbius, D. *J. Phys. Chem. B* 2002, *106*, 2583.

(20) Hönig, D.; Möbius, D. *J. Phys. Chem.* 1991, *95*, 4590.

(21) Hönig, D.; Overbeck, G. A.; Möbius, D. *Adv. Mater.* 1992, *4*, 419.

(22) Johann, R.; Vollhardt, D. *Mat. Sci. Eng. C* 1999, *8-9*, 35.

(23) Krasteva, N.; Vollhardt, D. *Colloids Surf. A: Physicochem. Eng. Aspects* 2000, *171*, 49.

(24) Weidemann, G.; Gehlert, U.; Vollhardt, D. *Langmuir* 1995, *11*, 864.

(25) Vollhardt, D.; Melzer, V. *J. Phys. Chem.* 1997, *101*, 3370.

(26) Kaganer, V. M.; Peterson, I. R.; Kenn, R. M.; Shih, M. C.; Durbin, M.; Dutta, P. *J. Chem. Phys.* 1995, *102*, 9412.

(27) Jacquemain, D.; Leveiller, F.; Weisbuch, S.; Lahav, M.; Leiserowitz, L.; Kjaer, K.; Als-Nielsen, J. *J. Am. Chem. Soc.* 1991, *113*, 7684.

(28) Als-Nielsen, J.; Jaquemain, D.; Kjaer, K.; Lahav, M.; Levellier, F.; Leiserowitz, L. *Phys. Rep.* 1994, *246*, 251.

(29) Kjaer, K. *Physica B* 1994, *198*, 100.

(30) Brezesinski, G.; Dietrich, A.; Struth, B.; Böhm, C.; Bouwman, W. G.; Kjaer, K.; Möhwald, H. *Chem. Phys. Lipids* 1995, *76*, 145.

(31) Overbeck, G. A.; Hönig, D.; Möbius, D. *Thin Solid Films* 1994, *242*, 213.

(32) Weidemann, G.; Vollhardt, D. *Langmuir* 1996, *12*, 5114.

(33) Weidemann, G.; Brezesinski, G.; Vollhardt, D.; Möhwald, H. *J. Phys. Chem. B* 1998, *102*, 1224.

(34) Ignés-Mullol, J.; Claret, J.; Reigada, R.; Sagués, F. *Phys. Report* 2007, *448*, 163.

(35) Nandi, N.; Vollhardt, D. *Chemical Reviews* 2003, *103*, 4033.

(36) Grüniger, H.; Möbius, D.; Meyer, H. *J. Chem. Phys.* 1983, *79*, 3701.

(37) Hall, R. A.; Thistlethwaite, P. J.; Grieser, F.; Kimizuka, N.; Kunitake, T. *Colloids and Surfaces A-Physicochemical and Engineering Aspects* 1995, *103*, 167.

(38) Vollhardt, D.; Fainerman, V. B. *Journal of Physical Chemistry B* 2002, *106*, 345.

(39) Lösche, M.; Duwe, H. P.; Möhwald, H. *J. Colloid Interface Sci.* 1988, *126*, 432.

(40) Pérez-Morales, M.; Pedrosa, J. M.; Muñoz, E.; Martín-Romero, M. T.; Möbius, D.; Camacho, L. *Thin Solid Films* 2005, *488*, 247.

(41) Martín, M. T.; Prieto, I.; Camacho, L.; Möbius, D. *Langmuir* 1996, *12*, 6554.

(42) Giner-Casares, J. J.; Perez-Morales, M.; Bolink, H.; Muñoz, E.; de Miguel, G.; Martin-Romero, M. T.; Camacho, L. *J. Colloid Interface Sci.* 2007, *315*, 278.

(43) Prieto, I.; Martín-Romero, M. T.; Camacho, L.; Möbius, D. *Langmuir* 1998, *14*, 4175.

(44) Ahuja, R. C.; Caruso, P. L.; Möbius, D.; Wildburg, G.; Ringsdorf, H.; Philp, D.; Preece, J. A.; Stoddart, J. F. *Langmuir* 1993, *9*, 1534.

(45) Giner-Casares, J. J.; Perez-Morales, M.; Bolink, H. J.; Munoz, E.; de Miguel, G.; Martin-Romero, M. T.; Camacho, L. *J. Colloid Interface Sci.* 2007, *315*, 278.

(46) Prieto, I.; Martín-Romero, M. T.; Camacho, L.; Mobius, D. *Langmuir* 1998, *14*, 4175.

(47) Overbeck, G. A.; Möbius, D. *J. Phys. Chem.* 1993, *97*, 7999.

(48) Overbeck, G. A.; Hönig, D.; Möbius, D. *Langmuir* 1993, *9*, 555.

(49) Leveiller, F.; Jacquemain, D.; Leiserowitz, L.; Kjaer, K.; Als-Nielsen, J. *J. Phys. Chem.* 1992, *96*, 10380.

(50) Song, Q.; Evans, C. E.; Bohn, P. W. *J. Phys. Chem* 1993, *97*, 13736.

(51) Lusk, A. L.; Bohn, P. W. *Langmuir* 2000, *16*, 9131.

(52) Lusk, A. L.; Bohn, P. W. *J. Phys. Chem. B* 2001, *105*, 462.

(53) Kuhn, H.; Försterling, H. D. *Principles of Physical Chemistry*; Jonh Wiley & Sons: New York, 1999.

(54) Kobayashi, T. *J-Aggregates* Wold Scientific: Singapore, 1996.

(55) Pope, M.; Swenberg, C. E. *Electronic Processes in Organic Crystals and Polymers*; Oxford Science Publications: New York, 1999.

(56) Hyperchem. 6th ed.; Htpercube, Inc.: Gainesville, FL, 1999.

(57) Fujiwara, H. *Spectroscopic Ellipsometry. Principles and Applications*; John Wiley & Sons: Chichester, England, 2007.

(58) Henon, S.; Meunier, J. *Chem. Phys.* 1993, *98*, 9148.

(59) Riviére, S.; Meunier, J. *Phys. Rev. Lett.* 1995, *74*, 2495.

(60) Mufazzal-Hossain, M.; Kato, T. *Langmuir* 2000, *16*, 10175.

(61) Yamamoto, T.; Manaka, T.; Iwamoto, M. *Eur. Phys. J. E* 2009, *29*, 1.

(62) Gaines, G. L. *Langmuir* 1991, *7*, 3054.

(63) Dynarowicz-Łatka, P.; Pérez-Morales, M.; Muñoz, E.; Broniatowski, M.; Martín-Romero, M. T.; Camacho, L. *J. Phys. Chem. B* 2006, *110*, 6095.

4.2 The Effect of the reduction of the available surface area on the hemicyanine aggregation in laterally organized Langmuir monolayers

This paper analyzes the effect of the reduction of the available area on the aggregation of an hemicyanine dye, 4-[4-dimethylamino)styryl]-1-docosylpyridinium bromide (SP) at the air-water interface. Mixed films of SP and stearic acid (SA) in molar ratio 1:1 have been studied, and compared with the previously studied films of SP and dimyristoyl-phosphatidic acid (DMPA) in molar ratio 1:1. With regard to the SP:DMPA films, the replacement of DMPA by SA involves reducing the area available for the hemicyanine aggregation, since the SA molecule provides only an alkyl chain to the set, whereas the DMPA molecule provides two alkyl chains to the set.

The SP:SA mixed films have been studied by Grazing Incidence X-ray Diffraction (GIXD), Brewster angle microscopy (BAM) and reflection spectroscopy at the air-water interface. Langmuir-Schaeffer films have been studied by UV-vis transmission spectroscopy. The SP:SA mixed monolayer forms star-shaped domains with inner textures, indicating anisotropy. Circular domains were observed for the SP:DMPA system. GIXD experiments relate the star-shaped domains with an orthorhombic phase, as for circular domains observed for the SP:DMPA system. The results obtained by reflection and transmission polarized spectroscopy for the SP:SA system, showed the splitting of the absorption band of the aggregate. The splitting has been related with a twisting in the hemicyanine groups.

The reduction on the available area accounts for the aggregation of the hemicyanine group. The domain shape at the mesoscopic level was mainly originated from the interactions between the polar groups and the reduced surface area. The interactions between the alkyl chains are essential to maintain the crystalline structure, although these interactions did not play the main role in the final shape of the domain.

Paper published in *J. Phys. Chem. C*, **115** (2011) 9059-9067

4.2.1 Introduction

In Langmuir monolayers, the repulsive dipolar interaction of the molecules within a domain favors a large boundary-to-area ratio, by which the electrostatic repulsion energy is reduced.[1] In this case, the domain morphology does not entirely correspond to the molecular lattice structure. To design well-defined structures, in which the lateral organization is controlled, it is required to compensate the repulsion energy between dipoles. In order to achieve this compensation, the polar heads of lipids should be connected, either through hydrogen bonding,[2] or through the self-aggregation of dyes.[3-4] Recently, we have used the latter strategy to study mixed films containing dimyristoyl-phosphatidic acid (DMPA) and an amphiphilic hemicyanine dye (SP) in a molar ratio 1:1.[4]

The key to apply this procedure is the adequate balance between the sizes of the hydrophobic and hydrophilic groups. The DMPA plays a triplet role in the SP:DMPA = 1:1 films. First, the DMPA molecule provides two aliphatic chains to the set, so the minimum perpendicular section of the 1:1 mixture would be around 0.6 nm^2 per SP molecule. Second, the anionic DMPA offsets the positive charge of the SP molecule. Finally, the alkyl chains of the DMPA are shorter than those of the SP, so that the DMPA polar group does not avoid the hemicyanine aggregation by the dye molecular tilt. Thus, if a_c is the interfacial area occupied by the hydrophobic group when the alkyl chains are fully extended ($a_c \approx 0.6$ nm^2 in the SP:DMPA = 1:1 system), and a_0 is the minimum interfacial area occupied by the head group ($a_0 \approx 0.33$ nm^2 for the hemicyanine group), the dyes to be selected should obey $a_c \geq a_0$. In this way, the domain structure depends on the ability of the dye to fill the available area excess (a_c - a_0).[4] BAM images show a well-organized structure (circular domains) of micrometre size, which presents inner anisotropy. By Grazing Incidence X-ray Diffraction (GIXD), the formation of two different crystalline phases, orthorrombic and Overbeck, was observed. The orthorrombic phase showed no tilting of hydrocarbon chains, whereas in the Overbeck phase the tilting value was ca. 17° for the complete range of surface pressure studied. Moreover, information on the organization of the polar heads was obtained by using reflection spectroscopy and simulating the domains observed by

In this paper, mixed films containing SP and stearic acid (SA) in a molar ratio 1:1 (See Scheme 1) have been studied. With regard to the previous study of the SP: DMPA = 1:1 films, the replacement of DMPA by SA involves the reduction of the

available area for the hemicyanine aggregation, since each SA provides only an alkyl chain to the set. Therefore, the minimum perpendicular section of the 1:1 mixture would be ca. 0.4 nm^2 per SP molecule. The SA molecule, as in the case of the DMPA molecule, can offset the positive charge of SP, as it is negatively charged at neutral pH. The alkyl chain of SA is also shorter than that of SP. These features do not avoid the hemicyanine aggregation by the dye molecular tilt.

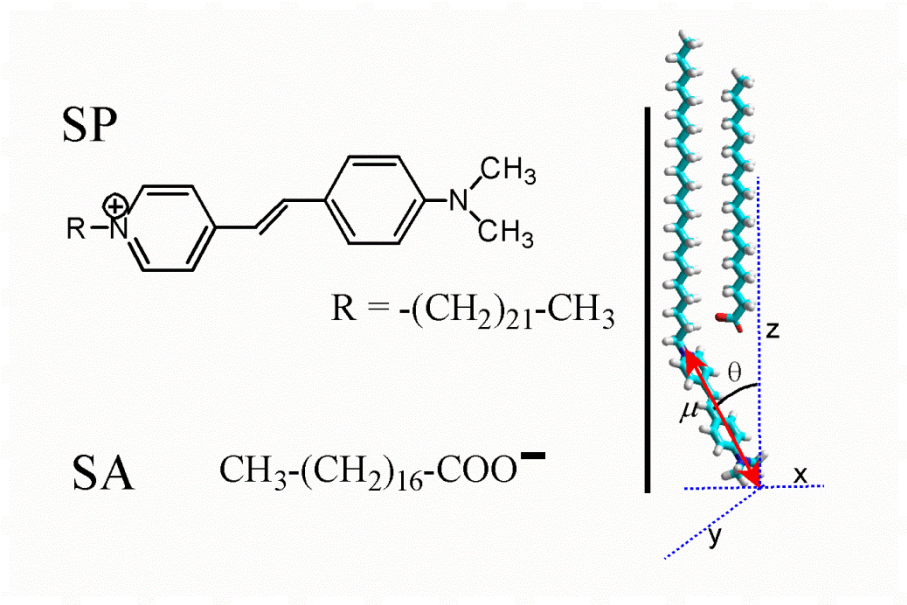

Scheme1: Molecular structures of hemicyanine, SP, and Stearic acid, SA. Graphical definition of the transition dipolar moment, μ, the polar tilt angle, θ, of the SP molecules in presence of the SA molecule (the interface plane coincides with *x*-*y* plane).

The present study attempts to analyze the effect of the reduction of the available space in both the structure of domains formed and the hemicyanine aggregation. Information on the possible changes in the packing of the alkyl chains is also analyzed. Thus, the molecular organization and the domain morphology of SP:SA = 1:1 mixed films have been studied by using Grazing Incidence X-ray Diffraction (GIXD), Brewster angle microscopy (BAM) and reflection spectroscopy at the air-water interface, as well as transmission spectroscopy of the monolayers transferred onto quartz.

The BAM images of the SP:SA = 1:1 system show the formation of star-shaped domains, with different geometry when compared to those observed for the SP:DMPA system. Moreover, the GIXD experiment permitted us to relate the star-shaped domains

with an untilted conformation of the hydrocarbon chains, which adopt a solid condensed state along the whole isotherm. Also, the closer approach between the hemicyanine groups led to a surprising phenomenon barely perceptible in the SP:DMPA system: the splitting of the absorption band of the aggregate. This splitting of the band has been related with a molecular distribution in which the hemicyanine groups are not organized parallel, but slightly twisted by each other. Therefore, the corresponding transition dipoles are added, resulting in two components or excited states with perpendicular orientation and optically allowed.[5-7]

4.2.2 Experimental

Materials. Hemicyanine dye, 4-[4-Dimethylamino)styryl]-1-docosylpyridinium bromide (SP) and stearic acid (SA) were purchased from Sigma-Aldrich and used as received. Their molecular structures are depicted in Scheme 1. A mixture of chloroform:methanol, ratio 3:1 (v/v), was used as spreading solvent for solving both components. The pure solvents were obtained without purification from Aldrich (Germany). Ultrapure water, produced by a Millipore Milli-Q unit, pre-treated by a Millipore reverse osmosis system (> 18.2 MΩ cm), was used as a subphase. The subphase pH was 5.7 and the temperature was externally controlled.

Methods. Two different models of Nima troughs (Nima Technology, Coventry, England) were used in this work, both provided with a Wilhelmy type dynamometric system using a strip of filter paper: a NIMA 611D with one moving barrier for the measurement of the reflection spectra, and a NIMA 601, equipped with two symmetrical barriers to record BAM images. The monolayers were compressed at a speed of ~ 0.1nm nm^2 min^{-1} $molecule^{-1}$.

UV–visible reflection spectra at normal incidence as the difference in reflectivity (ΔR) of the dye film-covered water surface and the bare surface[8] were obtained with a Nanofilm Surface Analysis Spectrometer (Ref SPEC^2, supplied by Accurion GmbH, Göttingen, Germany). The reflection spectra were normalized to the same surface density of hemicyanine by multiplying ΔR by the surface area, i.e., $\Delta R_{norm} = \Delta R \bullet A$, where A (nm^2/SP molecule) is taken from the surface pressure-area (π-A) isotherms. UV-visible electronic absorption spectra of the films were measured locating the substrate directly in the light path on a Cary 100 Bio UV-visible spectrophotometer.

Images of the film morphology were obtained by Brewster angle microscopy (BAM) with a I-Elli2000 (Accurion GmbH) using a Nd:YAG diode laser with wavelength 532 nm and 50mW, which can be recorded with a lateral resolution of 2 μm. The image processing procedure included a geometrical correction of the image, as well as a filtering operation to reduce interference fringes and noise. The microscope and the film balance were located on a table with vibration isolation (antivibration system MOD-2 S, Accurion, Göttingen, Germany) in a large class 100 clean room.

The monolayers were transferred onto quartz substrates, cleaned in successive steps with an alkaline detergent, isopropanol, and ethanol and then rinsed with ultrapure water. The monolayers were transferred at constant surface pressure by the Langmuir-Schaeffer technique, i.e., by horizontal touching of the substrate and the interface covered with the mixed film. The multilayers were assembled by sequential monolayer transfer. The transfer ratio was close to unity for all transfer processes.

Grazing Incidence X-ray Diffraction (GIXD) measurements of the monolayer were performed at 21°C at the BW1 beamline, HASYLAB, DESY (Hamburg, Germany). A Langmuir film balance equipped with a single movable barrier and a Wilhelmy plate for monitoring the lateral pressure was placed in a hermetically closed container filled with helium. At BW1, a monochromatic synchrotron X-ray beam (λ=1.304 Å) was adjusted to strike the helium/water interface at a grazing incidence angle α_i=0.85α_c (α_c=0.13°) and illuminated roughly 2x50 mm^2 of the surface. During the measurements, the trough was laterally moved to avoid any sample damage by the strong X-ray beam. A linear position-sensitive detector (PSD, MYTHEN, Switzerland) was rotated to scan the in-plane Q_{xy} component values of the scattering vector. The vertical channels of the PSD measured the out-of-plane Q_z component of the scattering vector between 0 and 0.8 Å^{-1}. The diffraction data consisted of Bragg peaks at diagnostic Q_{xy} values. The accumulated position-resolved counts were corrected for polarization, effective area, and Lorentz factor. Model peaks taken as Lorentzian in the in-plane direction and as Gaussian in the out-of-plane direction were least-square fitted to the measured intensities. The diffracted intensity normal to the interface was integrated over the Q_{xy} window of the diffraction peak to calculate the corresponding Bragg rod. Experimental details are described in the literature.[9-14]

Infrared Reflection Absorption Spectroscopy (IRRAS) spectra were recorded on an IFS 66 FT-IR spectrometer (Bruker, Germany) equipped with a liquid nitrogen-

cooled MCT (mercury cadmium telluride) detector. The spectrometer was coupled to a Langmuir-film balance, placed in a sealed container, to guarantee a constant-vapor atmosphere (the external XA-511 air/water reflection unit). In a typical experiment, one hour was given to saturation of the atmosphere with water vapor. Within the container, wet paper filter was place to ensure the saturation of water vapor. The IR beam was conducted out of the spectrometer and focused onto the water surface of the Langmuir trough. A computer controlled rotating KRS-5 wire-grid polarizer (thallium bromide and iodide mixed crystal) was used to generate parallel (p) and perpendicular (s) polarized light. The angle of incidence was set to 40° with respect to the surface normal. Measurements were performed using a trough with two connected compartments and a trough shuttle system.[15-16] One compartment contained the monolayer system under investigation (sample), whereas the other (reference) was filled with the pure subphase. The single-beam reflectance spectrum of the reference trough surface was used as the background signal to the single-beam reflectance spectrum of the sample to calculate the reflection absorption spectrum as $(-\log(R/R_0))$. IR spectra were collected at 8 cm^{-1} resolution using 200 scans for s-polarized light and 400 scans for p-polarized light.

4.2.3 Results and Discussion

4.2.3.1. Surface Pressure-Area Isotherms and Brewster Angle Microscopy (BAM)

Monolayers of SP:SA = 1:1 have been formed at the air−water interface by the co-spreading method. Figure 1 (top-left) shows the π–A isotherms at 17, 24 and 30ºC for the SP:SA = 1:1 monolayer. For T ≥ 24ºC and area values close to 1.8 nm^2, a phase change is observed. All the isotherms converged at high surface pressures reaching at a surface pressure of 35 mN/m, surface areas of 0.37 nm^2, 0.4 nm^2 and 0.44 nm^2, for T = 17, 24 and 30 ºC, respectively. These surface area values are consistent with the presence of two alkyl chains per hemicyanine group.

Simultaneously to the isotherm recording, the morphology of the mixed monolayer at the air−water interface was directly observed by BAM. At T = 17 ºC and very low surface pressure (Figure 1A), the monolayer appeared to be composed of a mixture of gas phase and bright domains. The appearance of domains indicates a strong

aggregation of the hemicyanine group. When the surface area decreased, the monolayer appears homogenous, indicating the complete miscibility of the components. After the isotherm take-off, small domains could be observed (Figure 1B). The morphology of these small domains could not be clearly observed, although they showed different textures with brighter and darker regions than the surrounding background. At high surface pressure, these structures occupied the entire observed region.

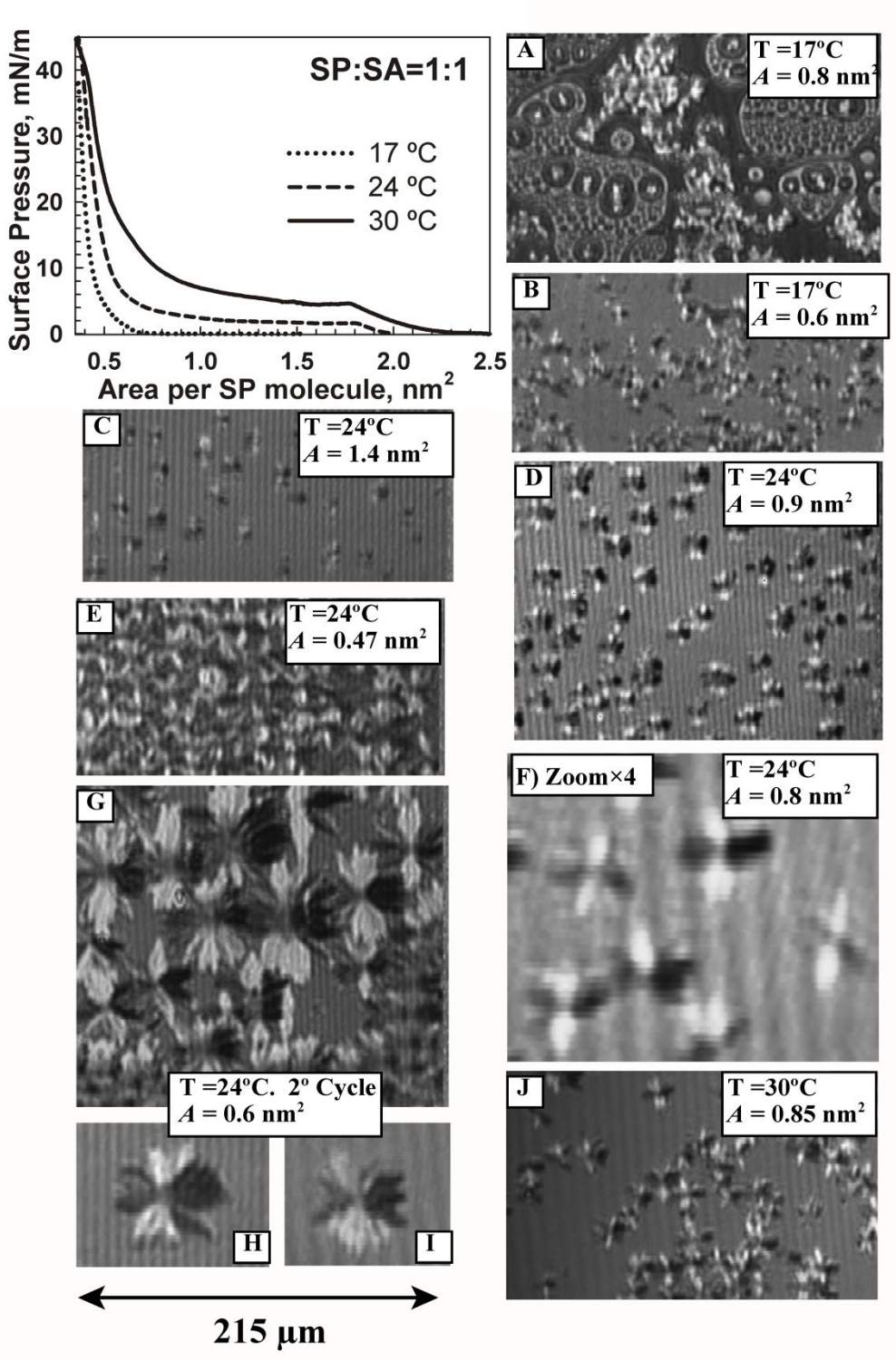

Figure 1: Surface pressure–area (π–A) isotherms of the mixed SP:SA monolayer in a molar ratio 1:1 at T = 17ºC, 24ºC and 30ºC (top-left). A)–J) BAM images of the mixed SP:SA = 1:1 monolayer under different surface pressures and temperatures at the air–water interface. Image size: 215 µm width.

At T = 24ºC and for areas slightly above the phase change, the monolayer is homogenous. For areas below the phase change, small domains similar to those described in Figure 1B appeared. When the area was further reduced, the domains grew in size (Figures 1C and 1D). At high surface pressure, the domains eventually covered the entire observed region (Figure 1E). Figure 1F shows the enlargement (zoom) of a BAM image in the early stages of the domain growth. The domains appeared as 4-pointed stars. The number of points increased as the surface pressure was increased, and these points are not symmetrically distributed in space. The star-shaped domains have inner textures, with different brightness. The vertical points of the star are brighter than the environment, while the lateral points of the star are darker. In a BAM experiment, p-polarized light reaches the air-water interface with an incidence angle of 53.15º, the Brewster angle for air/water interface. Usually, the different BAM textures are observed due to changes of the refractive index resulting from differences in thickness, density and/or molecular orientation between the different regions of the film. However, in our case the SP molecules absorb at the wavelength of the laser incident (532 nm, see Figure 4 below). This phenomenon was the main cause of the high reflectivity observed in the monolayer.[3-4] As in the SP:DMPA system, hemicyanine aggregation induced the formation of domains. The inner texture is an indication of an ordered aggregation of these groups (anisotropy). In other words, the different textures observed in the domains can be related to the 2D order of the polar groups of the monolayer.[4]

The BAM images shown in Figures 1C-1F correspond to the π–A isotherm at 24°C, during the first compression cycle. When the monolayer was decompressed and a second compression process was performed, some hysteresis at low surface pressure happened. Both isotherms were coincident at high surface pressure. The hysteresis at low surface pressure was related to the fact that the domains did not disappear completely when the monolayer was expanded. However, a significant phenomenon was observed during the second compression process: the domains growth is larger in the first cycle (see Figure 1G, 1H and 1I). Note that these domains coexisted with irregular structures (images not shown). In these large domains, the properties previously described appear. The domains showed anisotropy, and the variation of the polarization of the BAM laser changed their texture. At T = 30 ºC, the features observed in the domains were similar, but slightly larger than those recorded at 24 ºC, as shown in Figure 1J.

Additionally, experiments for the SP:SA = 1:1 monolayer by using a buffered subphase (acetic acid /acetate 10^{-5} M) were carried out. Isotherms and BAM images did not show any difference from those obtained by using pure water as a subphase.

The morphology of the domains observed in the presence of SA was different from those in the presence of DMPA. Thus, circular domains with bright horizontal regions and dark vertical regions have been observed for the SP:DMPA = 1:1 film.[4] Furthermore, a modification of the temperature, leads to a growth of branches grew from circular domains, whose brightness depended on the growth direction. In the presence of SA, there were star-shaped domains, indicating a different organization, at least with respect to the polar groups.

4.2.3.2. Synchrotron Grazing Incidence X-ray Diffraction (GIXD)

Grazing Incidence X-ray Diffraction (GIXD) measurements have been performed in order to obtain quantitative information about the 2D symmetry of Langmuir monolayers. GIXD is sensitive only to the condensed parts of the monolayer, giving an ordered structure that can result in X-ray diffraction. The liquid expanded phase contributes only to the background scattering. Structural changes along compression occurring for the SP/SA mixed monolayer have been monitored.

The crystalline phases of stearic acid have been described along monolayer compression as L_2-Ov-LS.[17-18] The transition surface pressure into the non-tilted LS phase is 24.6 mN/m. Figure 2 shows the corrected X-ray intensities as a function of the scattering vector components Q_{xy} and Q_z for the mixed SA:SP monolayer in a molar ratio 1:1 at T = 21°C. The X-ray diffraction patterns have been recorded at three different surface pressures: 3, 10 and 25 mN/m. In the investigated interval of surface pressures, there are two clear and well-defined Bragg peaks. Diffraction peaks and rods values are depicted in Table 1, with their full-width at half-maximum (fwhm) values. Quantitative information on the unit cell parameters, tilt angle and cross sectional area can be found in Table 2. The observed nearest neighbor (NN) tilt direction coupled with a next-nearest neighbor (NNN) unit-cell distortion direction is described as a L_{2h}.[14] Therefore, the mixed monolayer SP:SA adopts a L_{2h} phase at low values of surface pressure. Above the phase transition surface pressure of ca. 5 mN/m, the mixed monolayer SP:SA exhibits a non-tilted condensed phase with an orthorhombic unit-cell.

Calculating the orthorhombic unit-cell parameters a and b shows that the packing mode is pseudo-herringbone. The unit-cell distortion is in the NNN direction. To the best of our knowledge, no untilted phase with NNN distortion has been previously described.[14] Therefore, the known nomenclature cannot be used.

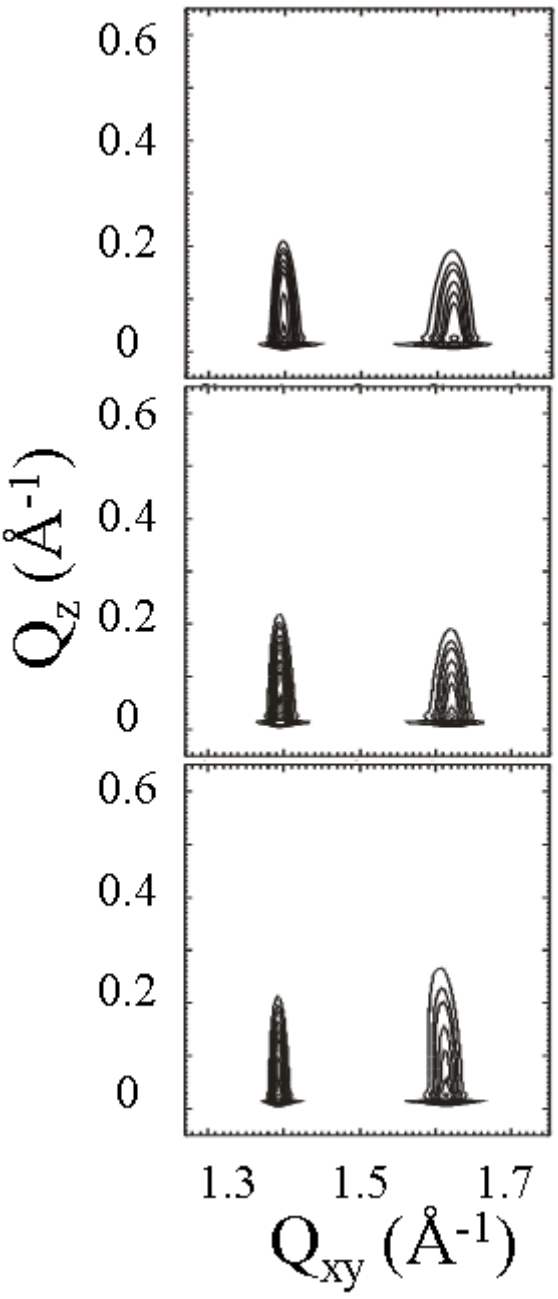

Figure 2: Contour plots of the corrected X-ray intensities as a function of the in-plane and out-of plane scattering vector Q_{xy} and Q_z components for the mixed SA:SP monolayer in a molar ratio 1:1 at T = 21°C. The GIXD measurements were performed at different values of surface pressure. From bottom to top: 3, 10 and 25 mN/m.

Table 1: In-plane Q_{xy} and out-of-plane Q_z components of the scattering vector of the mixed SA:SP monolayer in a molar ratio 1:1 at $T = 21°C$. The Full-Width at Half-Maximum (fwhm) of the peaks is given in parentheses.

Table 1				
π, mNm^{-1}	Q_{xy}, Å^{-1}	Q_z, Å^{-1}	Q_{xy}, Å^{-1}	Q_{z1}, Å^{-1}
3	1.393 (0.011)	0 (0.2)	1.612 (0.026)	0.080 (0.23)
10	1.395 (0.012)	0 (0.197)	1.620 (0.026)	0 (0.22)
25	1.398 (0.013)	0 (0.190)	1.620 (0.027)	0 (0.22)

Table 2: Primitive unit cell parameters, distortion values, tilt angle, projection of hydrocarbon chains in xy plane (A_{xy}) and cross sectional area of hydrocarbon chains (A_0) of the mixed SA:SP Monolayer in a Molar ratio 1:1 at $T = 21°C$.

Table 2								
π, mNm^{-1}	a, Å	$b = c$, Å	α, deg	$\beta = \gamma$, deg	distortion	tilt angle, deg	A_{xy}, Å^2	A_0, Å^2
3	4.322	5.001	128.8	115.6	0.1844039	3.1	19.5	19.5
10	4.297	4.990	129.0	115.5	0.1885730	0	19.4	19.4
25	4.299	4.982	128.9	115.6	0.1860272	0	19.3	19.3

The hydrocarbon chain lengths of SP (C22) and SA (C18) are quite similar. Enough space underneath the SA headgroup is expected to accommodate the bulky headgroup of SP. Therefore, a well-packed, highly crystalline structure of the mixed monolayer is obtained. However, unlike other mixed monolayers composed of two similar surfactants, the headgroups are very different. The arrangement of the bulky SP headgroup might induce the NNN distortion of the lattice.

The tight packing of the monolayer has also been confirmed by IRRAS. Figure 3 shows the IRRAS spectra of the mixed monolayer at 3, 10 and 25 mN/m. For the complete range of surface pressures, similar results on hydrocarbon chains conformation have been obtained. The asymmetric stretching mode of methylene, $\nu_{as}(CH_2)$, shows values of 2915.8, 2915.9 and 2915.9 cm^{-1} for 3, 10 and 25 mN/m, respectively. The symmetric stretching mode of methylene $\nu_s(CH_2)$, shows values of 2849.7, 2849.8 and 2849.9 cm^{-1} for 3, 10 and 25 mN/m, respectively. Therefore, the low wave numbers in the region of the CH_2 stretching vibrations show that the hydrocarbon chains of both SP and SA are tightly packed in the condensed state along the complete isotherm. The most prominent band in the spectra is that at 3580 cm^{-1} that arises from the OH stretch of water and is a characteristic feature of IRRA spectra (see the Supporting Information). The water OH stretching vibration present in the reference signal (R_0) is reduced in the reflectivity signal from the monolayer-covered surface (R)

because the lipid layer replaces a water layer and masks partially the OH stretching vibration. The result is a strong positive band at 3580 cm^{-1} that is related to the monolayer's effective thickness. As expected from the GIXD results showing small or no tilt angles, the intensity of this band does not change remarkably because the layer thickness and the packing density are mostly constant in the investigated pressure range. Surprisingly, the splitting of the CH_2 deformation band, expected from the GIXD results because of the packing in an orthorhombic unit cell, is not observed. Instead, a single band at 1472 cm^{-1} can be seen at all pressures (see the Supporting Information). The band at ca. 1166 cm^{-1} is assigned to the C-O stretch vibration mode of the carboxylic group of stearic acid.[19]

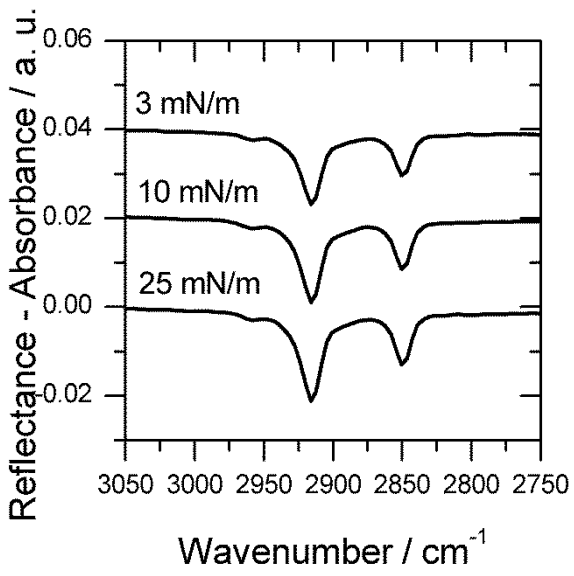

Figure 3: Selected region of IRRA spectra from the mixed SA:SP monolayer in a molar ratio 1:1 at T = 21°C, at different surface pressures. Spectra have been collected at an incidence angle of 40° by using p-polarized light. For clarity the spectra are scaled with an offset of cumulative 0.02 a. u.

4.2.3.3. Reflection Spectroscopy of the mixed SP:SA monolayers

The normalized reflection spectra, ΔR_{norm}, of SP:SA= 1:1 monolayers on water subphase at different surface areas (see isotherm of Figure 1) are shown in Figure 4.

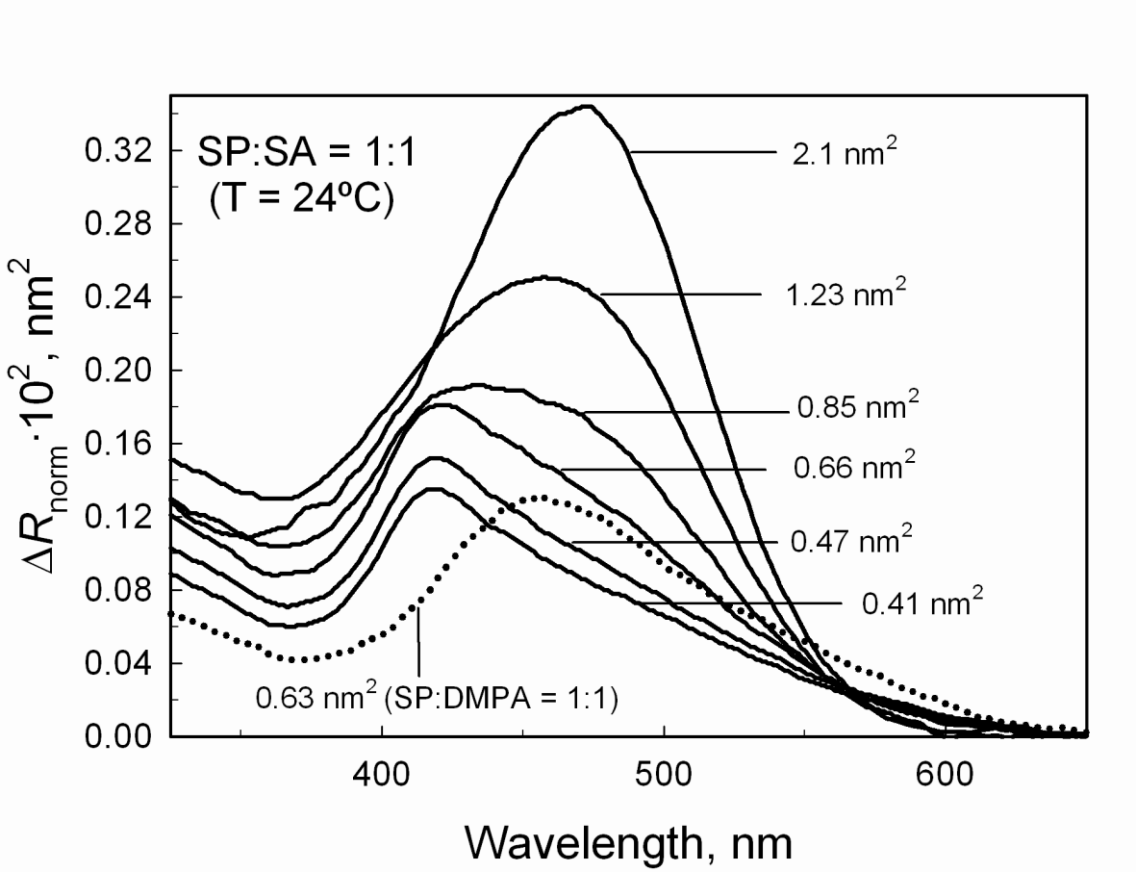

Figure 4: Normalized reflection spectra, ΔR_{norm}, of the mixed SP:SA = 1:1 monolayers (solid lines). The surface areas are indicated in the Figure. For comparison, the normalized reflection spectrum of the mixed SP:DMPA = 1:1 monolayer at high surface pressure (0.63 nm^2 per SP molecule) is also shown (dotted line).

For low values of absorption, the reflection ΔR has been shown to be proportional to the surface concentration of the dye.[8,20-22] In this case, the corresponding product $\Delta R \times A = \Delta R_{norm}$ could be expressed by means[4]

$$\Delta R_{norm} = \Delta R \times A = 5.407 \times 10^{-8} \, f_{orient} \, \varepsilon \qquad (1)$$

where the extinction coefficient ε is given as L mol^{-1} cm^{-1}, f_{orient} is a numerical factor that takes into account the different average orientation of the square transition moment of the dye in solution as compared to the monolayer at the air–water interface, A is the surface area per dye molecule and ΔR_{norm} is expressed in nm^2.

At low surface pressures, the spectra presented a low-energy band at 475 nm, corresponding to the π-π* transition of the chromophore in trans configuration.[23-24] As

the surface pressure increased, two phenomena were observed in the reflection band:

1) The maximum wavelength of the band was shifted to shorter wavelengths, from 475 nm to 410 nm (in the case of the SP:DMPA system, the band shifted from 475 nm to 459 nm). This shift is attributed to the formation of H aggregates of the SP chromophores.[23-26] For comparison, the Figure 4 shows the reflection spectrum of the SP:DMPA = 1:1 mixed monolayer, taken at a surface area close to the collapse of the film. In the vicinity of the collapse, the area per hemicyanine group was lower in the SP:SA film (~ 0.4 nm^2) than in the SP:DMPA film (~ 0.6 nm^2). Therefore, the hemicyanine groups seemed to be closer in the SP:SA system, which led to a greater interaction between them.

2) ΔR_{norm} decreased under compression, which could be related to the decreasing of the polar tilt angle of the chromophores. The polar angle θ is defined as the angle between the SP transition moment and the normal to the air–water interface (see Scheme 1). As demonstrated previously for the SP:DMPA system,[4] the integration of the absorption band gives the apparent oscillator strength. The value of the polar angle θ, can be calculated.[4] Using this procedure, the polar tilt angle of the hemicyanine group for the SP:SA = 1:1 film have been determined. When the surface area was close to the collapse, the obtained polar angle is ~ 50° (data not shown). This value is approximately coincident with the θ angle obtained for the hemicyanine group in the SP:DMPA system. The agreement between these values can be pointed out qualitatively by collating the spectra obtained for the SP:SA and SP:DMPA films at 0.41 nm^2 and 0.63 nm^2, respectively (see Figure 4). A simple visual comparison of these spectra allows to observe that the integration of the visible band should provide similar areas for both systems and, therefore, similar polar angles. However, similar values of the tilt polar angle of the hemicyanine group in both cases is contradictory, since the areas occupied by this group are quite different in the SP:SA and SP:DMPA films. In fact, the tilt angle of this group can be determined by geometric models, obtaining ~ 35º when the projected area of the hemicyanine group over the interface was ~ 0.4 nm^2. This estimation drastically contradicts the angle calculated from the integration of the band.

The method used to determine the tilt angle of the chromophore, which is based on the integration of the band, provides only an average angle.[4,22] This average angle can be directly related to the chromophore tilt angle, provided that two conditions are fulfilled: First, there must be only one type of aggregate, with all molecules equally

oriented, which can be often achieved at the air-water interface. Second, the band should be simple, i.e., caused by a single transition or at least all transitions of the band with their transition dipoles oriented in the same direction. In case of failure to comply with these requirements, the angle obtained by the above method would be only an average value of complex interpretation.

4.1.3.4. Transmision spectra of the mixed SP:SA LS films

Langmuir monolayers of SP:SA = 1:1 have been transferred onto quartz supports at different constant surface pressures, π_{Trans}, using the LS method. Transmission spectra of the LS films have been obtained under normal and 45º incidence angle, with non-polarized, s, and p-polarized light. Figure 5 shows the spectra for the first 7 monolayers transferred at π_{Trans} = 30 mN/m, recorded under normal incidence.

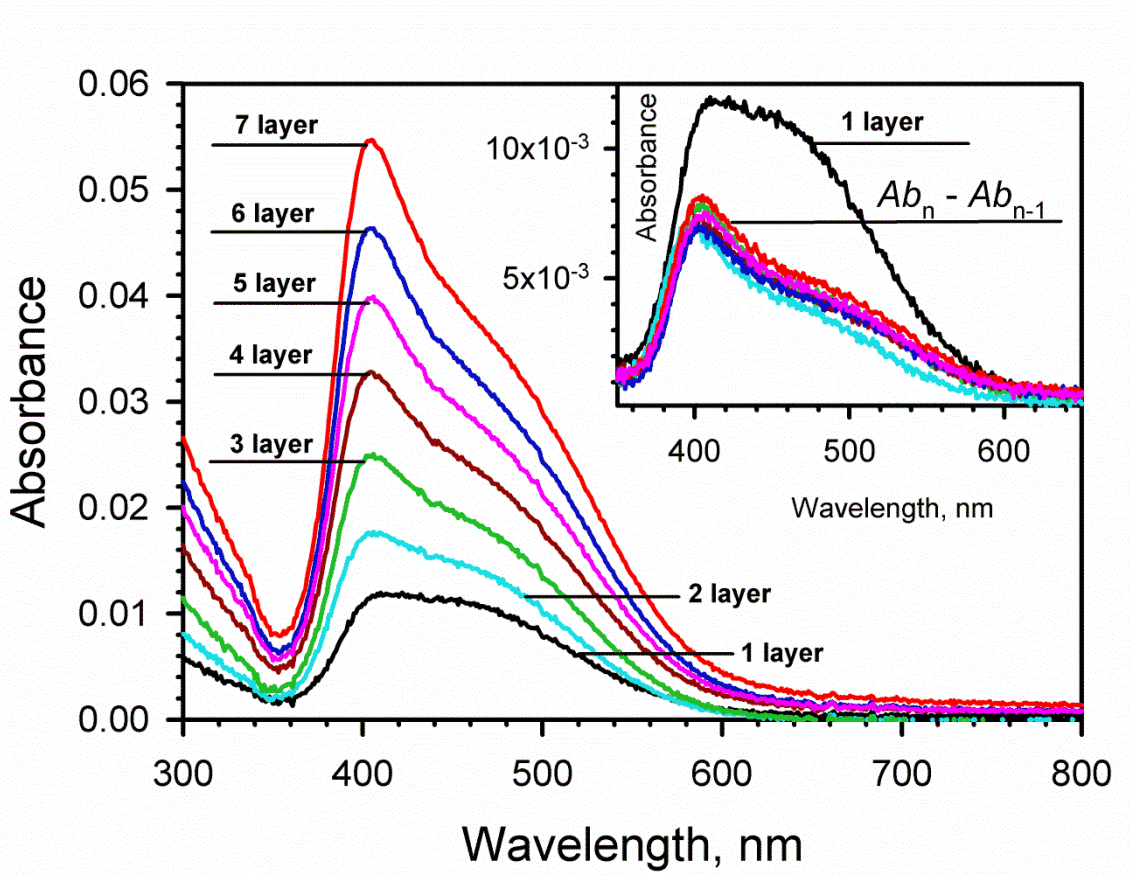

Figure 5: Absorption spectra of 1, 2, ... 7 SP:SA = 1:1 LS multilayers (π_{Trans} = 30 mN/m). The number of the transferred layers is indicated in the Figure. Insert: spectrum of the first monolayer and the subtracted spectra of the following layers ($Ab_n - Ab_{n-1}$). Similar line colors to indicate the number of layers used in both graphs.

The maximum value for the absorption spectra increased monotonically with increasing the number of transferred monolayers. The inset in Figure 5 shows the spectrum of the first monolayer (black line), as well as the spectra obtained by subtracting two successive spectra ($Ab_n - Ab_{n-1}$). The subtracted spectra ($Ab_n - Ab_{n-1}$) were almost coincident for any n transferred monolayer, although a quite different spectrum was obtained for the first monolayer. The transference of monolayers has been performed at different values of π_{Trans}. The results indicated that both the shape and height of the first monolayer spectrum depended on the transfer pressure. However, for $\pi_{Trans} \geq 7$ mN/m, the shape and height of the subtracted spectra were independent of the transfer pressure. Also, the shapes of the subtracted spectra were consistent with those of the reflection spectra recorded close to collapse. Consequently, the interactions between the monolayer and the support account for the changes observed in the spectra of the first monolayer transferred at different π_{Trans}. However, once the quartz surface was coated with the first monolayer, the subsequent films transferred did not change the structure that they had at the air-water interface. The molecular organization refers here to the arrangement of the hemicyanine group.

To rule out anisotropy in the plane of the quartz substrate, at least on the area covered by the footprint of the incident light beam, spectra were recorded under normal incidence of light at different polarization angles. The obtained spectra were identical in all cases. Figure 6 shows the transmission spectra of 7 monolayers obtained under an incidence of 45° and s and p-polarized light. The shape of the spectra under s and p-polarized light changed appreciably. Thus, while the s spectrum was a broadband centered at ~ 435 nm, the p spectrum had a narrow band centered at 405 nm and a shoulder at ~ 510 nm. The dichroic ratio, $DR = Ab_s/Ab_p$, is shown as inset in Figure 6 (solid line). The *DR* after the subtraction the s and p spectra of the first monolayer is also shown (dotted line). The *DR* ratio varied from the values of 0.8 for $\lambda \approx 405$ nm to 1.35 for $\lambda \approx 510$ nm. These transfers were repeated at different surface pressures $\pi_{Trans} \geq$ 7 mN/m, and the dichroic ratio ranged in all cases from 0.82 ± 0.04 for $\lambda \approx 405$ nm to 1.35 ± 0.05 for $\lambda \approx 510$ nm. Then, the polarization properties of the band must be related to the coexistence of two transition dipoles with different orientations. The first transition dipole is named H component, and has the maximum absorption at ~ 405 nm. The second transition dipole is named J component, and has the maximum absorption at

~ 510 nm, (see Scheme 2C below, where the s and p subtracted spectra Ab_2 - Ab_1 are shown).

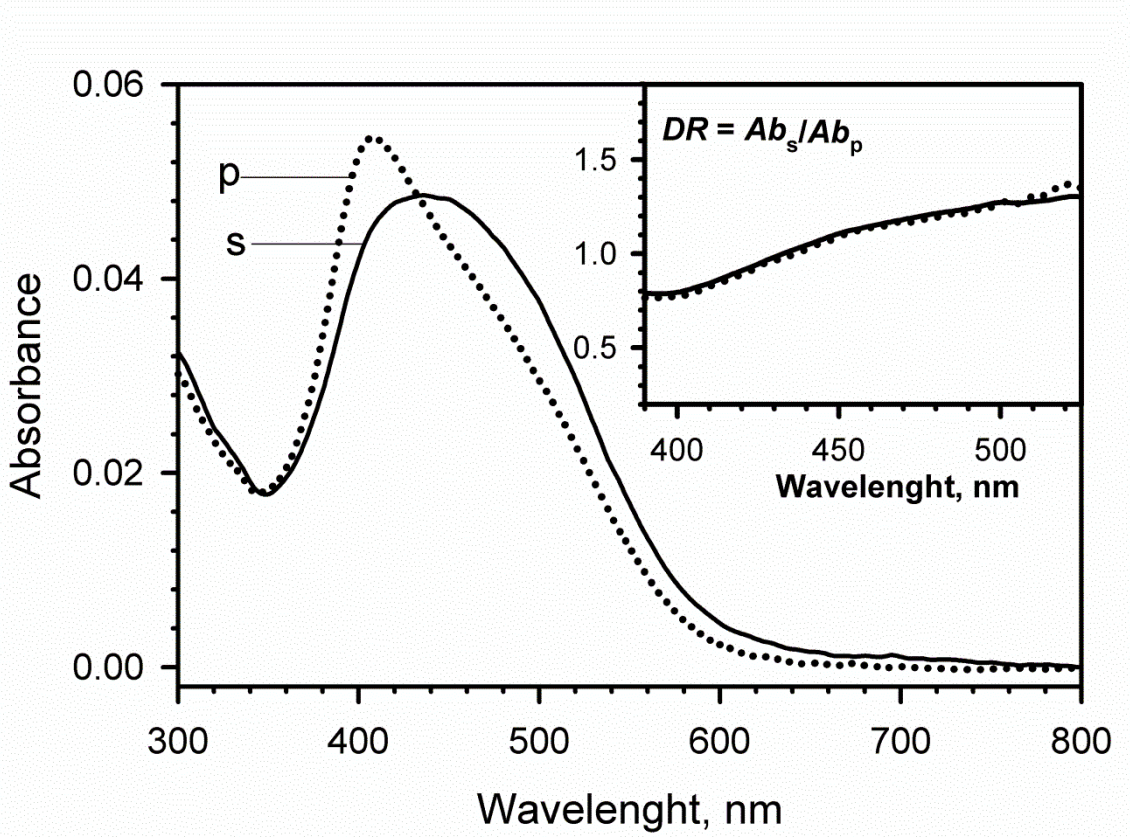

Figure 6: s- and p- polarized transmission spectra of 7 LS monolayers of SP:SA = 1:1, obtained under an incidence of 45° and transferred at π_{Trans}=30 mN/m. Insert: the variation of *DR* at the 390–520 nm region (solid line). With dotted line, the *DR* after subtraction of the s and p spectra of the first monolayer is also shown.

For very thin films, i.e., for weak absorption values (< 1%), and according to Vandevyver et al.,[27] the dichroic ratio *DR* can be expressed as:

$$DR = \frac{Ab_s}{Ab_p} = \left[\frac{n_1\cos(r)+n_3\cos(i)}{n_1\cos(i)+n_3\cos(r)}\right]\left[\frac{n_2^4\left\langle \sin\ \theta\ ^2\right\rangle}{2n_1^3 n_3\sin(i)^2\left\langle\cos(\theta)^2\right\rangle + n_2^4\left\langle \sin\ \theta\ ^2\right\rangle\cos(i)\cos(r)}\right] \qquad (2)$$

where n_1 (= 1), n_2 and n_3 (= 1.43) are the refractive index of air, film and quartz, respectively, i is the incidence angle of the light, r = arcsin[n_1 sin(i)/ n_3] is obtained from Snell's ratio, θ is the angle between the transition dipole and the normal to the support, and brackets denote average values. According to equation (2), and using n_2 =

1.6,[4] and $i = 45º$, $DR = 1.56$ was obtained for $\theta = 90º$ (parallel orientation with respect to the support), while $DR = 0$ for $\theta = 0º$ (perpendicular orientation).

From equation (2) ($n_2 = 1.6$ and $i = 45º$), the tilt angle from the *DR* values has been calculated, obtaining $\theta = 32° \pm 2°$ for $DR \approx 0.82$ ($\lambda \approx 405$ nm), and $\theta \approx 56° \pm 4°$ for $DR \approx 1.35$ ($\lambda \approx 510$ nm). In any case, these values must be carefully considered, since the H and J components of the absorption band could not be completely resolved. The *DR* variation (Figure 6) confirmed that the method previously used to determine the tilt of the chromophore at the air-water interface, which consisted on the integral of the reflection band, can not be used for the SP:SA system.

In the present case, there are two possible explanations for the variation of *DR* in the region of 400-510 nm. The first reason could be the coexistence of various types of aggregates with different orientations with respect to the interface. However, this explanation seemed unlikely. Indeed, in case of the coexistence of two or more kinds of aggregates, the relative proportion between them should vary with the applied surface pressure, which would be detected by changes in the shape of the spectrum under normal incidence with non-polarized light. Excluding the effect of the first monolayer transferred, this was not detected in the spectra of the following monolayers. In order to detect the possible presence of various kinds of aggregates, the emission spectra of the transferred films have been recorded, exciting at 405 and 510 nm. In the case of the coexistence of different types of aggregates, each of them should have different emission properties, and different emission spectra should be obtained. However, the emission of the SP:SA films was not detected under excitation at 405 and 510 nm, which points to the existence of a single type of aggregate. Given the case of coexistence of J and H aggregates, emission from (at least) the J aggregates is expected (Kobayashi, J aggregates books).[5] Therefore, the absence of emission indicates the occurrence of only H aggregates. Moreover, data obtained by GIXD and IRRAS at the air-water interface, support the idea of the existence of a single type of aggregate. As previously commented, GIXD peaks are well-defined, arising from a single crystalline phase. Moreover, the occurrence of different aggregate types would lead to a broadening of the IRRAS bands, as they would arise from different contributions, which is not the case herein.

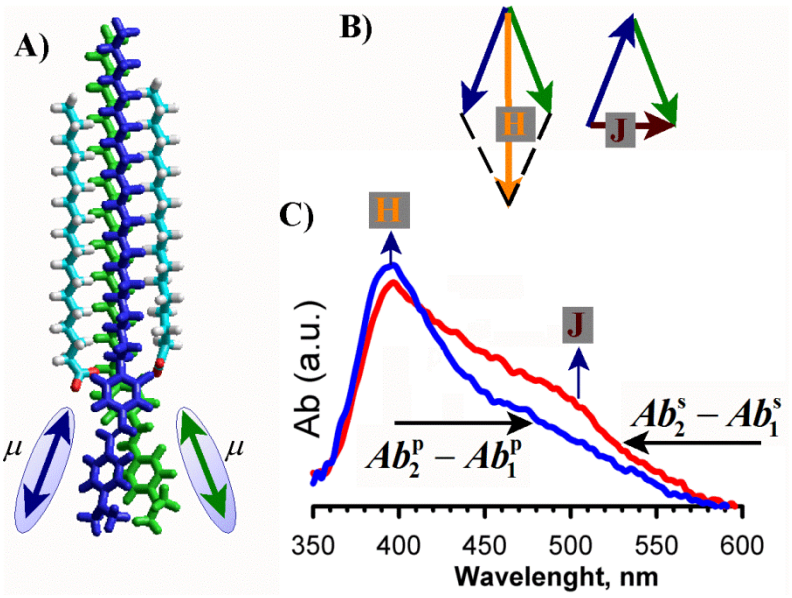

Scheme 2: A) Hemicyanine aggregation model sketch, where μ represents the transition dipole. B) The two optically allowed components of the addition of the transition dipole. C) Spectra obtained by subtracting the s and p polarized light spectra obtained from the second and first monolayer (Ab_2 - Ab_1).

The second phenomenon that may explain the variation of *DR* shown in Figure 6 is the existence of inequivalent molecules in the aggregate. This phenomenon has been described previously for molecular crystals according to Davidov's exciton theory, which shows that a given molecular energy level may be split into as many components as there are inequivalent molecules per unit cell.[7,28] In addition to the spectral splitting, the Davydov bands exhibit distinct polarization properties, as in our case.

Focusing our attention exclusively on two adjacent SP molecules, and in spite of SP molecules counteract their positive charges with the stearic acid molecules, it can be assumed that the close proximity between hemicyanine groups will lead to a strong repulsion between their dipole moments. In order to reduce this repulsion energy, the partial rotation of the groups in opposite directions may occur, as shown in Scheme 2A (the two SP molecules are drawn in different colors). In this configuration, the transition dipoles, μ, are not parallel, and the addition of these dipoles gives rise to two optically allowed components: one almost perpendicular to the support (H component) and another almost parallel to the support (component J) (see Scheme 2B). The structure drawn in Scheme 2A is solely a sketch obtained by means of the MM+ method.[29] The geometry of SP (positively charged) and SA (stearic acid anion) molecules has been previously optimized by means of the RM1 semiempirical method.[30] The results could

not be extrapolated to the experimental conditions existing at the air-water interface, but it should be highlighted that the hemicyanine groups are aggregated and slightly twisted by one another in the structure optimized by MM+ method (see Scheme 2A).

The tilt angles, as determined for the H and J components on the quartz support, can not be extrapolated directly to the monolayer at the air-water interface: reorientation of the film may happen during the transfer process. However, the shape of the reflection band recorded at the air-water under high surface pressure, and the shape of the absorption band on quartz, once the spectrum of the first monolayer was subtracted, were almost coincident. This fact clearly indicated that the air-water absorption band should have the same polarization properties as the quartz band, i.e. the band is split into its two components H and J. Moreover, on quartz, the angle of the H component, $\theta \approx 32°$, represented the average tilt angle of the hemicyanine transition dipole with respect to the normal of the support. This average angle value was almost coincident with that obtained from geometric considerations at the air-water interface, $\theta \approx 35°$, assuming a projected area of the hemicyanine group over the interface of about 0.4 nm^2.

For the SP:DMPA monolayer at the air-water interface, the hemicyanine tilt angle has been determined using the method based on the integration of the reflection band.[4] In order to check if the method is successful for this system, monolayers of SP:DMPA = 1:1 have been transferred on quartz substrates by the same procedure as for the SP:SA system. The results indicated that the splitting of the band also exists in the SP:DMPA system, although the J component showed much less intensity in this case. The difference in intensities could be related to a larger separation between hemicyanine groups and, therefore a lower rotation between them. In addition, the H component absorbed at 460 nm, being the tilt angle on quartz about 50°, being approximately coincident with the angle previously obtained at the air-water interface.[4] It can be concluded, that the method of integration of the band led to a correct angle value because of the small intensity of the J component.

4.1.4. Conclusions

The formation of mesoscopic 2D structures from mixed SP:SA = 1:1 monolayers at the air-water interface has been reported, and compared with the previously reported structures of the SP:DMPA = 1:1 system.[4] With regard to the SP:DMPA = 1:1 films, the replacement of DMPA by SA implies reducing the available area for the hemicyanine

aggregation, since each SA molecule provides only one alkyl chain to the set, being the minimum perpendicular section of the 1:1 mixture around 0.4 nm^2 per SP molecule. In the case of the SP:DMPA mixed monolayer, DMPA provided two alkyl chain to the set, with a minimum perpendicular section of the 1:1 mixture around 0.6 nm^2 per SP molecule.

The SP:SA = 1:1 monolayer forms star-shaped domains, bearing inner textures, related with anisotropy. The anisotropy is provoked by the absorption of the polar group. The anisotropy is related to a high degree of order in the interface. Therefore, SP:SA mixed monolayer might be defined as a 2D molecular crystal. However, for the SP:DMPA = 1:1 film circular domains have been observed. Furthermore, branches grow from circular domains when there is an increase in temperature.

GIXD experiments for the SP:SA = 1:1 mixed showed that the hydrocarbon chains adopted, at low values of surface pressure, a L_{2h} phase with a small tilt of the hydrocarbon chains in the NN direction. At ~5 mN/m, the chains adopted an untilted conformation with NNN unit-cell distortion. This distortion might be ascribed to the effect of the bulky SP headgroup. The tight packing of the hydrocarbon chains has been further confirmed by IRRAS. Significant changes in the organization of the polar groups when DMPA was replaced by SA in the mixed film were observed by UV-vis spectroscopy. The maximum wavelength of the reflection band shifted from 475 nm to 410 nm for the SP:SA = 1:1 system, while for the SP:DMPA = 1:1 system the shift was from 475 nm to 459 nm. The longer shift for SP:SA film was indicative of the greater interaction between the hemicyanine groups in the presence of SA. The splitting of the absorption band has been related to the existence of non-equivalent molecules per unit cell in the aggregate.[7,28] Thus, the close proximity between hemicyanine groups might cause a strong repulsion between their dipole moments, leading to a partial rotation of the groups in opposite directions. The transition dipoles, μ, are not parallel, resulting in two optically allowed components: one almost perpendicular to the substrate (H component) and another almost parallel to the substrate (J component). The splitting of the absorption band was not previously observed for the SP:DMPA film because of the lower intensity of the component J, caused by both the greater separation between hemicyanine groups and the least amount of tilt between them.

The changes observed by replacing DMPA for SA in the mixed monolayer should relate primarily to the less area available for the folding and hemicyanine

aggregation. A high packing of alkyl chains for both mixed monolayers has been observed by GIXD. The anisotropy of the domains is caused by the polar groups. The anisotropy is related to a high degree of order and packing of such groups (molecular crystal). The splitting of the absorption band supports this idea.

The domain shape is mainly originated from the interactions between the polar groups and the limitations of available space in this region of the monolayer. The interactions between the alkyl chains are fundamental in maintaining the crystal structure formed, but appear they do not play the main role in the final geometry of the domain.

4.1.5 Supporting Information

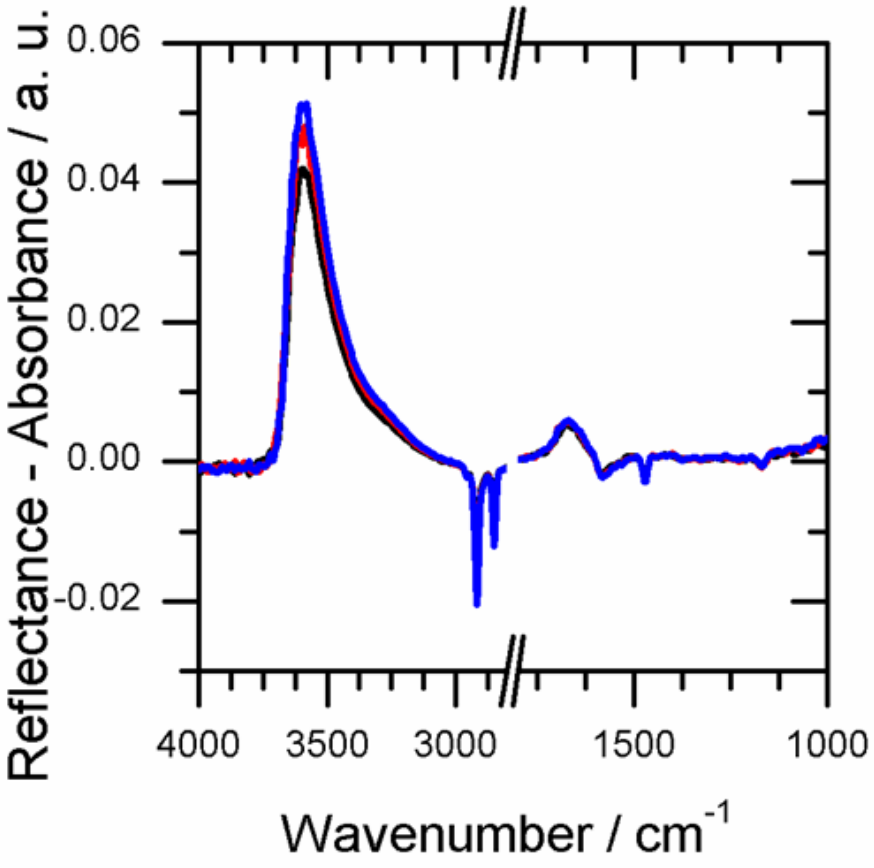

Figure S1. IRRA spectra from the mixed SA:SP monolayer in a molar ratio 1:1 at $T = 21°C$, at different surface pressures. Spectra have been collected at an incidence angle of 40° by using p-polarized light. The different values of surface pressures are depicted as follows. Black: 3 mN/m. Red: 10 mN/m. Blue: 25 mN/m.

Acknowledments

The authors thank the Spanish CICYT for financial support of this research in the framework of Projects CTQ2007-64474, and CTQ2010-17481 and also thank the Junta de Andalucía (Consejería de Innovación, Ciencia y Empresa) for special financial support P08-FQM-4011. A. González-Delgado, thanks the Ministerio de Ciencia e Innovación for a pre-doctoral grants (FPI program) and Juan J. Giner-Casares acknowledges Alexander von Humboldt Foundation for a postdoctoral fellowship.

References

(1) Johann, R.; Vollhardt, D.; Möhwald, H. *Colloid Polym. Sci.* **2000**, *278*, 104.

(2) Vollhardt, D.; Liu, F.; Rudert, R. *Journal of Physical Chemistry B* **2005**, *109*, 17635.

(3) Giner-Casares, J. J.; de Miguel, G.; Pérez-Morales, M.; Martín-Romero, M. T.; Muñoz, E.; Camacho, L. *J. Phys. Chem. C.* **2009**, *113*, 5711.

(4) González-Delgado, A. M.; Rubia-Paya, C.; Roldán-Carmona, C.; Giner-Casares, J. J.; Perez-Morales, M.; Muñoz, E.; Martín-Romero, M. T.; Camacho, L.; Brezesinski, G. *J. Phys. Chem. C* **2010**, *114*, 16685.

(5) Kobayashi, T. *J-Aggregates* Wold Scientific: Singapore, 1996.

(6) Kuhn, H.; Försterling, H. D. *Principles of Physical Chemistry*; Jonh Wiley & Sons: New York, 1999.

(7) Pope, M.; Swenberg, C. E. *Electronic Processes in Organic Crystals and Polymers*; Oxford Science Publications: New York, 1999.

(8) Grüniger, H.; Möbius, D.; Meyer, H. *J. Chem. Phys.* **1983**, *79*, 3701.

(9) Kaganer, V. M.; Peterson, I. R.; Kenn, R. M.; Shih, M. C.; Durbin, M.; Dutta, P. *J. Chem. Phys.* **1995**, *102*, 9412.

(10) Jaquemain, D.; Leveiller, F.; Weisbuch, S.; Lahav, M.; Leiserowitz, L.; Kjaer, K.; Als-Nielsen, J. *J. Am. Chem. Soc.* **1991**, *113*, 7684.

(11) Als-Nielsen, J.; Jaquemain, D.; Kjaer, K.; Lahav, M.; Levellier, F.; Leiserowitz, L. *Phys. Rep.* **1994**, 251.

(12) Kjaer, K. *Physica B* **1994**, *198*, 100.

(13) Brezesinski, G.; Dietrich, A.; Struth, B.; Böhm, C.; Bouwman, W. G.; Kjaer, K.; Möhwald, H. *Chem. Phys. Lipids* **1995**, *76*, 145.

(14) Kaganer, V. M.; Möhwald, H.; Dutta, P. *Rev. Mod. Phys.* **1999**, *71*, 779.

(15) Muenter, A. H.; Hentschel, J.; Börner, H. G.; Brezesinski, G. *Langmuir* **2008**, *24*, 3306.

(16) Flach, C. R.; Gericke, A.; Mendelsohn, R. *J. Phys. Chem. B* **1997**, *101*, 58.

(17) Bibo, A. M.; Knobler, C. M.; Peterson, I. R. *J. Phys. Chem.* **1991**, *95*, 5591.

(18) Brezesinski, G.; Vollhardt, D.; Iimura, K.; Cölfen, H. *J. Phys. Chem. C* **2008**, *112*, 15777.

(19) Socrates, G. I. *nfrared and Raman Characteristic Group Frequencies: Tables and Charts*; John Wiley & Sons: Weinheim, Germany, 2001.

(20) Orrit, M.; Möbius, D.; Lehmann, U.; Meyer, H. *J. Chem. Phys.* **1986**, *85*, 4966.

(21) Martín, M. T.; Prieto, I.; Camacho, L.; Möbius, D. *Langmuir* **1996**, *12*, 6554.

(22) Pedrosa, J. M.; Martín-Romero, M. T.; Camacho, L.; Möbius, D. *J. Phys. Chem. B* **2002**, *106*, 2583.

(23) Song, Q.; Evans, C. E.; Bohn, P. W. *J. Phys. Chem* **1993**, *97*, 13736.

(24) Lusk, A. L.; Bohn, P. W. *Langmuir* **2000**, *16*, 9131.

(25) Lusk, A. L.; Bohn, P. W. *J. Phys. Chem. B* **2001**, *105*, 462.

(26) Hall, R. A.; Thistlethwaite, P. J.; Grieser, F.; Kimizuka, N.; Kunitake, T. *Colloids and Surfaces A-Physicochemical and Engineering Aspects* **1995**, *103*, 167.

(27) Vandevyver, M.; Barraud, A.; Ruaudel-Teixier, A.; Maillard, P.; Gianotti, C. *J. Colloid Interface Sci.* **1982**, *85*, 571.

(28) Davydov, A. S. *Theory of Molecular Excitons*; McGraw-Hill: New York, 1962.

(29) Hyperchem; 6th ed.; Htpercube, Inc.: Gainesville, FL, 1999.

(30) Rocha, G. B.; Freire, R. O.; Simas, A. M.; Stewart, J. J. P. *J. Comput. Chem.* **2006**, *27*, 1101.

CAPÍTULO 5

CALIXARENOS ANFIFÍLICOS Y SUS COMPLEJOS DE INCLUSIÓN CON FULLERENO EN LA INTERFASE AIRE-AGUA

5.1 Langmuir monolayers of an inclusion complex formed by a new calixarene derivative and fullerene

The design of new molecules with directed interactions to functional molecules as complementary building blocks is one of the main goals of supramolecular chemistry. A new *p-tert*-butylcalix[6]arene monosubstituted derivative bearing only one alkyl chain with an acid group (C6A3C) has been synthesized. The C6A3C has been successfully used for building Langmuir monolayers at the air/water interface. The C6A3C molecule adopts a flat-like orientation with respect to the air-water interface. The molecular structure gives the molecule amphiphilic character, while allowing the control of both the dissociation degree and the molecular conformation at the air-water interface. The C63AC has been combined with pristine fullerene (C60) to form the supramolecular complex C6A3C:C60 in 2:1 molar ratio (CFC). The CFC complex retains the ability of C6A3C to form Langmuir monolayers at the air/water interface. The interfacial molecular arrangement of the CFC complex has been convincingly described by in situ UV-vis reflection spectroscopy and synchrotron X-ray reflectivity measurements. Computer simulations complement the experimental data, confirming a perpendicular orientation of the calixarene units of CFC with respect to the air-water interface. This orientation is stabilized by the formation of intermolecular H-bonds. The interfacial monolayer of the CFC supramolecular complex is proposed as a useful model for the well-defined self-assembly of recognition and functional building blocks.

Paper sent to *Langmuir* for publication.

5.1.1. Introduction

Calixarene chemistry has been established as a readily available molecular platform to build a wide variety of interesting cavity-containing and multifunctional molecules. Calixarene derivatives have been widely used as recognition agents. The main interest of calixarenes is based on their broad potential for the design of supramolecular host–guest structures. The supramolecular structures are of high relevance for selective molecular recognition of biologically relevant species, metal cation complexation, design and synthesis of enzyme-mimic systems, or gas sensing.[1-2]

Supramolecular architectures combining electron-deficient fullerenes and calix[n]arene derivatives are of large interest for applications in the purification of fullerenes.[3-5] Supramolecular complexes of fullerenes with recognition-active molecules as host–guest entities have been described in both aqueous[6-7] and organic solvents, where weak charge transfer (CT) forces play an important role in the complexation.[8-10]

The conformational mobility of calixarenes is a remarkable feature. *p-tert*-butylcalix[6]arene might display up to eight conformations: 'cone' and 'partial cone', which differ in the respective orientation of the aromatic rings. The conformational freedom is a key factor in the optimization of the particular host-guest interactions between calixarene ligands and their guests.[11] The study of calixarenes at the air/water interface provides useful information on their conformation and complexation ability in a very simple and straightforward way. The conformational insights attained at the air/water interface are in agreement with results obtained by using more complex techniques.[12-16] The use of calixarenes with amphiphilic character offers the advantage of an additional structural factor allowing a certain control in the organization and molecular conformation.

In this work, a mono substituted asymmetric derivative of *p-tert*-butylcalix[6]arene has been synthesized. One of the six-OH groups is replaced by a -O-$(CH_2)_3$COOH (see Scheme 1, left). The synthesized compound will be named as C6A3C herein. Symmetrical derivatives of calix[n]arenes in which all -OH groups were replaced by -O-$(CH_2)_n$COOH have been already studied.[17-18] These symmetric compounds were highly amphiphilic, although the overcrowding of the acid groups prevented adequate control of the degree of dissociation and conformation at the air-water interface.[19-20] The aim in synthesizing the derivative C6A3C is the fine tuning of both the conformation and the degree of dissociation. Thus, the existence of only one

acid group per calix[6]arene unit gives the C6A3C amphiphilic character. Remarkably, given the existence of a single alkyl chain in the C6A3C molecule, the calix[6]arene ring displays great flexibility. This flexibility results in a variety of conformational changes that might be induced by the anisotropy or the applied surface pressure at the air-water interface.

The flexibility of the C6A3C molecule might lead to several conformations coexisting at the air/water interface. The variation of the induced surface pressure and the composition of the aqueous subphase, i. e., through ion complexation, might lead to a certain control over the conformational changes.[12] The formation of inclusion complexes can be used to set a specific conformation.[21] In this work we have formed the inclusion complex C6A3C:C_{60}, with a 2:1 stoichiometry. The physicochemical properties of the complex at the air-water interface have been described.

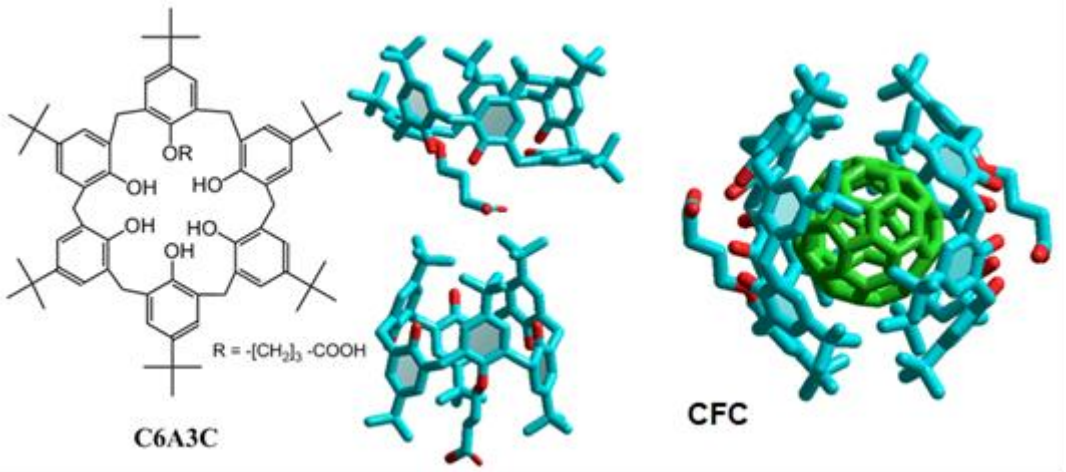

Scheme 1: Left: Molecular structure of C6A3C. Centre: two structures obtained from MM geometry optimization corresponding to the cone and OH-alternate conformation. Right: MM geometry optimization structures obtained for the C6A3C:C_{60} = 2:1 complex (CFC).

5.1.2. Experimental

Materials. Pure chloroform as spreading solvent was obtained from Sigma-Aldrich and used as received. Toluene for the CFC synthesis was purchased from Across Organics (extra dry with molecular sieves, water <50 ppm) and used as received. Ultrapure water, produced by a Millipore Milli-Q unit, pre-treated by a Millipore reverse osmosis system (>18.2 MΩcm), was used as subphase.

Synthesis: ^{1}H- and ^{13}C-NMR spectra were recorded on a Bruker DRX 400 (chemical shifts in ppm). Mass spectra (and electrospray ionisation - ESI) were recorded on a Bruker micrOTOF-Q apparatus, at the Service Commun de Spectrométrie de Masse Organique, Nancy, or on a Varian Mod 1200L (Triple cuadrupole) at Servicio Central de Apoyo a la Investigación, Córdoba. Infrared was performed on a Mattson Research Series instrument or a Bruker Vector 22 apparatus (KBr, ν in cm^{-1}). Elemental analyses were performed at the Service de Microanalyse, Nancy. Merck TLC plates were used for chromatography analysis (SiO_2, ref 1.05554; Al_2O_3, ref 1.05581). Hexa-*p-tert*-butyl-calix[6]arene and other reactants were commercially available and used as received.

Synthesis of calixarene mono- carboxyl derivative:

5,11,17,23,29,35-hexakis-tert-butyl-calix[6]arene-39,39,40,41,42-pentol-37-[4-(ethylbutyrate)] **(1)** *:* Hexa-*p-tert*-butyl-calix[6]arene (2 g, 2.06 mmol) was dissolved in CH_3CN and refluxed for half an hour in the presence of $NaHCO_3$ (0.173 g, 2.00 mmol) and K_2CO_3 (0.142 g, 1.03 mmol). Then, 4-bromo-ethylbutyrate (0.294 ml, 2.05 mmol) was added to the mixture and the reflux was kept for 30 hours under Ar. After evaporation of the solvent, the residue was dissolved in CH_2Cl_2 and filtered to remove inorganic salts. The concentrated filtrate was chromatographed (SiO_2; CH_2Cl_2/MeOH 1:1) to give the monoethylester derivative **1** (0.466 g, 20.4%). White solid. IR(pure; ATR): 1732 (C=O). ^{1}H NMR ($CDCl_3$): 0.89 (t, J = 6.8 Hz, 3 H, OCH_2CH_3); 1.15 (s, 9 H, Me_3C); 1.21 (s, 9 H, Me_3C); 1.26 (s, 18 H, Me_3C); 1.28 (s, 18 H, Me_3C); 2.39 (m, 2 H, $OCH_2CH_2CH_2COO$-); 2.94 (t, J = 7.1 Hz, 2 H, $OCH_2CH_2CH_2COO$-); 3.45 (d, J = 14.1 Hz, 2 H, Ar-CH_2-Ar); 3.51 (d, J = 13.6 Hz, 2 H, Ar-CH_2-Ar); 3.57 (d, J = 14.4 Hz, 2 H, Ar-CH_2-Ar); 3.99 (d, J = 13.8 Hz, 2 H, Ar-CH_2-Ar); 4.15 (q, J = 7.3 Hz, OCH_2CH_3); 4.21-4.29 (m, 4 H, Ar-CH_2-Ar + $OCH_2CH_2CH_2COO$-) ; 4.30 (d, J = 13.6 Hz, 2 H, Ar-CH_2-Ar); 7.06 (s, 2 H, ArH); 7.076 (s, 2 H, ArH); 7.09-7.17 (s + AB, 8 H, ArH). ESI-MS (CH_3CN + HCOOH):1109.68 ($[M + Na]^+$); 2197.38 ($[2 M + Na]^+$). Anal. Calcd. For $C_{72}H_{94}O_8$, 0.3 CH_2Cl_2(1112.99): C, 78.02; H, 8.57; O, 11.77; found: C 78.32, H 8.10.

5,11,17,23,29,35-hexakis-tert-butyl-calix[6]arene-39,39,40,41,42-pentol-37-[4-(butyric)] acid (**C6A3C**)*:* A mixture of calixarene monoester **1** (0.3 g; 0.269

mmol) and 0.22 ml of 15% NaOH aqueous solution (0.825 mmol) in ethanol (25 ml) was refluxed at 85°C for 8 h. Then, ethanol was removed under reduced pressure and water was added to the solid residue. 1M HCl was added until pH = 1 was raised. The resulting solid was recovered by filtration and dissolved in CH_2Cl_2 (20 ml). This solution was washed with 1M HCl (20 ml) and brine (20 ml). The organic phase was recovered, dried over Na_2SO_4, and evaporated to dryness to give **C6A3C** as a white solid (0.248 g, 85.5 %). IR (KBr pellets): 1748, 1716 (C=O). ^{1}H NMR (DMSO-d6): 1.02 (s, 9 H, *Me*$_3$C); 1.07 (s, 18 H, *Me*$_3$C); 1.13 (s, 9 H, *Me*$_3$C); 1.15 (s, 18 H, *Me*$_3$C); 2.11 (m, 2 H, $OCH_2CH_2CH_2COO$-); 2.57 (t, J = 7.25 Hz, 2 H, $OCH_2CH_2CH_2COO$-); 3.47-4.23 (m, 14 H, Ar-CH_2-Ar + $OCH_2CH_2CH_2COO$-); 6.80-7.09 (m, 10 H, ArH); 7.15 (s, 2 H, ArH); 7.99 (s, 2 H, OH); 8.07-8.30 (m, 3 H, OH); 12.06 (*br* s, COOH). ESI-MS (CH_3CN): 1060 ($[M + H]^+$; 1077 ($[M + NH_4]^+$). Anal. Calcd. For $C_{70}H_{90}O_8$, 0.25 CH_2Cl_2 (1080.69): C 78.08, H 8.44; found: C 78.29, H 8.03.

Synthesis of calixarene-fullerene complex CFC.

A mixture 2 mM of C6A3C and 1 mM C_{60} in toluene was refluxed at 140ºC for 24h. Then, a change in color from violet to brown was observed, indicating the complex formation. The obtained product was used without further purification. In figure 1, UV-Vis spectra of C_{60} (1 mM, red line) and C6A3C (2 mM, blue line) in toluene solution are shown. Also, figure 1 shows the UV-Vis spectra of the C6A3C:C_{60} = 2:1 complex (black line) which will be denominated CFC. The CFC concentration was 1 mM (2 mM in C6A3C and 1 mM in C_{60}). As can be seen, there is a large spectroscopic change in the region from 420 to 480 nm due to the charge transfer (CT) absorption band between the C_{60} and the calixarenes,[22-23] indicating the formation of the complex. In order to confirm the stoichiometry of the complex, the increase of the absorption at 437 nm *vs.* mole fraction of C_{60} (for a constant concentration of C_{60}) was analyzed, obtaining the maxima variation for the 2:1 stoichiometry.[23]

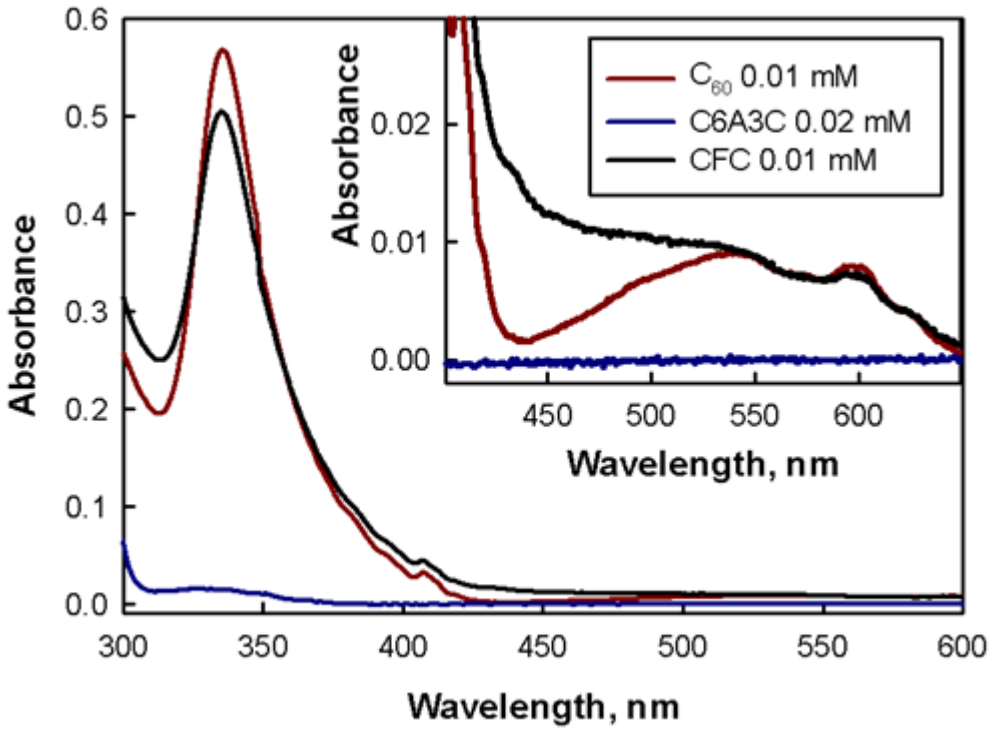

Figure 1: UV-Vis spectrum (toluene solutions) of C_{60} 0.01mM (red line); C6A3C 0.02mM (blue line); and CFC 0.01mM [C6A3C 0.02mM+ C60 0.01mM] (black line).

Methods. Langmuir monolayers of C6A3C and CFC were prepared on pure water at 21 ºC. After evaporation of the organic solvent, the monolayer was compressed or expanded using a movable barrier on a Nima rectangular trough provided with a filter paper Wilhelmy plate with a compression velocity of 10–20 $Å^2$ $molecule^{-1}$ min^{-1}, facilitating the recording of surface pressure–area (π–A) isotherms. The system was also equipped with a vibrating capacitor device, Kelvin Probe SP1 (Nanofilm Technologies, Gottingen, Germany) for measurement of the surface potential/area (ΔV–A).

Brewster angle microscopy (BAM) was used to gain additional information on the molecular organization of C6A3C and CFC in monolayers at the air–water interface. Images of the film have been recorded with a lateral resolution of 2 μm (I-Elli2000 supplied by NFT, Accurion GmbH, Göttingen, Germany). The image processing procedure included a geometrical correction of the image, as well as a filtering operation to reduce interference fringes and noise. Furthermore, the brightness of each image was scaled to improve contrast. The size of the images is 430 μm in width. The microscope and the film balance were located on a table with vibration isolation (anti-

vibration system MOD-2 S, Accurion GmbH, Göttingen, Germany) in a large class 100 clean room.

UV-Visible reflection spectra at normal incidence as the difference in reflectivity (ΔR) of the film-covered water surface and the bare surface were obtained with a *ref SPEC*^{2} surface analysis spectrometer, supplied by Accurion GmbH, Göttingen, Germany.

Specular X-Ray Reflectivity (XRR): The specular X-Ray reflectivity (XRR) measurements were performed on the undulator beamline BW1 at HASYLAB, DESY (Hamburg, Germany). XRR provides an averaged electron density profile normal to the interface of all molecules. For reflectivity measurements, the angles of incidence αi and reflected αf beams are equal and varied in a range $0.5\alpha_c < \alpha_i$ (α_f) $< 30\alpha_c$, where α_c=0.138. The reflected intensity was measured by a NaI scintillation detector in the plane of incidence as a function of the vertical scattering vector component Q_z. The electron density profile was obtained from the reflectivity curve using a linear combination of b-splines following the approach of Pedersen and Hamley. The electron density profiles were calculated using the StochFit software.[24]

Molecular Mechanics study. The molecular mechanics simulations were carried out using the HyperChem molecular modelling package.[25] The geometry of the molecule was preoptimized using the Amber96 force field with no partial charges. Then the charges were assigned using the AM1 semiempirical method. Next, the geometry was again optimized using Amber. The procedure was repeated until the convergence was achieved (the convergence criteria for geometrical optimization was 0.001 kcal/(Å·mol)). A similar method of assigning partial charges was used for other calixarene derivatives.[18,26-27] After charges were assigned, three runs of the molecular dynamics simulations were performed to search for the possible existence of other structures with lower energy. Each run consisted of heating the structure to 300 K, molecular dynamics simulations for 5 ps, and then annealing to 0 K.

C6A3C molecule has 20 different conformations depending on the relative orientation of the -OH groups respect to the acid group. The molecular geometry optimization in vacuum was performed starting from some of these conformations. Scheme 1 (centre) shows two of the structures obtained starting from the conformation cone and OH-alternate, respectively. The energies of the found structures were very

similar in all runs. Often the formation of hydrogen bonds contributes to the stability of the species. Moreover, our results show that the formation of the inclusion complex between C6A3C and C_{60} is possible only when the calix[6]arene is in cone conformation. The structures obtained with C6A3C:C_{60} = 1:1 and 2:1 stoichiometry are very stable and correspond to true energy minimums. The structure obtained for the 2:1 complex is shown in Scheme 1 (right). In this representation, hydrogen atoms are not drawn and the C_{60} is green coloured in order to distinguish the different molecules.

5.1.3. Results and discussion

5.1.3.1 Surface pressure/Area isotherms. Figure 2 shows the surface pressure-molecular area (π-A) isotherms of C6A3C and CFC. The molecular area is expressed as surface area per C6A3C molecule in both cases. The Langmuir monolayer formed by pure C6A3C shows the overshoot of the surface pressure at a molecular area of ca. 2.6 nm^2/molecule. This value is indicative of a parallel orientation of C6A3C with respect to the air/water interface.[12] Scheme 2 shows an idealized representation of the C6A3C cone conformation and its interfacial projected area. The interaction between the hydrophilic region of the C6A3C, i. e., the OH and acidic groups, and water favors the cone conformation. However, different conformations might coexist at the air-water interface. The presence of the terminal acid group in the alkyl chain is sufficient to induce a parallel orientation of the C6A3C plane to the air/water interface for any given conformation of the calixarene molecule. The bare tert-butyl-calix[6]arene in absence of complex-forming ions in the subphase leads to a perpendicular conformation of the main plane of the molecule at the air/water interface.[12,28]

For a surface pressure of 10 mN/m the C6A3C isotherm shows an change of slope, being characteristic of other *p-tert*-butylcalix(6)arene derivatives. This change of slope has been attributed to a conformational phase transition.[12] Upon further compression of the Langmuir monolayer, a continuous rise of the isotherm resembling those presented by condensed phase is detected. There is no clear starting point of the one-phase region. For surface pressures above 22 mN/m, there is a decrease in slope of the π–A isotherm. This decrease in the slope cannot be related to a typical amphiphilic monolayers collapse, i.e., strong reduction of the surface area. This behavior has been related to a gradual loss of parallel orientation toward a more compact perpendicular orientation (ca. 1.8 nm^2/molecule, see Scheme 2).[12]

The complexation of the C_{60} molecule by two calixarene molecules leads to the supramolecular entity CFC, as shown in scheme 2. The surface pressure-molecular area isotherm of CFC is clearly different to that of pure C63AC. For CFC the surface pressure starts to rise at an area of ≈ 1.9 nm^2/C6A3C molecule. This value is indicative of a perpendicular orientation of C6A3C with respect to the interface[12] (see scheme 2). It also indicates that the C_{60} occupies no net area at the interface, which suggests the formation of the inclusion complex.

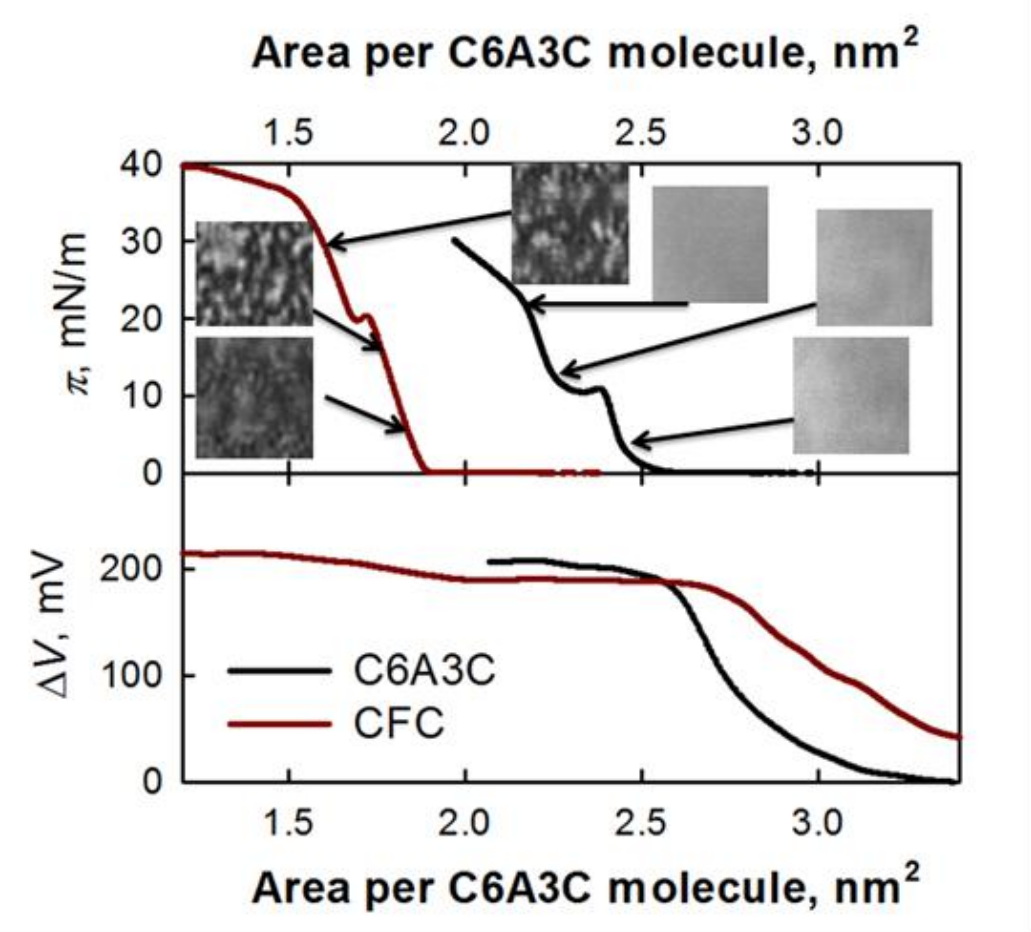

Figure 2. Top: Surface pressure−area (π–A) isotherms of C6A3C (black line) and CFC (red line). BAM images are show under different surface pressures. Image size: 42 μm width. Bottom: Surface potential-area (ΔV - A) isotherms of C6A3C (black line) and CFC (red line).

The change of slope in the isotherm is observed at a surface pressure of ca. 20 mN/m.A typical collapse is observed at a surface pressure of ca. 36 mN/m. The perpendicular orientation of C6A3C units is stabilized by means of the formation of inter molecularH-bonds.

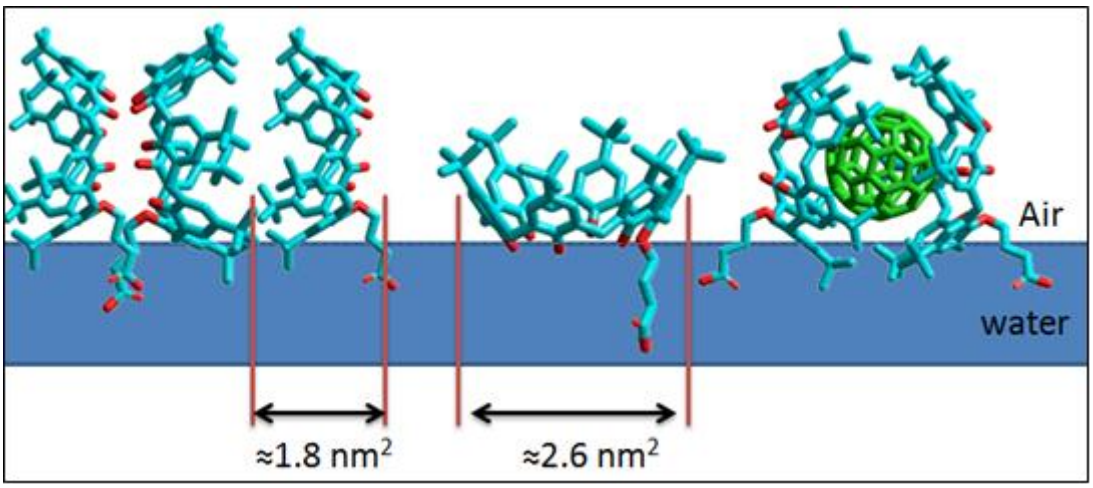

Scheme 2. Idealized representation of the interface projected area for the cone conformation of C6A3C, and CFC.

5.1.3.2 Brewster angle microscopy. The morphology of both monolayers was directly visualized by Brewster angle microscopy (BAM) simultaneously to the π-A isotherm recording. The Langmuir monolayer of pure C6A3C is completely homogeneous along the whole isotherm. However, the Langmuir monolayer of pure CFC shows a completely different morphology, with irregular bright and dark regions in an uneven fashion.

The absence of domains or micrometer structure in the monolayer of C6A3C might be due to the parallel orientation adopted by the ring of calix[6]arene. Indeed, in this orientation the interactions between molecules are weak, and hydrogen bonds can be formed only intramolecularly and with water molecules in the subphase. This situation does not favor the formation of large domains that could be visualized by BAM.

On the contrary, in the case of the monolayer of the complex CFC the interactions between neighboring molecules are strong due to the perpendicular orientation of the calix[6]arene ring, enabling the formation of intermolecular hydrogen bonding. Therefore, the observed structures are due to the lateral aggregation between the C6A3C units.

5.1.3.3 Surface potential - Area Isotherms. The surface potential of a Langmuir monolayer depends on three main factors: (a) the vertical component of the dipole moments of the monolayer molecules, (b) the relative orientation of the water

molecules, and (c) the ionic environment and the state of the headgroups and subphase. The first of these factors is very sensitive to molecular reorientations at the air/water interface. For this reason, studying the surface potential in calixarenes monolayers is of great interest, though it only provides qualitative information. Figure 2 (bottom) shows the ΔV vs A per C6A3C molecule for the C6A3C and CFC monolayers.

The π - A isotherm and the surface potential have opposite trends with the compression of the monolayer. In other words, the surface pressure begins to increase for higher values of molecular areas for the case of the C6A3C when compared to the CFC monolayer. On the contrary, the surface potential rises and reaches a first plateau for larger areas values in the case of the CFC monolayer. Thus, for the monolayer of pure C6A3C the surface potential starts to raise at an area of ≈ 3.30 nm^2/molecule and reaches a plateau (ca. +210 mV) at 2.60 nm^2/molecule. This value of molecular area coincides with the overshoot of surface pressure. This behavior suggests that the calixarene molecule does not adopt a particular conformation when spread on the air/water interface. Only the application of surface pressure induces the parallel conformation of the molecule. However, in the case of CFC monolayer the ΔV is different from zero even at a value of molecular area of ca. 3.5 nm^2, reaching a first plateau (ca. +180 MV) at areas of 2.8 nm^2. Upon further compression of the monolayer, the surface potential is approximately constant until ca. 1.9 nm^2 per C63AC molecule, on the overshoot of surface pressure. In the final steps of the isotherm the ΔV increased slightly up to values of ca. +210 mV. This behavior suggests that CFC adopts a defined conformation before the surface pressure begins to increase significantly.

The maximum values of ΔV are coincident for both monolayers, ca. +210 mV at the maximum stage of compression of the monolayer. Although this coincidence in the value of surface potential seems to be in contradiction with the different orientations models for the C6A3C and CFC monolayers, it can be attributed to the effect of the headgroup. In the case of no buffer in the subphase, i. e., neutral pH, the carboxylic group of the C63AC molecule must be partially dissociated. The orientation of the carboxylic group is assumed to be the main contribution to the total effective dipole moment of the whole monolayer at the air/water interface. In this scenario, the change in the orientation of the hydrophobic region of the C63AC molecule does not contribute significantly to the total value of surface potential. Therefore, the coincidence in the

value of surface potential indicates the same orientation of the carboxylic group for both C63AC and CFC monolayers.

5.1.3.4. In situ UV-vis Reflection Spectroscopy at the air–water interface. In order to obtain direct evidence of the presence of C_{60} in the CFC monolayer, UV-vis reflection spectra were recorded at different surface pressures. Figure 3 shows the UV-vis reflection spectra at π = 5, 15 and 30 mN/m. The UV-vis spectrum of CFC in toluene solution has been plotted in Figure 3 for comparison.

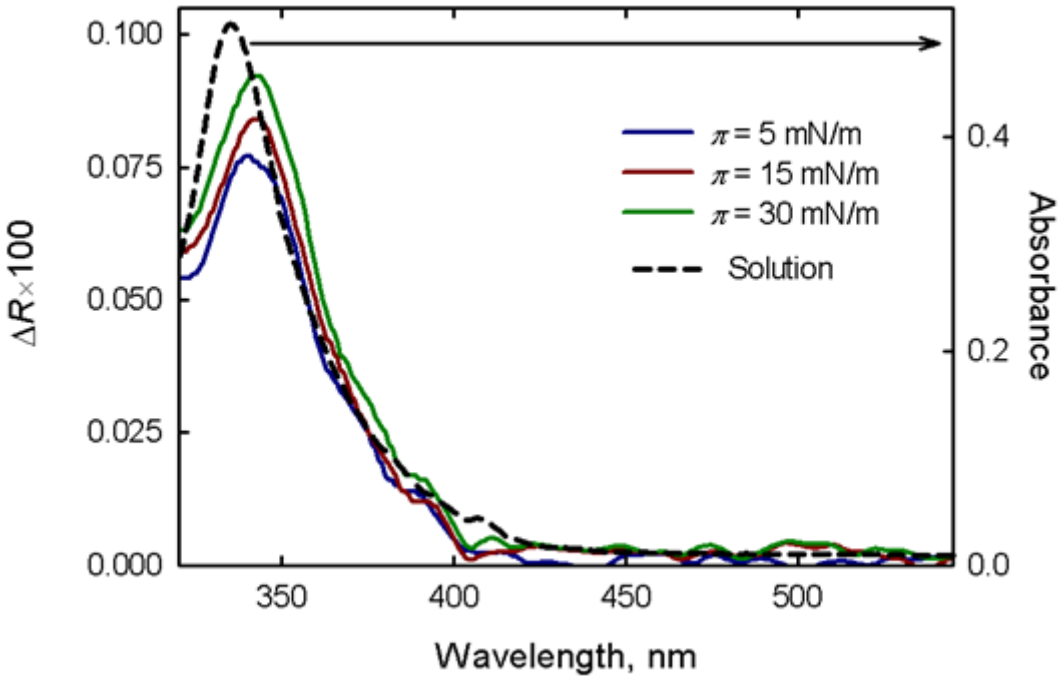

Figure 3. UV-vis Reflection spectra (ΔR) of the CFC monolayer obtained at different surface pressures (solid lines). Blue: 5 mN/m, red: 15 mN/m, green: 30 mN/m. For comparison, the absorption spectrum of CFC 0.01 mM on toluene solution (dashed line) is also shown.

The UV-vis reflection spectra show a small red shift from 335 nm band (solution) to 341 nm (air-water interface). This shift may be related to the aggregation of C_{60}[29] and/or to the different environments existing in the monolayer and in toluene solution. In most of the cases, C_{60} aggregation can be detected by the presence of a broad band centred around 450 nm.[29-30] However, this band has been not observed in the experiments presented herein. Remarkably, the width of the band at 341 nm at the air/water interface is very similar to that obtained in solution. Due to the resolution of

the reflection spectra it is not possible to detect the charge transfer bands (see Figure 1). Note that the UV-vis reflection spectra in the air-water interface correspond to a single monolayer.

For low values of absorption, the reflection ΔR is given in a reasonable approximation by,[31-32]

$$\Delta R = 2.303\times10^{3}\cdot\Gamma_{C60}\cdot f_{orient}\cdot\varepsilon\cdot\sqrt{R_s} \qquad (1)$$

where Γ_{C60} is the surface concentration of C_{60} in mol cm^{-2}, R_s = 0.02 is the reflectivity of the air–water interface at normal incidence,[33] ε is the extinction coefficient given as L mol^{-1} cm^{-1}, and f_{orient} is a numerical factor that takes into account the different average orientation of the chromophores in solution as compared to the monolayer at the air–water interface, which could be considered f_{orient} = 1 for pseudospherical molecules.[34-35]

The maximum value of reflection at π = 30 mN/m (341 nm, see Figure 3) is $\Delta R \approx 9.2\times10^{-4}$. From the CFC spectrum in toluene solution, we can obtain $\varepsilon \approx 5.0\times10^{4}$ L mol^{-1} cm^{-1} at 335 nm. This value is used herein, assuming no aggregation. Therefore, $\Gamma_{C60} \approx 5.6\times10^{-11}$ mol cm^{-2} is obtained from equation (1).

At π = 30 mN/m, the surface area per C6A3C molecule for the CFC monolayer is $A \approx 1.55$ nm^2 from the surface pressure-molecular area isotherm. Therefore, the surface concentration of calix[6]arene is $\Gamma_{C6A3C} = 10^{14}/AN_A \approx 1.1\times10^{-10}$ mol cm^{-2}, where N_A is the Avogadro number. Given the 2:1 stoichiometry of the C6A3C:C_{60} complex, the surface concentration of the C_{60} molecule is $\Gamma_{C60} \approx 5.05\times10^{-11}$ mol cm^{-2}. This value of surface area is in good agreement with the value obtained from the UV-vis reflection spectrum.

It has been observed that the aggregation of pristine C_{60} molecules leads to a decrease in molar extinction coefficient at 335 nm.[29-30] This decrease in the absorption properties of the CFC complex does not take place in the experiments presented herein, thereby confirming that there is no aggregation.

5.1.3.5. Synchrotron-based in situ X-ray Reflectivity (XRR). XRR experiments allows the determination of the vertical electron density profile of soft matter thin films.[36-37] The data for π = 30 mN/m showed a single decreasing reflectivity (Figure 4, left). The experimental data have been modeled using a one box model using

StochFit software.[24] The numerical fit of the experimental data allows obtaining a thickness of 10.9 ± 0.5 Å, and a relative electron density respect to bulk water of ρ /ρwater = 1.21 ± 0.02, considering an interfacial roughness of 3.42 ± 0.07 Å (Black solid line in Figure 4, center).

The vertical profile of electron density was determined from the spatial distribution of different atoms that HyperChem provided after geometry optimization of the complex.[25] Thus, in Figure 4-center, the green dashed line represents the relative electron density of C60, and the cyan dashed line represents the relative electron density of the two C6A3C units. The dashed black line represents the electron density of water which is fitted to a gaussian distribution for the contact region with the CFC monolayer. Finally, the overall relative electron density is represented as a red solid line.

The vertical thickness of the CFC complex, as depicted in the figure, is ca. 18 Å. The CFC complex can be considered as three different regions: the central region of ca. 8 Å shows a high electron density, which reaches a maximum of approximately 1.25 times the electron density of water. The two external regions of ca. 5 Å display a steep decrease of the electron density with the distance from the central region of the CFC complex.

The region which is in contact with water should be partially hydrated, therefore the electron density should tend quickly to the unity. The one box model represents a good approximation to the electron density profile obtained theoretically, which is a further evidence of the formation of the inclusion complex. Exclusively the formation of the CFC complex is able to explain the existence of a 11 Å thickness region with an electron density 1.2 times higher than the electron density of water.

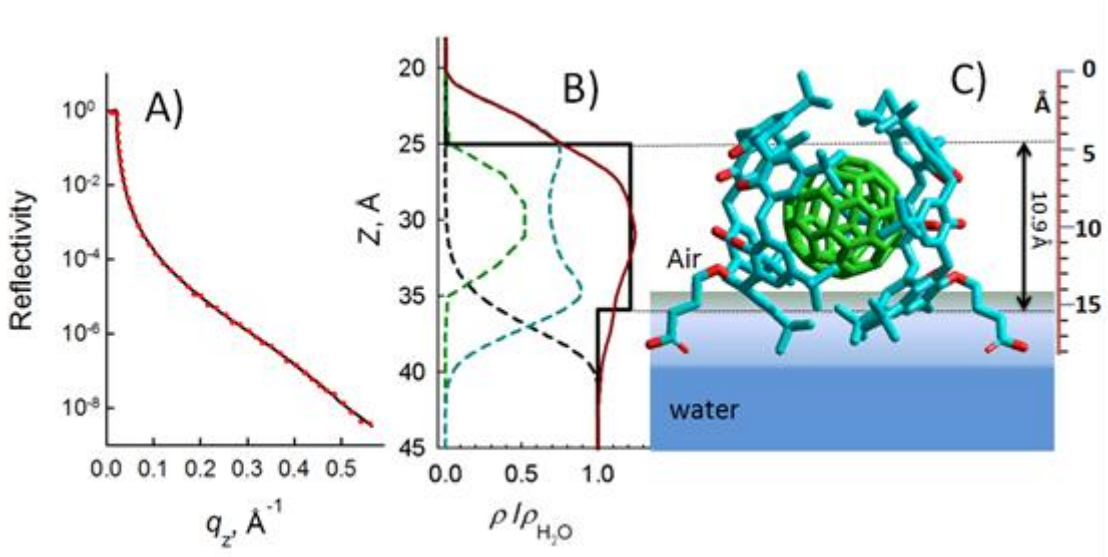

Figure 4. Left: X-ray reflectivity for CFC monolayer at 30 mN/m (red dot) and numerical fit using one box model (black solid line). Centre: Vertical profile of the relative electron density obtained from the numerical fit (black solid line) and from the spatial molecular distribution (red solid line). The profiles of the relative electron density for C60 (dashed green line) and C6A3C (dashed cyan line) are also shown. The dashed black line represents the electron density of water. Right: The vertical spatial distribution of CFC used for determine the relative electron density.

5.1.4. Conclusions

In this work, a novel mono substituted asymmetric derivative of *p-tert*-butylcalix[6]arene has been synthesized: C63AC. One of the six-OH groups is replaced by a -O-$(CH_2)_3$COOH group. The existence of only one acid group per molecule in the C6A3C derivative gives amphiphilic character to the the C63AC molecule. Moreover, the dissociation degree of the carboxylic group can be tuned to a certain extent.

The C6A3C molecule has been studied, both alone and in combination with fullerene (C_{60}) at the air/water interface. The complex C6A3C:C_{60} 2:1 (CFC) has been synthesized prior to the spreading on the air/water interface. The formation of this inclusion complex and the stoichiometry has been studied by UV-vis spectroscopy, confirming the C6A3C:C_{60} = 2:1. Charge transfer between the C_{60} and the calixarenes has been found.[22,38] The molecular conformation of both C63AC and CFC monolayers has been described convincingly by a combination of experimental and computational methods.

The C6A3C molecule adopts a parallel orientation of the main plane with respect to the air/water interface. In the case of the CFC complex, the C6A3C units adopt perpendicular orientation with respect to the air/water interface. The absence of

expansion in the surface pressure-molecular area isotherm confirms the formation of the inclusion complex between the C_{60} and the C63AC molecules. The perpendicular orientation of C6A3C units is stabilized by intermolecular H-bonds. Direct evidence of the presence of C_{60} in the CFC monolayer is obtained by in situ UV-vis reflection spectra. The UV-vis reflection spectra discard aggregation of the C_{60} molecules. The vertical electron density profile of CFC monolayer was determined using in situ synchrotron-based X-Ray reflectivity measurements, and a good agreement with the theoretical electron density profile for the inclusion complex was found.

We expect the inclusion complex calixarene:fullerene at the air/water interface to be useful as a model for the well-defined supramolecular structures containing both recognition and photofunctional molecules.

Acknowledments

The authors thank the Spanish CICYT for financial support of this research in the framework of Project CTQ2010-17481 and also thank the Junta de Andalucía (Consejería de Innovación, Ciencia y Empresa) for special financial support P08-FQM-4011 and P10-FQM-6703. A. González-Delgado, thanks the Ministerio de Ciencia e Innovación for a pre-doctoral grants (FPI program) and Juan J. Giner-Casares acknowledges Alexander von Humboldt Foundation for a postdoctoral fellowship. HASYLAB at DESY and Dr. Bernd Struth are acknowledged for excellent beamtime and support.

References

(1) Gutsche, C. D. *Calixarenes*; The Royal Society of Chemistry:: Cambridge, 1989.

(2) *Calixarenes 2001*.; Kluwer Academic: Dordrecht, 2001.

(3) Atwood, J. L.; Koutsantonis, G. A.; Raston, C. L. *Nature* **1994**, *368*, 229.

(4) Suzuki, T.; Nakashima, K.; Shinkai, S. *Chem. Lett.* **1994**, 699.

(5) Komatsu, N. *Org. Biomol. Chem* **2003**, *1*, 204.

(6) Andersson, T.; Nilsson, K.; Sundahl, M.; Westman, G.; Wennerström, O. *J. Chem. Soc. Chem. Commun.* **1992**, 604.

(7) Yoshida, Z.; Takekuma, H.; Takekuma, S.; Matsubara, Y. *Angew. Chem.* **1994**, *106*, 1658.

(8) Haino, T.; Yanase, M.; Fukazawa, Y. *Angew. Chem. Int. Ed. Engl.* **1997**, *36*, 259.

(9) Guldi, D. M.; Luo, C.; Prato, M.; Troisi, A.; Zerbetto, F.; Scheloske, M.; Dietel, E.; Bauer, W.; Hirsch, A. *J. Am. Chem. Soc.* **2001**, *123*, 9166.

(10) Wang, Y.-B.; Lin, Z. *J. Am. Chem. Soc.* **2003**, *125*, 6072.

(11) Lonetti, B.; Lo Nostro, P.; Ninham, B. W.; Baglioni, P. *Langmuir* **2005**, *21*, 2242.

(12) Dei, L.; Casnati, A.; Lo Nostro, P.; Baglioni, P. *Langmuir* **1995**, *11*, 1268.

(13) Dei, L.; LoNostro, P.; Capuzzi, G.; Baglioni, P. *Langmuir* **1998**, *14*, 4143.

(14) Dei, L.; Casnati, A.; LoNostro, P.; Pochini, A.; Ungaro, R.; Baglioni, P. *Langmuir* **1996**, *12*, 1589.

(15) Capuzzi, G.; Fratini, E.; Dei, L.; LoNostro, P.; Casnati, A.; Gilles, R.; Baglioni, P. *Colloids Surf. A* **2000**, *167*, 105.

(16) Capuzzi, G.; Fratini, E.; Pini, F.; Baglioni, P.; Casnati, A.; Teixeira, J. *Langmuir* **2000**, *16*, 188.

(17) Richardson, T.; Greenwood, M. G.; Davis, F.; Stirling, C. J. M. *Langmuir* **1995**, *11*, 4623.

(18) de Miguel, G.; Pedrosa, J. M.; Martín-Romero, M. T.; Muñoz, E.; Richardson, T. H.; Camacho, L. *J. Phys. Chem. B* **2005**, *109*, 3998.

(19) de Miguel, G.; Perez-Morales, M.; Martin-Romero, M. T.; Munoz, E.; Richardson, T. H.; Camacho, L. *Langmuir* **2007**, *23*, 3794.

(20) de Miguel, G.; Martin-Romero, M. T.; Pedrosa, J. M.; Munoz, E.; Perez-Morales, M.; Richardson, T. H.; Camacho, L. *Phys. Chem. Chem. Phys.* **2008**, *10*, 1569.

(21) Dei, L. L., P., ; Capuzzi, G.; Baglioni, P. *Langmuir* **1998**, *14*, 4143.

(22) Leach, S.; Vervloet, M.; Despres, A.; Breheret, E.; Hare, J. P.; Dennis, T. J.; Kroto, H. W.; Taylor, R.; Walton, D. R. M. *Chemical Physics* **1992**, *160*, 451.

(23) Ikeda, A.; Yoshimura, M.; Shinkai, S. *Tetrahedron Lett.* **1997**, *38*, 2107.

(24) Danauskas, S. M.; Li, D.; Meron, M.; Lin, B.; Lee, K. Y. C. *J. Appl. Cryst.* **2008**, *41*, 1187.

(25) Hyperchem.; 7.51 ed.; Hypercube, Inc.: 1115 NW 4th Street, Gainesville, Florida 32601, USA, 1999.

(26) Kane, P.; Fayne, D.; Diamond, D.; Bell, S. E. J.; McKervey, M. A. *J. Mol. Model* **1998**, *4*, 259.

(27) Van der Heyden, A.; Regnouf-de-Vains, J. B.; Warszynski, P.; Dalbavie, J. O.; Zywocinski, A.; Rogalska, E. *Langmuir* **2002**, *18*, 8854.

(28) Ishikawa, Y.; Kunitake, T.; Matsuda, T.; Otsuka, T.; Shinkai, S. *Journal of the Chemical Society-Chemical Communications* **1989**, 736.

(29) Hungerbüehler, H.; Guldi, D. M.; Asmus, D. *J. Am. Chem. Soc.* **1993**, *115*, 3386.

(30) Torres, V. M.; Posa, M.; Srdjenovic, B.; Simplício, A. L. *Colloids and Surfaces B: Biointerfaces* **2011**, *82*, 46.

(31) Grüniger, H.; Möbius, D.; Meyer, H. *J. Chem. Phys.* **1983**, *79*, 3701.

(32) Pedrosa, J. M.; Martín-Romero, M. T.; Camacho, L.; Möbius, D. *J. Phys. Chem. B* **2002**, *106*, 2583.

(33) Grüniger, H.; Möbius, D.; Lehmann, U.; Meyer, H. *J. Chem. Phys.* **1986**, *85*, 4966.

(34) Huesmann, H.; Bignozzi, C. A.; Indelli, M. T.; Pavanin, L.; A., R. M.; Mobius, D. *Thin Solid Films* **1996**, *62*, 284.

(35) Giner-Casares, J.; Pérez-Morales, M.; Bolink, H. J.; Lardiés, N.; Muñoz, E.; de Miguel, G.; Martín-Romero, M. T.; Camacho, L. *J. Mater. Chem.* **2008**, *18*, 1681.

(36) Ege, C.; Majewski, J.; Wu, G.; Kjaer, K.; Lee, K. Y. C. *ChemPhysChem* **2005**, *6*, 226.

(37) Evers, F.; Shokuie, K.; Paulus, M.; Sternemann, C.; Czeslik, C.; Tolan, M. *Langmuir* **2008**, *24*, 10216.

(38) Ikeda;, A.; Yoshimura;, M.; Shinkai, S. *Tetrahedron Letters* **1997**, *38*, 2107.

CONCLUSIONES

Al final de cada capítulo de esta Memoria se incluyen las conclusiones particulares del estudio desarrollado en cada uno de dichos capítulos. En este apartado se presentan conclusiones más generales, teniendo en cuenta las implicaciones prácticas del trabajo desarrollado en cada capítulo.

1. Se ha probado que la técnica de Langmuir es de gran utilidad para preparar películas de compuestos orgánicos con un alto grado de ordenación a nivel molecular. Así mismo, ha demostrado ser una de las pocas técnicas que permite un cierto grado de control sobre dicha ordenación, así como de la agregación, la orientación y, en algunos casos, la conformación de las moléculas, siempre que se trabaje con sistemas que tengan las características adecuadas para ello.
2. Se ha demostrado que la combinación de técnicas ópticas y espectroscópicas, junto con simulaciones computacionales relativamente sencillas, es una poderosa herramienta para el estudio y caracterización de películas orgánicas en la interfase aire-agua.
3. El estudio del colapso de una película formada por DOMA y TSPP ha permitido establecer limitaciones al uso de la teoría NGC clásica en la formación de estructuras tridimensionales en la interfase. También ha arrojado luz sobre los factores que influyen en la reversibilidad del colapso de este tipo de películas, como son la línea de tensión de los dominios tridimensionales formados o la presencia de regiones donde persista la monocapa bidimensional al final del colapso de la película.
4. Se ha descubierto que la relación entre las áreas que ocupan las cadenas hidrófobas y los grupos polares cromóforos es un factor crucial en la formación de películas estables de mezclas de colorantes anfifílicos y lípidos, y en el control de la agregación de dichos colorantes en la interfase. Así mismo, se ha demostrado que este tipo de sistemas pueden formar estructuras ópticamente heterogéneas que se organizan en forma de cristal líquido bidimensional.
5. Se ha sintetizado un nuevo calixareno anfifílico monosustituido que, a diferencia de otros calixarenos, forma monocapas homogéneas y estables en la interfase aire-agua. También se ha sintetizado el complejo de inclusión de este calixareno y fullereno en proporción 2:1, CFC, que también es capaz de formar monocapas estables. Las monocapas formadas por ambos compuestos presentan morfologías diferentes, debido a la distinta orientación respecto a la interfase de las moléculas de calixareno en uno y otro sistema. Dado que el fullereno es un buen aceptor de electrones, el CFC tiene potencial para formar complejos supramoleculares más grandes con moléculas donadoras de electrones, como por ejemplo las porfirinas, en los que se pueda controlar la distancia entre las mismas, así como su orientación y agregación.

At the end of each chapter of this report, specific conclusions relevant to the work described in it have been included. In this section, a summary of more general conclusions**,** which take into account the practical implications of the work developed in each chapter, is presented.

1. It has been proven that the Langmuir technique is very useful to prepare organic films with a high grade of molecular order. Likewise, it has shown to be one of the few techniques that allow a certain grade of control over that order, as well as over the aggregation, orientation and, in some cases, the molecular conformation, provided that the studied molecular system has the proper characteristics for it.
2. It has been demonstrated that the combination of optic and spectroscopic techniques, plus relatively simple computational simulations, are powerful tools for the study and characterization of organic films at the air-water interface.
3. The study of the collapse of a film formed by DOMA and TSPP allowed establishing some limitations to the use of the classical NGC theory for the formation of tridimensional structures at the air-water interface. It also shed light on the factors which influence the reversibility of the collapse process of this kind of films, like the line tension of the tridimensional domains formed or the presence of regions where the bidimensional monolayer persists at the end of the collapse of the film.
4. It has been discovered that the relation between the area occupied by the hydrophobic chains and the chromophores polar groups, is a key factor in the formation of stable films with mixtures of amphiphilic dyes and lipids, as well as in the control of the aggregation of such dyes at the interface. Likewise, it has been proven that this kind of systems can form optically heterogeneous structures, organized as a bidimensional liquid cr**y**stal.
5. A new monosubstituted amphiphilic calixarene, which, unlike other ordinary and amphiphilic calixarenes, forms homogeneous and stable films at the air-water interface, has been synthesized. An inclusion complex with this calixarene and a fullerene in a 2:1 ratio, named CFC, has also been synthesized. This inclusion complex forms stable monolayers at the air-water interface, too. The films formed by both compounds present different morphologies due to the different orientation with respect to the interface of the calixarene molecules in the two systems. As the fullerene is a good electron acceptor, the CFC has potential to be used to form bigger supramolecular complexes with electron donors like, for example, porphyrins, in which their separation, orientation and aggregation can be controlled.

ANEXO

PUBLICACIONES Y CONGRESOS

La Tesis Doctoral presentada por D. Antonio Miguel González Delgado, que lleva por título *"Películas orgánicas organizadas en sistemas nanoestructurados"* consta de los siguientes apartados:

Objetivos, Introducción, Resultados y Discusión, Conclusiones y Anexo.

Se pretende su defensa como compendio de publicaciones en base a que se cumplen los requisitos establecidos para ello, como se documenta a continuación:

Publicaciones de la Tesis Doctoral:

1. "Reversible Collapse of Insoluble Monolayers: New Insights on the Influence of the Anisotropic Line Tension of the Domain"

   Gonzalez-Delgado, AM; Perez-Morales, M; Giner-Casares, JJ; Munoz, E; Martin-Romero, MT; Camacho, L.

   Journal of Physical Chemistry B ***113*** (2009) 13249-13256

   Categoría: Physical, Chemistry. Factor de impacto (2010): 3.603. Posición en el ranking: 32 de 127

2. " Control of the Lateral Organization in Langmuir Mono layers via Molecular Aggregation of Dyes"

   Gonzalez-Delgado, AM; Rubia-Paya, C; Roldan-Carmona, C; Giner-Casares, JJ; Perez-Morales, M; Munoz, E; Martin-Romero, MT; Camacho, L; Brezesinski, G

   J. Phys. Chem. C **114** (2010) 16685-16695

   Categoría: Physical, Chemistry. Factor de impacto (2010): 4.524. Posición en el ranking: 27 de 127

3. "The Effect of the Reduction of the Available Surface Area on the Hemicyanine Aggregation in Laterally Organized Langmuir Monolayers"

   Gonzalez-Delgado, AM; Giner-Casares, JJ; Rubia-Paya, C; Perez-Morales, M; Martin-Romero, MT; Brezesinski, G; Camacho, L

   J. Phys. Chem. C **115** (2011) 9059-9067

   Categoría: Physical, Chemistry. Factor de impacto (2010): 4.524. Posición en el ranking: 27 de 127

4. Langmuir monolayers of an inclusion complex formed by a new calixareno derivative and fullerene

   Gonzalez-Delgado, AM; Giner-Casares, JJ; Brezesinski, G; Regnouf-de-Vains, JB; Camacho, L

   Pendiente de aceptación

Comunicaciones y Ponencias en Congresos:

1. Autores: Gonzalez-Delgado, AM; Rubia-Paya, C; Giner-Casares, JJ; Perez-Morales, M; Munoz, E; Martin-Romero, MT; Camacho, L; Brezesinski, G

   Título: Control of the lateral organization and effect of the reduction of the available surface area on Langmuir monolayers formed by hemicyanine

   Tipo de participación: Comunicación oral

   Congreso: ECOF12. 12TH European Conference on Organized Films

   Lugar de celebración: Sheffield (England) Fecha: 2011

2. Autores: Gonzalez-Delgado, AM; Rubia-Paya, C; Jiménez Millán, E; Giner-Casares, JJ; Munoz, E; Camacho, L

   Título: Organización lateral de monocapas mixtas

   Tipo de participación: Póster

Congreso: NanoUco III. Encuentro sobre nanociencia y nanotecnología de investigadores y tecnólogos andaluces

Lugar de celebración: Córdoba (España) Fecha: 2011

3. Autores: Gonzalez-Delgado, AM; Perez-Morales, M; Giner-Casares, JJ; Munoz, E; Martin-Romero, MT; Camacho, L

   Título: Colapso reversible de monocapas insolubles. Influencia de la línea de tensión de los dominios.

   Tipo de participación: Comunicación oral

   Congreso: NanoUco II. Encuentro sobre nanociencia y nanotecnología de investigadores y tecnólogos de la UCO

   Lugar de celebración: Córdoba (España) Fecha: 2010

4. Autores: Gonzalez-Delgado, AM; Perez-Morales, M; Giner-Casares, JJ; Munoz, E; Martin-Romero, MT; Camacho, L

   Título: Reversible collapse of insoluble monolayers.

   Tipo de participación: Póster

   Congreso: III Reunión Ibérica de Coloides e Interfases (RICI). VIII Reunión del Grupo Especializado de Coloides e Interfases (GECI) de las Reales Sociedades Españolas de Física y Química.

   Lugar de celebración: Granada (España) Fecha: 2009